DOCTOR OF PHILOSOPHY

Improved incompressible SPH method for predicting wave impacts on coastal structures

Gui, Qinqin

Award date:
2014

DOCTOR OF PHILOSOPHY

Improved incompressible SPH method for predicting wave impacts on coastal structures

Qinqin Gui

2014

University of Dundee

Improved incompressible SPH method for predicting wave impacts on coastal structures

Qinqin Gui

July 2014

A thesis submitted to the University of Dundee for the degree of Doctor of Philosophy in the School of Engineering, Physics & Mathematics

Declaration

I declare that this work is original, except where indicted by special reference in the text. No part of the work referred to in the thesis has been submitted in support of an application for any another academic degree.

SIGNED: …… DATE: ……14/09/2014……..

Certificate

This is to certify that Qinqin Gui has done this research under my supervision, and that she has fulfilled the condition of Ordinance 14 of the University of Dundee, so that she is qualified to submit the following thesis in application for the degree of Doctor of Philosophy.

SIGNED: …… DATE: ……15/09/2014……..

Acknowledgements

Completing this thesis has been a life-changing journey for me. My acknowledgments to those who have helped me in reaching the destination are heartfelt.

First and foremost, I would like to express my deepest gratitude to my supervisor Prof. Ping Dong for his guidance with unique patience and remarkable insight, and constant support academically and financially to enable me to complete this work. His enthusiasm and broad view on research has had a great impact on me. I would also like to thank Dr. Songdong Shao for his expert advice, and for being a constant source of help throughout the research. He often spent hours to discuss with me about my research, as well as gave me generous advice on my future career. He is not only a good teacher but also a wise friend.

I want to thank Yiqiang Chen for providing many great ideas when I was at my wits end or depressed, and to Dr. Chunyan Zhou, Chunyang Xu, Dr. Haixia Xu, Dr. Jisheng Zhang, and all other people in the Fluid Group for their helpful suggestions and encouragements. Many thanks also to all the students I have come to know in University of Dundee, whose friendship and companionship I will always treasure. In addition, I want to thank all the staffs in the Division of Civil Engineering for providing such a stimulating research environment.

I am indebted Dr. Kezhao Fang and Prof. Zhili Zou for recommending me to obtain the scholarship from Chinese Scholarship Council and University of Dundee, as well as being the good advisors for my MSc aster study at University of Dalian technology. I am also indebted to the Chinese Scholarship Council and University of Dundee for funding this work. I extend a special thanks to my dearest friends Yu Zhang and Juan Yuan for helping me come to UK by being my guarantors for studying aboard.

Last but not the least, I would like to express my sincere gratitude to my family who have supported and encouraged me over the years. I especially want to

thank my sister and brother for their inspiration and continuous encouragement during my studies. Finally, I want to extend my profound appreciation to my beloved parents for their love, affection, and invaluable support during my life and studies.

And last, thanks to myself.

Papers and conferences

[1] **Gui, Q**., Dong, P. and Shao, S., (2014). "Numerical Study of PPE Source Term Errors in the incompressible SPH Models." *International Journal for Numerical Methods in Fluids*. (under review) (**Chapter 5**)

[2] **Gui, Q**., Shao, S., and Dong, P. (2014). "Wave Impact Simulations by an Improved ISPH Model." *Journal of Waterway, Port, Coastal, and Ocean Engineering*, 10.1061/(ASCE)WW.1943 -5460.0000239, 04014005. (**Chapter 4**)

[3] **Gui, Q**., Dong, P. and Shao, S., (2013). "Wave impact prediction by an Improved Smoothed Particle Hydrodynamics (SPH) method." *26th Scottish Fluid Mechanics Conference*.

Abstract

Smoothed Particle Hydrodynamics (SPH) is a simple and attractive meshless Lagrangian particle method for simulating free surface flows and has been widely applied in predicting wave impacts on coastal structures. However, despite the superior theoretical basis the performance of the existing Incompressible SPH models based on either a density invariant or a velocity divergence-free formulation is often not better than the recently improved Weakly Compressible SPH models. This could be largely caused by the particular formulations of the Pressure Poisson Equation (PPE) source term in the existing ISPH models and a better formulation of this source term can be expected to significantly improve the accuracy of the ISPH models

This thesis presents an improved incompressible smoothed particle hydrodynamics (ISPH) method for wave impact applications by combining the density invariant and velocity divergence free formulations in a weighted average manner to form a general source term. The model is then applied to two problems: (1) dam-breaking wave impact on a vertical wall and (2) solitary wave run-up and impact on a coastal structure. The computational results have indicated that the new source term treatment can predict the wave impact pressure and force more accurately compared with using either density invariant or a velocity divergence-free formulation alone. It was further found that depending on the application case, the influence of the density invariant and velocity divergence-free parts could be quite different. A simple parameterisation that relates the weighting coefficient α in the mixed pressure source term to the ratio of the characteristic height to length scales of the flow system is proposed and evaluated.

In order to gain further insight into the effects of the source term formulations on the impact pressure prediction, three more benchmark fluid impact problems including two dam break flows and one solitary wave impact are investigated using the three different ISPH numerical schemes, respectively. The

computational results are validated against either the experimental data or numerical data based on the WCSPH. The in-depth numerical analysis has revealed that the pure density-invariant formulation can lead to relatively large divergence errors while the velocity divergence-free formulation may cause relatively large density errors. As compared with these two approaches the mixed source term formulation performs much better having the minimum total errors in all test cases.

Finally, the SPH model was applied to study the wave interaction with porous structure to investigate the flow motion in and around the porous structure. In order to describe correctly the flow through the interface between the porous region and pure fluid region within the SPH framework a heuristic and boundary treatment method was proposed. The SPH model was validated against the theoretical data of wave propagating over a porous bed and further investigated by comparing the predicted wave surface profile and velocity results with the experiment data for a typical case of flow motion inside of a submerged the porous structure. A good agreement is obtained between the numerical results and experiment data. All these demonstrate that the improved ISPH model developed in this work is capable of modelling the wave interaction with porous structure.

Contents

Notation

$A(\mathbf{r})$	Any field function
$\mathbf{r}$	Particle position
δ	Dirac delta function
W	SPH interpolation kernel
m	Particle mass
m_a	Mass of neighbouring particle a
ρ_a	Density of neighbouring particle a
m_b	Mass of neighbouring particle b
ρ_b	Density of neighbouring particle b
V_b	Density of neighbouring particle b
$\mathbf{r}_a$	Position of particle a
$\mathbf{r}_a$	Position of particle b
h	Smoothing length of kernel or elevation of house location
κ	Scaling factor
$\nabla A(\mathbf{r})$	Gradient field function $A(\mathbf{r})$
q	r/h Relative distance between the particles
r	Separation distance between the particles
ν	Number of dimension
$\nabla \cdot \mathbf{u}$	Divergence of a vector $\mathbf{u}$
P	Pressure
∇P	Gradient of pressure
$\overset{\Rightarrow}{\boldsymbol{\tau}}$	Shear stress tensor
$\overset{\Rightarrow}{\Delta}$	Strain tensor
μ_{eff}	Effective viscosity

ν_a	Molecular kinematic viscosity of particle a
ν_b	Molecular kinematic viscosity of particle b
η	Small number in order to avoid the denominator being zero
$\mathbf{u}$	Particle velocity
t	Time
$\mathbf{u}_*$	Intermediate particle velocity
$\mathbf{u}_t$	Particle velocity at time t
$\Delta\mathbf{u}_*$	Changed particle velocity during prediction step
$\Delta\mathbf{u}_{**}$	Corrected particle velocity increment
Δt	Time increment/step
$\mathbf{r}_*$	Intermediate particle position
$\mathbf{r}_t$	Particle position at time t
ρ	Fluid particle density
ρ_*	Intermediate particle density after the prediction step
ρ_0	Initial and constant particle density
P_{t+1}	Particle pressure at time $t+1$
$\mathbf{u}_{t+1}$	Particle velocity and position at time $t+1$
$\mathbf{r}_{t+1}$	Particle velocity and position at time $t+1$
l_0	Initial particle spacing
V_{max}	Maximum particle velocity at each time step
Δt_n	Current time step
Δt_{n+1}	Next time step
$\mathbf{n}$	Unit vector of normal direct
d	Still water depth
η	Water surface elevation
A	Wave amplitude or wave height
c	Speed of wave

$X_P(t)$ Wave paddle displacement

$u_P(t)$ Wave paddle velocity

U_d Damped velocity

U_0 Particle velocity at the start line $x = x_0$

$f(x)$ Damping function of wave

L_d Length of the damping zone

v_T Turbulence eddy viscosity

ΔX Mixing length

$\overline{S}_{ij}$ Components of the strain-rate tensor

k Turbulence kinetic energy

δ_{ij} Kronecker's delta

C_s Smagorinsky constant

$|\overline{S}|$ Local strain rate

α Weighting coefficient in mixed PPE source term

β Weighting coefficient in mixed PPE source term

ρ_i Density of particle *i*

$\rho_i(t)$ Density time series of particle *i*

D_0 Particle size

F Wave force

F_0 Reference wave force

g Gravitational acceleration

H Wave height

H Water column height in dam break case

L Horizontal length scale in a flow system

R Vertical wave run-up height

t_0 Time origin of wave travel

τ $(d/g)^{1/2}$ time scale

$E_d(t)$ Normalized particle density error

t_0 Time origin

h Elevation of the house location on slope dike

θ Weighting coefficient

E_{den} Normalized density errors

E_{div} Normalized velocity divergence errors

$\nabla \cdot \mathbf{u}_i$ Velocity divergence of particle *i*

$\nabla \cdot \mathbf{u}_i(t)$ Velocity divergence time series of particle *i*

$\mathbf{u}_w$ Flow velocity outside of porous structure

$\mathbf{u}_p$ Discharge velocity

v Molecular viscosity

n_w Porosity of the porous media

K_P Intrinsic permeability

C_f Nonlinear resistance coefficient

d_{50} Characteristic diameter (or stone size) of porous materials

H_i Initial wave height

S_0 Stoke of wave paddle

h_p Depth of the porous bed

h_0 Constant water depth in porous cases

List of Figures

List of tables

Chapter 1

Introduction

1.1 Motivation

Wave impact poses a major threat to the safety of coastal structures during their lifetime. Violent pressures from the wave impact can cause severe damage or collapse of coastal structures such as the breakwaters, offshore oil platforms and ships, especially when the hurricane and tsunami happen. The study of fluid impact on structures is therefore of significant importance in order to understand the underlying physics of the hydrodynamic phenomena, evaluate the structure stability and to develop effective measures to prevent the possible structure damages and functional failure.

Laboratory experiments or field measurements are traditionally used to study such wave impact problem. But it is often difficult and expensive to measure the impact pressure in natural environment. Although considerable efforts have been made to simulate accurately wave interactions with various forms of coastal structures in laboratory flumes and basins, the inevitable scale effects present in these physical models mean that the hydrodynamic conditions generated in the laboratories cannot fully reproduce the real prototype wave impact phenomena.

As an alternative, numerical studies of wave impact on coastal structures are widely carried out by the researchers and engineers either to understand the physical processes involved or to provide the practical design parameters (Cummins et al., 2012; Lara et al., 2008). To predict wave interactions with coastal structures and the wave impact forces, a variety of numerical models have been developed: Demirbilek and Nwogu (2007) comprehensively evaluated the practical applications of the Boussinesq models (such as BOUSS-2D and MIKE21) in wave propagation and

runup over the fringing coral reefs. Liu et al. (1999) used a Reynolds-averaged Navier-Stokes (RANS) model to investigate the breaking wave impact on a caisson breakwater protected by the porous layer. Huang and Dong (2001) solved the primitive Navier-Stokes (N-S) equations and studied the solitary wave passing over a submerged impermeable obstacle. Shiach et al. (2004) solved the shallow water equations (SWEs) based on the finite volume (FV) numerical scheme to study violent wave overtopping under different impact conditions.

There exist two broad approaches in describing fluid flows in Fluid Mechanics: Eulerian and Lagrangian approaches. All above mentioned modelling works are based on the Eulerian approach, which has been developed more than fifty years concerning with different aspects of flow simulations. In recent years, advances in modern computers have enabled the rapid development of latter in the form of mesh-free Lagrangian particle models. These particle methods have many advantages in simulating complex fluid flows. For example, when solving the N-S equations in a mesh-free particle method, the advection term is calculated directly for each individual particle and thus the numerical diffusions can be greatly reduced. In comparison, numerical diffusion is an inevitable problem in any Eulerian grid-based approach and can result in serious errors, especially when the deformation of the free surface is very large. In a mesh-free particle method, determining the free surface is more straightforward because the calculation points are just the moving particles in the Lagrangian coordinates and the free surface can be captured directly by tracing these particles, thus avoiding the need for mesh readjustment which is usually unavoidable in any mesh-based Eulerian approaches.

For civil engineering and coastal hydrodynamic computations, two particle modelling techniques are frequently used i.e. Moving Particle Semi-implicit (MPS) method (Khayyer and Gotoh, 2009a) and Smoothed Particle Hydrodynamics (SPH) (Gómez-Gesteira et al., 2005) method with the latter being more popular and more extensively developed. The Smoothed Particle Hydrodynamics (SPH) method was originated in the astronomic applications (Gingold and Monaghan, 1977; Lucy, 1977). It was then further developed in astrophysics for the study of dynamics of interstellar gas (Monaghan, 1992) and subsequently applied in many other fields

such as ballistics, volcanology, and oceanography. Since the first demonstration of its potential in simulating fluid flows (Monaghan, 1992) the SPH method has proven to be a powerful tool in modelling a wide range of wave impact problems in coastal engineering.

The basic concept of the SPH is that any field variable of a reference particle can be expressed with enough accuracy by appropriate integrals, which are approximated by summation interpolants over neighbouring particles. As a particle method, a grid is not needed to calculate the spatial derivatives in SPH. All spatial derivatives including the gradient, divergence and Laplacian operators in the Navier-Stokes equations can be similarly evaluated by the summation interpolants with particle properties.

In the earlier fluid impact simulations by the SPH, the fluid media was treated as being slightly compressible so the method was referred to as the Weakly Compressible SPH (WCSPH) (Monaghan and Kos, 1999; Monaghan et al., 2003). By using this approach, different wave impact problems have been studied including Gomez-Gesteira et al. (2005) for a green water wave interaction with a horizontal deck, Crespo et al. (2007) for a 3D large wave interaction with a dike, Rogers et al. (2010) for a caisson breakwater movement and Liang et al. (2010) for a solitary wave impact on the coastal house, etc. However, because in this method the computation of fluid pressures was based on an equation of state related to the thermodynamic formulation, relatively large pressure fluctuations and noises are often generated, which could greatly compromise the simulation accuracy.

Following the novel SPH projection approach (Cummins and Rudman, 1999), different incompressible SPH methods (ISPHs) were developed in recent years. The key feature of this approach is that the fluid pressure was solved using a truly hydrodynamic formulation based on the pressure Poisson equation (PPE) in a way similar to most mesh-based hydrodynamic schemes. Quite a few works have demonstrated that in simulating fluid impact the ISPH could predict a more stable pressure and particle field than that of the WCSPH and no additional numerical smoothing techniques such as the XSPH correction (Monaghan, 1989) or kernel corrections were needed. By using this ISPH approach, Shao (2005) studied the

solitary wave impact on a partially immersed curtain wall, Khayyer and Gotoh (2009b) investigated the wave impact pressure due to the sloshing waves and Khayyer et al. (2009) addressed comprehensively both the dam-break flow and violent wave impacts on the structures.

Recently, a number of works have been reported on the pros and cons of WCSPH and ISPH for the free surface flow simulations. Hughes and Graham (2010) studied two standard dam-break problems and one regular water wave impact against a vertical wall and they found that the WCSPH performs at least as well as ISPH, and in some respects even performs better. Shadloo et al. (2012) studied the bluff body flow problems such as flow over an airfoil and a square obstacle and their predictions of a variety of flow parameters indicated that the WCSPH method with the suggested improvements produced numerical results as accurate and reliable as those of the ISPH. Chen et al. (2013) investigated three benchmark hydrodynamic problems including a liquid sloshing and concluded that their improved WCSPH is more attractive than the ISPH in modelling free surface incompressible flows as it is more accurate and stable with comparable or even less computational efforts. It should be noted that these WCSPHs have all included some additional numerical treatments to improve the model performances, such as the Moving Least Squares (MLS) density filter or XSPH schemes, while there were no corresponding treatments in the ISPHs used so the comparisons of the two techniques reported may not have been entirely fair.

For the ISPH modelling techniques, there exist two general branches, i.e. density-invariant ISPH and velocity divergence-free ISPH. The former uses the density difference as source term in the PPE while the latter uses the divergence of flow velocity field. The density-invariant ISPH was initially proposed by Shao and Lo (2003) and the velocity divergence-free ISPH was initially proposed by Hu and Adam (2007) and Lee et al. (2008), both of which were rooted in the projection concept of Cummins and Rudman (1999) but applied in the free surface flows.

As severe particle oscillation may be caused by the pressure noises arising from the solution of PPE, a number of SPH techniques have been developed to reduce the pressure noises and particle oscillations, such as the kernel corrections

and density filters similar to WCSPHs. As to ISPH methods the focus has been placed on improving the PPE source term representation, noting in particular that the density-invariant and velocity divergence-free approaches do not provide identical impact pressure and force predictions, although both schemes were consistent in satisfying the incompressible principles. For example, Xu et al. (2009) found that the divergence-free ISPH method cannot maintain the stability in certain situations although it is fairly accurate before the instability sets in, while the density-invariant ISPH method is stable but often associated with the random-noise like disturbances. On the other hand, Cummins and Rudman (1999) and Hu and Adam (2007) found that if only a discrete velocity divergence-free condition is enforced, larger density-variation or particle clustering may occur due to the spatial truncation errors of the discretization scheme and the density errors can accumulate during long time computations. Clearly, despite the attractiveness of ISPH, more work is still need to improve its accuracy and enhance its robustness, especially in the prediction of large wave impact on the diverse range of complex structures found in coastal engineering practices.

1.2 Thesis scope

The scope of this thesis is threefold. Firstly, it proposed a novel formulation of pressure Poisson equation in incompressible SPH algorithm, mixed pressure Poisson equation, which is essentially a combination of the two existing pressure Poisson equations (density invariant PPE and velocity divergence free PPE), and applied this SPH model to study the wave impact on coastal structure. The capability of the new SPH model will be tested systematically in wave impact predictions involving different flows such as dam break and wave run-up on a sloping dike together with an evaluation of model convergence with changing the size of particle spacing. A general formula for determining the weighting parameter was developed based on these cases studies. Secondly, an in-depth evaluation was carried out to determine the size and nature of the errors associated with different two types of source terms

in the PPE based on a detailed numerical analysis of the three types of PPE (mixed PPE, density gradient PPE, velocity divergence PPE). The influence of each PPE on density gradient and velocity divergence is revealed. Thirdly, the ISPH model was applied to study flow through porous structures. A simple and rational interface boundary treatment consistent with the SPH approach was developed for effective simulation of flows outside and inside of porous structures.

The importance of this work is threefold: firstly, a new ISPH model with higher accuracy was proposed and validated for free-surface flow and wave interaction with coastal structure; and secondly, it reveals the origin and nature of errors associated with different ISHP formulations, which not only help the understanding of the performance of ISPH methods but point to directions for its future improvement; and finally by extending the new ISPH model to flow through porous structures and with the suggested improved treatment of interface boundaries the work provides a potentially valuable engineering tool for analysis of flow through porous coastal structures and direct evaluation of the stability of rock armours in the rubble-mound breakwaters.

1.3 Outline of thesis

The thesis is divided in seven chapters and structured as follows:

The first chapter describes the research motivation and scope of the thesis, as well as the structure of the thesis.

The second chapter gives the basic concepts related to SPH methodology and the properties of kernel function and reviews various SPH formulas that were used in the ISPH model and their applications.

The third chapter presents the general numerical framework of the ISPH model and its solution procedures, followed by the formulation of a new PPE source term, which is in the form of the weighted average of the commonly used density invariant and velocity divergence free source terms. The treatment of solid boundary

and free surface conditions is explained as well as the description of the type of waves used in the research and the wave generation method in the model.

The fourth chapter is concerned with the validation of the new ISPH model with the new form of PPE source term by applying the new model to two different wave impact cases, i.e. dam-break flow impact on a wall and solitary wave impact on a beach house. Compared with the existing ISPH models and other similar particle modelling techniques, the key feature of the present model is that it includes both the density invariant and velocity divergence free terms in a simple combination and is computationally efficient involving no additional subroutines, which makes it more suitable for the practical engineering application. The model improvement is directed at achieving better representation of wave impact pressures and forces rather than the wave surface profiles and flow velocities, as the former are more susceptible to the particle disorder and pressure noise. Also included in this chapter is a sensitivity analysis to investigate the influence of particle spacing on the weighting coefficient of the density invariant and velocity divergence free terms in the PPE and check the convergence of numerical scheme. A semi-empirical approach is proposed to predict the weighting coefficient in PPE source term based on the energy damping principles.

In Chapter 5, extending the work in Chapter 4, three more benchmark fluid impact problems including two dam break flows and one solitary wave impact are investigated using the three different ISPH numerical schemes, respectively. The computational results are validated against either the experimental data or numerical data based on the WCSPH. And above all, an extensive numerical analysis is carried out to quantify the density and divergence errors of three different ISPH numerical schemes for the dam break flows and solitary wave impact. In order to further reveal the possible reason for the density error and velocity divergence error, the systematic analysis not only includes the numerical error in temporal domain but also the numerical error in spatial domain for three source term treatments. The temporal and spatial distributions of the particle density and velocity divergence errors were investigated.

Chapter 6 begins with a description of the governing equations of both flows outside and outside the porous media. After that, a boundary treatment was proposed to deal with the interface between pure fluid region and porous media region. The accuracy of the numerical model for porous structures study was verified by comparing the numerical results of wave damping over porous bed with the theoretical solution of Packwood and Peregrine (1980). Finally, the SPH model was applied to investigate the features of flow field around and inside a submerged porous breakwater under the action of waves, such as velocity and pressure. Comparison of the wave surface profiles and velocity results with the experiment of Wu and Hsiao (2013) was carried out to test the capacity of SPH model.

Finally, Chapter 7 summarises the findings of this research and provides suggestions for future work.

Chapter 2

SPH methodology

Smoothed particle hydrodynamics is a numerical computational method used for simulating fluid flows and is a Lagrangian method. Flow of continuous media is represented in the form of discrete particles, and the positions of the discrete computational points change with the flow movement. The flow movement is implemented by the interaction of particles within the influence domain in SPH simulation, which was reflected in the integral interpolations approximation equation of physical quantities through the smoothing kernel function mathematically.

2.1 Basics of SPH

Generally, the simulation domain is consisted of large number of infinitesimal bodyies, which are called computation points in practical implementation. In this section, the computation point will be defined and described in detail. On the other hand, integral interpolants are fundamental to the SPH method originally invented for astrophysics. So the integral interpolant functions will be introduced for understanding the basic conception and the expressions of variable and derivatives, as well as for using the SPH formulations more flexibly.

2.1.1 Particle definition

In a given fluid zone, the zone is divided into many small volumes of spaces as shown in Figure 2.1. Each of the space contains a fixed mass of fluid and is so-called particle in SPH. The boundary of the fluid zone is also discretised into one line or

several lines of particles. So an ensemble of particles forms a dependent particle system in SPH.

The particles are just the computational points in SPH, analogous to the nodal points in the finite element method. All the particles possess the physical quantities such as position, mass, velocity, pressure, density in SPH. It is obvious that the mass of each particle depends on the material properties of the particles and the volume of space represented by the particle. The movement properties of these particles can be obtained according to the governing dynamics, such as Navier-Stokes equations or equations of motion.

At the beginning, all the quantities need to be initialized by being given a specific value. The mass is the only constant among these physical quantities through the simulations. As a Lagrangian method, the particles move with its velocity in SPH. It means the position of particle varies from one time step to the next time step. This is different from Eulerian methods, in which the computational point is a fixed position in space. It is also necessary to be noted that the density of each particle in SPH is different of the nature density of water, it's the averaged density evaluated by summing up the contributions of the neighboring particles. However, water is normally regard as incompressible, so density is required to be a constant in truly incompressible SPH model. Density is considered only slightly changeable even for weakly compressible SPH approach.

2.1.2 Interpolation function

The key feature of the SPH is that it is an interpolation method, which allows the physical quantity and any function of interest to be obtained by summation of relevant physical quantities and functions (Monaghan, 1992). The summation usually can be expressed in terms of the values at a set of disordered points within the range of the support domain as indicated in Figure 2.1.

The deduction procedure starts from the fact that the value of any field function $A(\mathbf{r})$ at point $\mathbf{r}$ can be expressed as

$$A(\mathbf{r}) = \int A(\mathbf{r}')\delta(\mathbf{r}-\mathbf{r}')d\mathbf{r}' \tag{2.1}$$

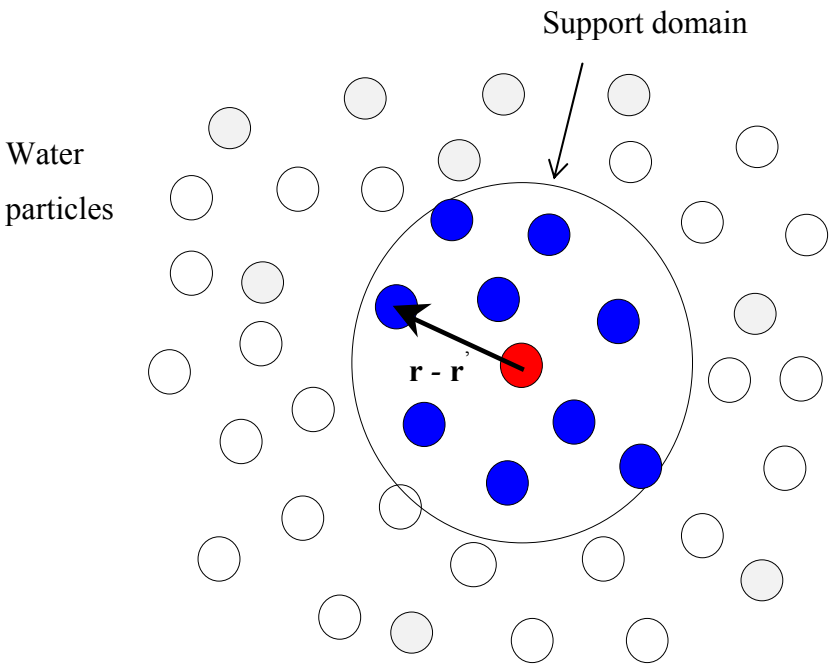

Figure 2.1. Schematic of discrete fluid particles

where $\delta(\mathbf{r}-\mathbf{r}')$ is the Dirac delta function, which is a special function for always equalling to zero except at the point $\mathbf{r}' = \mathbf{r}$.

$$\delta(\mathbf{r}-\mathbf{r}') = \begin{cases} +\infty & \text{if } \mathbf{r}' = \mathbf{r} \\ 0 & \text{if } \mathbf{r}' \neq \mathbf{r} \end{cases} \tag{2.2}$$

Obviously, $\int_{-\infty}^{+\infty} \delta(\mathbf{r}-\mathbf{r}')d\mathbf{r}' = 1$. So the computation of a quantity of any particle only depends on itself and has no interaction with other particles since the Dirac delta function is infinitesimally narrow.

The Dirac delta function was replaced by an appropriate smoothing function, which was generated to obey the physical principle of interaction influence between

particles. When particles are close to each other, a bigger weighting is considered for contribution in the SPH computation. So the integral interpolant of any field function $A(\mathbf{r})$ is approximated by the following expression:

$$A(\mathbf{r}) = \int A(\mathbf{r}')W(\mathbf{r}-\mathbf{r}', h)d\mathbf{r}' \tag{2.3}$$

where $W(\mathbf{r}-\mathbf{r}', h)$ is the interpolating kernel function, h is the smoothing length and will be discussed in section 2.2 later.

Finally, the quantity $A(\mathbf{r})$ in equation (2.3) at particle a is averaged or smoothed with the corresponding values of the particles around it. In practice, the integral interpolant in SPH numerical simulations is calculated by a summation interpolant in the discrete notation as

$$A_a(\mathbf{r}) = \sum_b m_b \frac{A_b(\mathbf{r})}{\rho_b} W_{ab} \tag{2.4}$$

where a and b denote the reference and neighbouring particles, respectively; m_b and ρ_b are the mass and density of neighbouring particle b, respectively; $d\mathbf{r}'$ in equation (2.3) becomes the volume of neighbouring particle b, that is

$$V_b = \frac{m_b}{\rho_b} \tag{2.5}$$

and $W_{ab} = W(|\mathbf{r}_a - \mathbf{r}_b|, h)$ is the kernel function of particles a and b. The value of $A_a(\mathbf{r})$ is "smoothed" by the kernel function $W_{ab} = W(|\mathbf{r}_a - \mathbf{r}_b|, h)$. For simplicity of notation, $W(|\mathbf{r}_a - \mathbf{r}_b|, h)$ was replaced by W_{ab} in the following text.

Another feature of SPH is that spatial derivative of any function $A(\mathbf{r})$ is only derived to kernel function by ordinary differentiation in mathematics. There is no need for a grid, which is necessary in Eulerian method. The derivative of any function $A(\mathbf{r})$ can be calculated from equation (2.3) as

$$\nabla A(\mathbf{r}) = \int A\left(\mathbf{r}'\right)\nabla W\left(\mathbf{r}-\mathbf{r}', h\right)d\mathbf{r}' \tag{2.6}$$

Writing equation (2.6) in the form of summation of the value of neighbour particles, the derivative of any function $A(\mathbf{r})$ in the position of particle a can be approximated by a discrete form of neighbouring particles

$$\nabla A_a(\mathbf{r}) = \sum_b m_b \frac{A_b}{\rho_b}\nabla W(\mathbf{r}_a - \mathbf{r}_b, h) \tag{2.7}$$

where $\mathbf{r}_a$ and $\mathbf{r}_b$ are the position of particle a and particle b, respectively. Similarly, if $A(\mathbf{r})$ is a vector, the divergence of $A(\mathbf{r})$ in the position of particle a in the discrete form becomes

$$\nabla \cdot A_a(\mathbf{r}) = \sum_b m_b \frac{A_b}{\rho_b}\cdot\nabla W(\mathbf{r}_a - \mathbf{r}_b, h) \tag{2.8}$$

2.2 The kernel function

2.2.1 Introduction

Kernel functions are fundamental in the SPH scheme, being analogue to the different basis functions in a finite element method or the difference schemes in finite difference method. It is so called “smoothing function” or “weighting function” in other literatures (Gomez-Gesteira et al., 2010; Randles and Libersky, 1996a). Naturally, several kinds of smoothing functions have been proposed by many researchers to satisfy different order of accuracy required in their applications.

Lucy (1977) used the bell-shaped function as the kernel function at first, while Monaghan (1992) suggested that assuming the kernel function being a Gaussian is a good physical interpretation of an SPH equation. A spline-based function, the cubic spline kernel function which is being applied widely in the hydrodynamics research, was devised by Monaghan and Lattanzio (1985). After that, more spline smooth functions with higher order, such as quadratic smoothing

function and quantic smoothing function (Morris, 1994; Morris, 1996), were devised by other researchers. Liu and Liu (2003) summarized and described the equations and graphs of Gaussian kernel and the spline kernels as well as their derivatives, and also stated the advantages and disadvantages of each of the kernel function in terms of accuracy, smoothness and stability.

For example, the Gaussian smooth function has sufficient smoothness even for high order derivatives, but it is not of compact support theoretically (Liu and Liu, 2003). While the cubic spline smooth function has a narrower compact support, which is good for efficiency in numerical calculation. But the second derivative of the cubic spline smooth function is a discontinuous function. Usually, the un-smoothness of derivatives can lead to error accumulation in the simulation (Xu et al., 2009) when the particle disorder starts to occur and program breaks down eventually.

2.2.2 Properties

The kernel function must have the following properties either for mathematical reasons or for physical reasons (Liu and Liu, 2003):

(1) The kernel function can be normalized over its support domain

$$\int_{\Omega} W\left(\mathbf{r}-\mathbf{r}^{'},h\right)d\mathbf{r}^{'}=1 \tag{2.9}$$

where Ω is the volume of the fluid domain of interest. This property ensures the sum of the contribution of all neighbour particles equals to one.

(2) The kernel function must converge to a Dirac Delta function as the smoothing length approaches to zero as shown in equation (2.10).

$$\lim_{h\to 0} W\left(\mathbf{r}-\mathbf{r}^{'},h\right)d\mathbf{r}^{'}=\delta\left(\mathbf{r}-\mathbf{r}^{'}\right) \tag{2.10}$$

This property makes sure that the approximation value of reference particle is the original value of reference particle when smoothing length approaching to be zero.

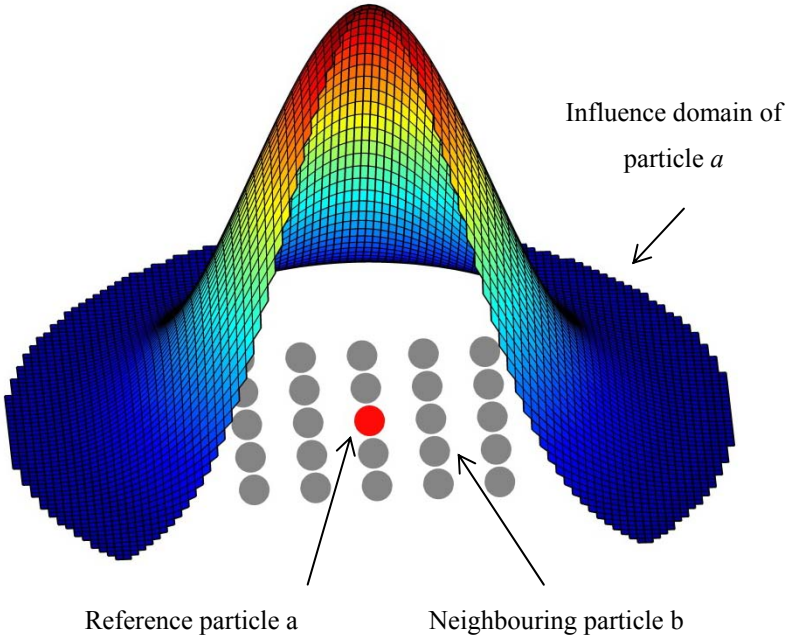

Figure 2.2. Schematic representation of kernel function in SPH method

(3) The kernel function needs to be supported compactly

$$W\left(\mathbf{r}-\mathbf{r}^{'}\right)=0,\ \text{for}\ \left|\mathbf{r}-\mathbf{r}^{'}\right|>\kappa h \tag{2.11}$$

where κ is a scaling factor, which can determine the dimension of the support domain together with smoothing length h.

This means only those particles located closely around the reference particle can be included in the summation of the approximation interpolation equations. Usually, we call them neighbouring particles of the reference particle in SPH as shown in Figure 2.2. Therefore, this property can help to reduce the computational efforts.

(4) The value of the kernel function should be positive for any particle $\mathbf{r}^{'}$ within the support domain.

$$W\left(\mathbf{r}-\mathbf{r}'\right)\geq 0 \tag{2.12}$$

This property is a requirement for obeying the physical phenomena in SPH simulation used in some field, especially in hydrodynamic simulations. Negative value of the kernel function can results in negative physical quantity in density, which is clearly wrong in reality.

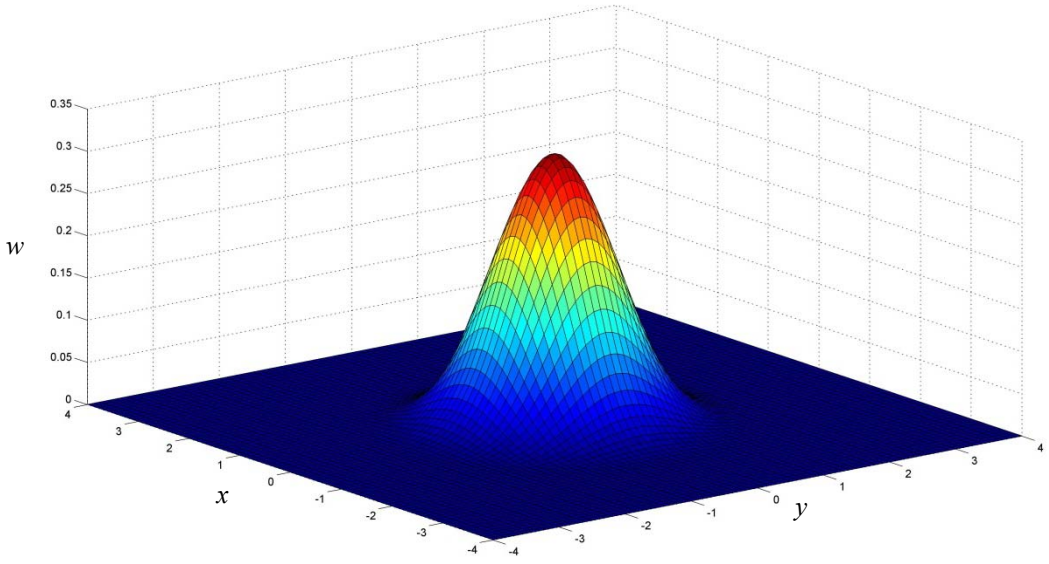

Figure 2.3. The kernel function when $\nu = 2$

(5) The value of the kernel function should be reducing with the increase of the distance away from the reference particle as shown in Figure 2.3. In other words, the influence decreases when a neighbour particle is away from the reference particle. This is consistent with particle interaction in reality.

More details or summary of the properties of the property can be found in the book of Liu and Liu (2003).

2.2.3 Cubic spline kernel function

As mentioned above, the cubic spline kernel function based on the spline function developed by Monaghan and Lattanzio (1985) has been used widely to solve many kinds of hydrodynamic problems, and it has the following form

$$W(r,h)=\frac{\sigma}{h^{\nu}}\begin{cases}\left(1-\frac{3}{2}q^2+\frac{3}{4}q^3\right) & 0\le q\le 1\\ \frac{1}{4}(2-q)^3 & 1\le q\le 2\\ 0 & q>2\end{cases} \tag{2.13}$$

where $r=$ the separation distance between the reference particle and neighbouring particle, and $q=r/h$ are the relative distance. With ν denoting the dimensionality of the simulation, the normalization constant σ has the value as below (Monaghan and Lattanzio, 1985)

$$\sigma=\begin{cases}\frac{2}{3} & \nu=1\\ \frac{10}{7\pi} & \nu=2\\ \frac{1}{\pi} & \nu=3\end{cases} \tag{2.14}$$

The value of the kernel function depends on the relative distance and the smoothing length. The smoothing length decides the range of the kernel function and it is usually a constant in the SPH simulation. The radius of the extent of kernel function is set to be double of the smoothing length here.

As shown in Figure 2.2, only particles within the double smoothing length contribute to the values of the reference particle. This kernel function has the advantage of possessing compact support, the second derivative being continuous and the kernel is of second order accuracy in the numerical scheme. In literatures, a fifth-order kernel has been used by Xu et al. (2009) to develop the particle-shifting

ISPH technique. Here cubic spine kernel function with $\nu = 2$ is depicted in Figure 2.3.

The cubic spline kernel function is used in this research. It has the advantage of being close to the Guassian kernel function.

2.3 SPH formulas

In the previous sections, the basic concepts and essential derivations of SPH method have been provided. With regard to the fluid particles in an SPH framework, the Lagrangian form of the Navier-Stokes equations is written as follows:
The continuity equation

$$\frac{1}{\rho}\frac{d\rho}{dt} + \nabla \cdot \mathbf{u} = 0 \tag{2.15}$$

The momentum equation

$$\frac{d\mathbf{u}}{dt} = -\frac{1}{\rho}\nabla P + \mathbf{g} + \frac{1}{\rho}\nabla \cdot \vec{\boldsymbol{\tau}} \tag{2.16}$$

where $\rho =$ fluid particle density; $t =$ time; $\mathbf{u} =$ particle velocity; $P =$ pressure; $\vec{\boldsymbol{\tau}} =$ shear stress tensor; and $\mathbf{g} =$ gravitational acceleration.

The full derivative d/dt of a vector field $\mathbf{u}$ is defined by

$$\frac{d\mathbf{u}}{dt} = \frac{\partial \mathbf{u}}{\partial t} + (\mathbf{u} \cdot \nabla)\mathbf{u} \tag{2.17}$$

The left hand side of equation (2.17) is just the time derivative of the velocity of particles in SPH.

In this section, the SPH formulations, which are written in the form of summation of discrete points, are derived for all the corresponding quantities and operators in the Navier-Stokes equations in Lagrangian form.

2.3.1 The continuity equation

All the physical quantities (including scalar and vector) in the SPH framework are approximated by employing equation (2.4). For example, the density of particle a is expressed in the fluid zone by:

$$\rho_a = \sum_b m_b W_{ab} \tag{2.18}$$

Although this summation density approach is used widely in SPH application, some modifications have been proposed to improve the accuracy of the approximation and suit the requirement of fluid flow simulation in SPH. One of the methods is to normalize equation (2.18) with the summation of the smoothing kernel function itself over all the neighbouring particles around particle a (Randles and Libersky, 1996b), as following

$$\rho_a = \frac{\sum_b m_b W_{ab}}{\sum_b \left(\frac{m_b}{\rho_b} \right) W_{ab}} \tag{2.19}$$

Apart from various quantities, the gradient, divergence and Laplacian operators are also parts of the governing equations. All of these will have to be included in the computation. As mentioned above the spatial derivatives of a variable is performed directly to the kernel function.

The divergence of velocity term is on the right hand side of the continuity equation. Normally, the divergence of a vector $\mathbf{u}$ at a given particle, a, can be estimated by (Monaghan, 1992)

$$\nabla \cdot \mathbf{u}_a = \sum_b m_b \mathbf{u}_b \cdot \nabla_a W_{ab} \tag{2.20}$$

where $\nabla_a W_{ab}$ is the gradient of the kernel function taken with respect to the positions of particle a. Equation (2.20) represents the basic form of the SPH divergence operator to any vector.

It was pointed out that employing the basic form of SPH divergence or gradient can yield the numerical non-convergence and instability (Oger et al., 2007). Two golden roles of SPH were presented by Monaghan (1992) to find a physical interpretation of an SPH equation: first, it is always best to assume the kernel is a Gaussian; second, rewrite formulae with the density placed inside operators. Considering the second golden rule of SPH, an alternative way is to rewrite the density inside the operator

$$\nabla \cdot \mathbf{u} = \left[\nabla \cdot \left(\rho \mathbf{u} \right) - \mathbf{u} \cdot \nabla \rho \right] \Big/ \rho \tag{2.21}$$

Combining equation (2.20) and equation (2.21) together, hence, the divergence of a velocity $\mathbf{u}$ at particle a can be formed as

$$\rho_a \left(\nabla \cdot \mathbf{u}_a \right) = \sum_b m_b \left(\mathbf{u}_b - \mathbf{u}_a \right) \cdot \nabla_a W_{ab} \tag{2.22}$$

Finally, the continuity equation which represents the conservation of mass can be written as for fluid flow simulation in SPH (Monaghan, 1992)

$$\frac{d\rho_a}{dt} = \sum_b m_b \mathbf{u}_{ab} \cdot \nabla W_{ab} \tag{2.23}$$

where $\mathbf{u}_{ab} = \mathbf{u}_a - \mathbf{u}_b$ is velocity difference. This equation shows clearly that the time increment of density of a particle is the relative velocities between this particle and all the neighbouring particles in the support domain in SPH simulation.

2.3.2 The momentum equation

The gradient of the pressure at the right hand side of the momentum equation (2.16) can also be written in many different ways. Similar to equation (2.22), the pressure gradient of particle a can be obtained by replacing vector velocity $\mathbf{u}$ with scalar pressure P

$$\rho_a \left(\nabla P \right)_a = \sum_b m_b \left(P_b - P_a \right) \nabla_a W_{ab} \tag{2.24}$$

In order to ensure the linear and angular momentum conservation exactly, it was proposed by Monaghan (1992) that it is better to form the pressure gradient term to a symmetrical SPH equation by rewriting $\nabla P/\rho$ according to

$$\frac{\nabla P}{\rho} = \nabla\left(\frac{P}{\rho}\right) + \frac{P}{\rho^2}\nabla P \tag{2.25}$$

After some simple mathematical manipulation the following symmetric pressure gradient is obtained and used in this study.

$$\left(\frac{1}{\rho}\nabla P\right)_a = \sum_b m_b \left(\frac{P_a}{\rho_a^{\,2}} + \frac{P_b}{\rho_b^{\,2}}\right)\nabla_a W_{ab} \tag{2.26}$$

where the summation is over all the neighbouring particles other than particle a itself. Similarly, the divergence of a vector $\mathbf{u}$ in the continuity equation (2.15) at a given particle a also can be estimated by the following symmetric form.

$$\nabla\cdot\mathbf{u}_a = \rho_a \sum_b m_b \left(\frac{\mathbf{u}_a}{\rho_a^{\,2}} + \frac{\mathbf{u}_b}{\rho_b^{\,2}}\right)\cdot\nabla_a W_{ab} \tag{2.27}$$

Equations (2.20), (2.22) and (2.24) have an asymmetric, which means that it is not the same when swapping the places of particle a and particle b. Obviously, equation (2.26) and equation (2.27) are in symmetric forms, which makes sure the conservation of linear and angular momentum exactly in the simulation.

The turbulent shear stress term at the right side of momentum equation (2.16) can also be formulated by following the derivation method of the above gradient or divergence operators as (Shao and Lo, 2003)

$$\left(\frac{1}{\rho}\nabla\cdot\overrightarrow{\boldsymbol{\tau}}\right)_a = \sum_b m_b \left(\frac{\overrightarrow{\boldsymbol{\tau}}_a}{\rho_a^{\,2}} + \frac{\overrightarrow{\boldsymbol{\tau}}_b}{\rho_b^{\,2}}\right)\cdot\nabla_a W_{ab} \tag{2.28}$$

where the stress tensor $\overrightarrow{\boldsymbol{\tau}}$ is related to the strain tensor $\overrightarrow{\Delta}$ in the tensor form as

$$\overrightarrow{\boldsymbol{\tau}}_{ij} = \overrightarrow{\boldsymbol{\tau}}_{ji} = \mu_{\text{eff}}\,\overrightarrow{\Delta}_{ij} \tag{2.29}$$

where μ_{eff} is the effective viscosity, and $\vec{\Delta}_{ij}$ is defined by

$$\Delta_{ij} = \frac{\partial u_i}{\partial x_j} + \frac{\partial u_j}{\partial x_i} \tag{2.30}$$

However, while applying equation (2.30) to SPH particles instead of grid points, the full derivative between two particles *a* and *b* is first derivative by applying the finite difference derivation. Then it can be decomposed into *x* and *y* directions in two-dimension simulation, or *x*, *y* and *z* directions in three-dimension.

$$\left(\frac{\partial u_i}{\partial x_j}\right)_a = \left(\frac{\partial u_i}{\partial r_{ab}}\right)\left(\frac{\partial r_{ab}}{\partial x_j}\right)^{-1} \tag{2.31}$$

$$\left(\frac{\partial u_i}{\partial x_j}\right)_a = \frac{(u_i)_a - (u_i)_b}{r_{ab}} \frac{(x_j)_a - (x_j)_b}{r_{ab}} \tag{2.32}$$

Where r_a and r_b are the position of particle a and b, respectively; $r_{ab} = r_a - r_b$. The viscosity coefficient μ_{eff} has a constant value μ in the condition of water being the fluid.

Besides, the density of particle *a* and *b* can be assumed as (Khayyer et al., 2008)

$$\rho_a = \frac{\rho_a + \rho_b}{2};\ \rho_b = \frac{\rho_a + \rho_b}{2} \tag{2.33}$$

Combining equations from equation (2.28) to equation (2.32), and complying incompressibility to the procedure via continue equation, the SPH formulation of viscous term can be simplified from equation (2.28) to equation (2.34) without considering the turbulence in the SPH simulation (Shao and Lo, 2003).

$$(\nu_0 \nabla^2 \mathbf{u})_a = \sum_b m_b \frac{2(\nu_a + \nu_b)}{\rho_a + \rho_b} \frac{\mathbf{u}_{ab}\mathbf{r}_{ab} \cdot \nabla_a W_{ab}}{|\mathbf{r}_{ab}|^2 + \eta^2} \tag{2.34}$$

Where ν_0 is the molecular kinematic viscosity and has the relationship $\nu_0 = \mu/\rho$ with the dynamic viscosity μ and density ρ. ν_a and ν_b are the molecular kinematic viscosities of particle a and b, respectively; η is a small number to keep the denominator not zero and is commonly set to $0.1h$ (Shao and Lo, 2003).

2.3.3 The Poisson equation

The pressure Poisson equation in ISPH is

$$\nabla \cdot \left(\frac{1}{\rho_*} \nabla P_{t+1} \right) = \frac{\rho_0 - \rho_*}{\rho_0 \Delta t^2} \tag{2.35}$$

where $\Delta t =$ time increment; ρ_0 is initial and constant particle density; $\rho_* =$ intermediate particle density.

The Laplacian operator can be formulated in the same way as other operators by using the standard method. Due to the high sensitivity of pressures to particle disorder, the Laplacian (second derivative) in the pressure Poisson equation is formulated through a hybrid of the standard SPH first order derivative and difference method (Shao and Lo, 2003) as

$$\nabla \cdot \left(\frac{1}{\rho} \nabla P \right)_a = \sum_b m_b \frac{8}{\left(\rho_a + \rho_b \right)^2} \frac{P_{ab} \mathbf{r}_{ab} \cdot \nabla_a W_{ab}}{\left| \mathbf{r}_{ab} \right|^2 + \eta^2} \tag{2.36}$$

where $P_{ab} = P_a - P_b$ and $\mathbf{r}_{ab} = \mathbf{r}_a - \mathbf{r}_b$; and η is the same as mentioned in equation (2.34).

Though different from the form of equation (2.27) and equation (2.28), this Laplacian operator with respect to pressure is also in symmetric form. Cummins and Rudman (1999) formulated a similar equation for the pressure term in Poisson equation (Cummins and Rudman, 1999). The symmetric form can lead to a symmetric coefficient matrix of the linear pressure equations after discretization. As obtaining the solution of pressure Poisson equations is the most time consuming part of a program, a symmetric coefficient matrix allows the equations to be more efficiently solved by available mathematical solvers (Shao and Lo, 2003).

Chapter 3

Two types of ISPH Model

3.1 Introduction

ISPH were rooted in the projection concept of Cummins and Rudman (1999), and is widely applied in the free surface flows now. Two general modelling techniques exist in ISPH, density-invariant ISPH and velocity divergence-free ISPH. The density-invariant ISPH was initially proposed by Shao and Lo (2003) and uses the density difference as source term in the PPE. The velocity divergence-free ISPH was initially proposed by Hu and Adam (2007) and Lee et al. (2008) and uses the divergence of flow velocity field as source term in the PPE.

Extensive applications of ISPH for the fluid impact problems have disclosed that the density-invariant and velocity divergence-free approaches cannot provide identical impact pressure and force predictions, although both schemes were consistent in satisfying the incompressible principles. For example, Xu et al. (2009) found that the divergence-free ISPH method cannot maintain the stability in certain situations although it is fairly accurate before the instability sets in, while the density-invariant ISPH method is stable but often associated with the random-noise like disturbances. On the other hand, Cummins and Rudman (1999) and Hu and Adam (2007) found that if only a discrete velocity divergence-free condition is enforced, larger density-variation or particle clustering may occur due to the spatial truncation errors of the discretization scheme and the density errors can accumulate during long time computations.

Both Hu and Adams (2007) and Xu et al. (2009) have tried to combine both source terms alternatively in the solution of PPE but this was carried out at the expense of increased CPU time. To make use of the advantages of both projection

schemes, Asai et al. (2012) and Qin et al. (2014) combined both the density-invariant and divergence-free terms in a simple and straightforward PPE source term representation and found that the wave impact predictions on the collapse of a water column can be much improved. Similar combination technique was also adopted in other particle-based method like the Consistent Particle Method (CPM) (Koh et al., 2013).

3.2 Governing equations

The governing equations for simulating the dynamic fluid flows are the mass and momentum conservation equations. The commonly used set of partial differential equations is Navier-Stokes equations. Navier-Stokes equations written in the Lagrangian form, equations (2.15) and (2.16), are employed as the basic governing equations in this study.

In the condition of incompressible flows, the continuity equation (2.15) becomes

$$\nabla \cdot \mathbf{u} = 0 \tag{3.1}$$

This equation will be used in the derivation of the pressure Poisson equation.

3.3 Numerical procedures

The primary numerical procedures of ISPH model can be seen simply as the projection method for solving the governing equations -- Navier-Stokes equations. By using the fractional steps, the Navier-Stokes equations (2.15) and (2.16) are solved by the prediction–correction method in the incompressible SPH approach, which is based on the two- step projection scheme of Chorin (1968). Cummins and Rudman (1999) first introduced the SPH projection method to enforce the incompressibility in a correction step.

The first step-- the prediction step is an explicit integration in the time, based on the stress tensor and the gravitational force. So the intermediate particle velocity and position are calculated from the momentum equation without pressure gradient term as:

$$\Delta \mathbf{u}_* = \left(\mathbf{g} + \frac{1}{\rho} \nabla \cdot \overset{\Rightarrow}{\boldsymbol{\tau}} \right) \Delta t \tag{3.2}$$

$$\mathbf{u}_* = \mathbf{u}_t + \Delta \mathbf{u}_* \tag{3.3}$$

$$\mathbf{r}_* = \mathbf{r}_t + \mathbf{u}_* \Delta t \tag{3.4}$$

where $\Delta \mathbf{u}_*$ = changed particle velocity during the prediction step; Δt = time increment; $\mathbf{u}_t$ and $\mathbf{r}_t$ = particle velocity and position at time t ; $\mathbf{u}_*$ and $\mathbf{r}_*$ = intermediate particle velocity and position.

Then the second step-- the correction step, the pressure gradient term is incorporated into the momentum equation (2.16) to enforce the incompressibility. Once being solved in a fully implicit way, the pressure is then involved to correct the particle velocity by using equation (3.5), equation (3.6) as below

$$\Delta \mathbf{u}_{**} = -\frac{1}{\rho_*} \nabla P_{t+1} \Delta t \tag{3.5}$$

$$\mathbf{u}_{t+1} = \mathbf{u}_* + \Delta \mathbf{u}_{**} \tag{3.6}$$

Finally, the new particle positions are centered by equation (3.7) after obtaining the corresponding velocity at the current time step.

$$\mathbf{r}_{t+1} = \mathbf{r}_t + \frac{\mathbf{u}_{t+1} + \mathbf{u}_t}{2} \Delta t \tag{3.7}$$

where ρ_* = intermediate particle density after the prediction step; P_{t+1} = particle pressure; and $\mathbf{u}_{t+1}$ and $\mathbf{r}_{t+1}$ = particle velocity and position at time $t+1$, respectively.

Figure 3.1 shows the flow chat of the ISPH computation process.

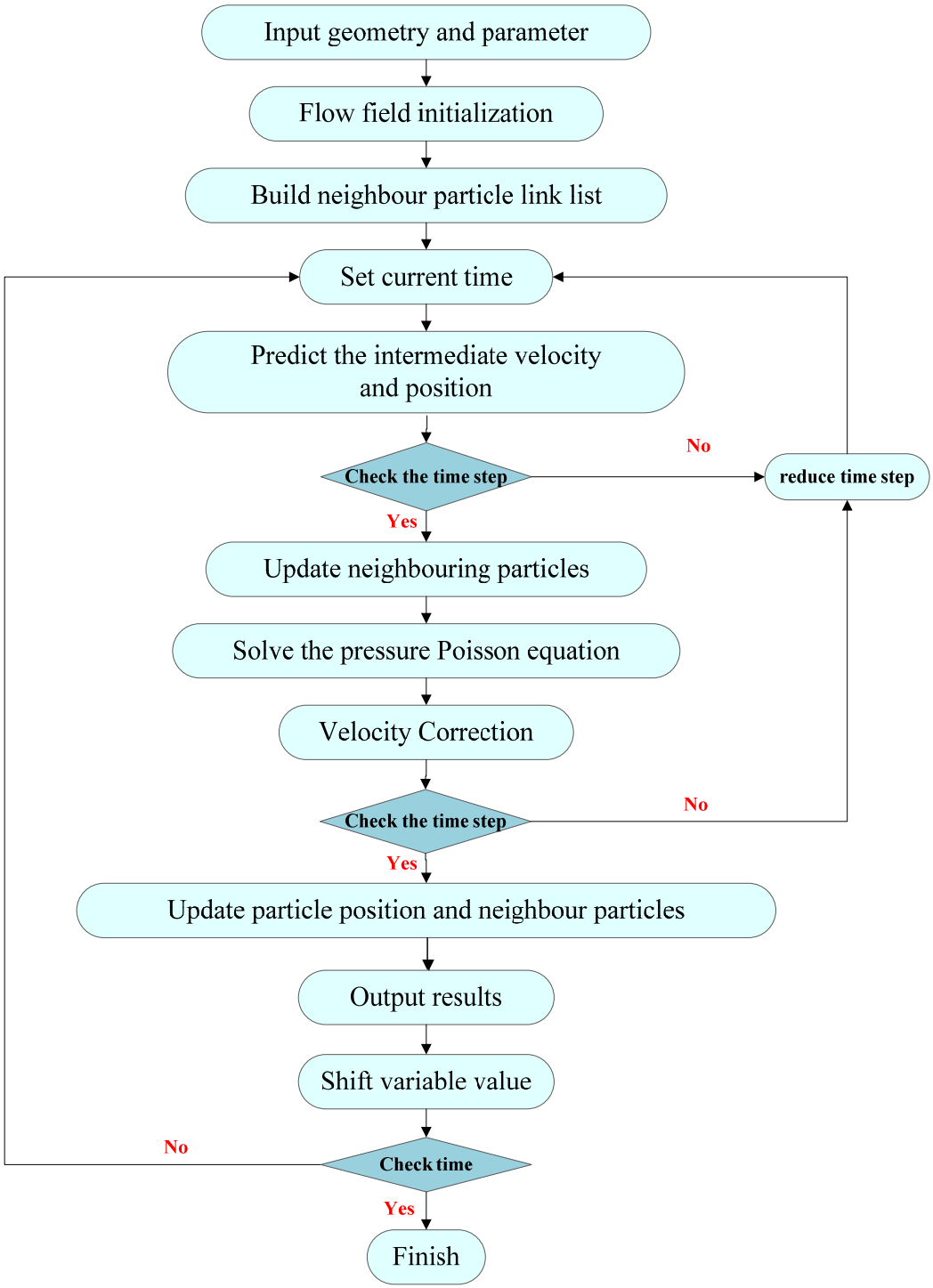

Figure 3.1. Flow chat of codes in ISPH model

3.4 Two types of Poisson equation

There are two different source terms in the ISPH pressure calculation, i.e. density invariant ISPH and velocity divergence free ISPH. The former uses the density difference as the source term in the PPE while the latter uses the divergence of flow velocity field. The density invariant ISPH was initially proposed by Shao and Lo (2003) for a dam-break free surface flow and later used by Shao (2005) for the solitary wave impact on a curtain wall and by Khayyer and Gotoh (2009b) and Khayyer et al. (2009) for breaking wave impacts on the structure. On the other hand, the velocity divergence free ISPH was initially proposed by Cummins and Rudman (1999) for the non-free surface flows and later modified by Lee et al. (2008) for the existence of the free surface. This approach has also been widely used in wave impact applications such as documented by Khayyer and Gotoh (2010).

It has been found that the density invariant ISPH has more strict incompressibility requirement and thus could generate relatively larger numerical forces during the wave impact, while the divergence free ISPH has less incompressibility requirement and thus produced a relatively stable and smoothed pressure curve. The former has more particle oscillations while the latter has less. For the practical wave impact applications, either applying the density invariant ISPH or the divergence free ISPH may not be able to achieve the best performance for the area of interest. In this section, the derivative of both of the Pressure Poisson equation will be given in detail.

3.4.1 Density invariant PPE

On the one hand, the Density invariant PPE can be deducted by writing the mass conservation equation (2.15) in the discrete form at the intermediate time step first.

$$\frac{1}{\rho_0}\frac{\rho_* - \rho_0}{\Delta t} + \nabla \cdot \mathbf{u}_* = 0 \tag{3.8}$$

Then enforcing the incompressibility as

$$\mathbf{u}_{t+1} = \mathbf{u}_* + \Delta\mathbf{u}_* \tag{3.9}$$

$$\nabla \cdot \mathbf{u}_* = -\nabla \cdot \left(\Delta\mathbf{u}_* \right) \tag{3.10}$$

Substituting the above equation into equation (3.8), the following equation can be obtained

$$\frac{1}{\rho_0} \frac{\rho_0 - \rho_*}{\Delta t} + \nabla \cdot \left(\Delta\mathbf{u}_{**} \right) = 0 \tag{3.11}$$

where $\rho_0 =$ initial constant particle density.

Combining equation (3.5) and equation (3.11), Shao and Lo (2003) gave the classical pressure Poisson equation based on the relative density variance as follows:

$$\nabla \cdot \left(\frac{1}{\rho_*} \nabla P_{t+1} \right) = \frac{\rho_0 - \rho_*}{\rho_0 \Delta t^2} \tag{3.12}$$

3.4.2 Velocity divergence-free PPE

On the other hand, through adding the velocity relation equation (3.6) to equation (3.5), we can get the following relation.

$$\mathbf{u}_{t+1} - \mathbf{u}_* = -\frac{1}{\rho_*} \nabla P_{t+1} \Delta t \tag{3.13}$$

Here, by projecting the intermediate velocity field onto a divergence-free space, the divergence of equation (3.6) can be written as:

$$\nabla \cdot \left(\frac{\mathbf{u}_{t+1} - \mathbf{u}_*}{\Delta t} \right) = -\nabla \cdot \left(\frac{1}{\rho_*} \nabla P_{t+1} \right) \tag{3.14}$$

As for a truly incompressible approach, density is constant and thus equation (2.15) is reduced to the following formulation in discrete form for enforcing the incompressibility:

$$\nabla \cdot \mathbf{u}_{t+1} = 0 \tag{3.15}$$

It should be noted that the intermediate velocity field $\mathbf{u}_*$ is usually not a divergence free. By considering a constant density and combining equation (3.14) and equation (3.15), the following pressure Poisson equation with the velocity divergence free source term is obtained (Lee et al., 2008):

$$\nabla \cdot \left(\frac{1}{\rho} \nabla P_{t+1} \right) = \frac{\nabla \cdot \mathbf{u}_*}{\Delta t} \tag{3.16}$$

3.5 Time step

Since the flow evolves quickly over time in coastal structure studies, the time step is an essential part of the time integration for approximations to the governing equations of flow field. The time step is one of the most important parameters for accurate, reliable efficient numerical simulation of time dependent flow. Less computational time is needed for running the programme with large time step. But the programme might break down with larger time step sometimes when the flow changes rapidly or free surface experiences violent deformation. Small time step was chose in order to achieve numerical stability and accuracy, resulting in large computation consume inevitably.

The time step Δt is determined according to the Courant–Friedrichs–Lewy condition in our model.

$$\Delta t \leq 0.1 \frac{l_0}{V_{max}} \tag{3.17}$$

where l_0 = initial particle spacing and V_{max} = maximum particle velocity at each time step. As shown in equation (3.17), the value of the Courant number is 0.1 according to Shao and Lo (2003).

The viscous diffusion also impose restrictions on the time step by

$$\Delta t \leq \alpha \frac{l_0^2}{\nu_0 + \nu_t} \tag{3.18}$$

where α is the coefficient depending on the type of smoothing function and particle arrangement. α is usually the order of 0.1 (Lo and Shao, 2002).

However, an adaptive time step is applied in our model. By calculating right hand side of equation (3.17) and checking the relation between two sides after each time step, the model can be adjusted to increase or reduce the value of time step Δt automatically, which will be used in the next time step.

The adjustment is done as follows:

$$\Delta t_{n+1} = 0.9\Delta t_n \tag{3.19}$$

or

$$\Delta t_{n+1} = 1.1\Delta t_n \tag{3.20}$$

where Δt_n is the current time step, and Δt_{n+1} is the next time step. The coefficients in equation (3.19) and equation (3.20) are obtained according to repeated numerical calibration. This scheme can balance the accuracy and the computational efficiency as compared to using a fixed small time step during the whole simulations.

3.6 Boundary conditions

The original SPH was developed for astrophysics study, which has no boundary in the simulation. Since being introduced to the study of hydrodynamics, the boundary condition has always been an important aspect related to the successful calculation. Here, the boundary condition for the incompressible flow usually includes the following four parts: solid wall, free surface, wave maker and absorbing boundaries. Regarding to these boundaries, the variables that are most concerned with are velocity and pressure which should satisfy Neumann boundary or Dirichlet boundary conditions.

3.6.1 Solid Boundaries

Generally, in order to fulfil the physical boundary condition, solid walls are represented by fixed wall particles with the same particle distance as the inner fluid particles as shown in Figure 3.2 (a).

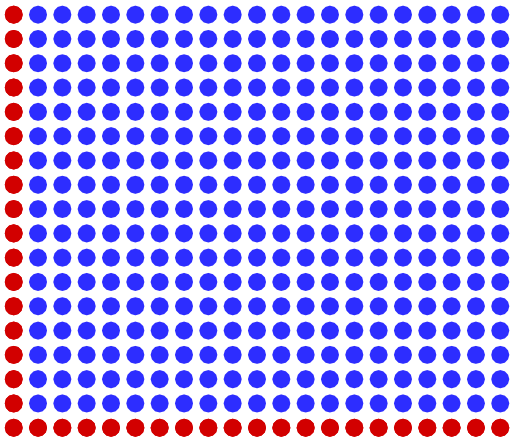

(a)

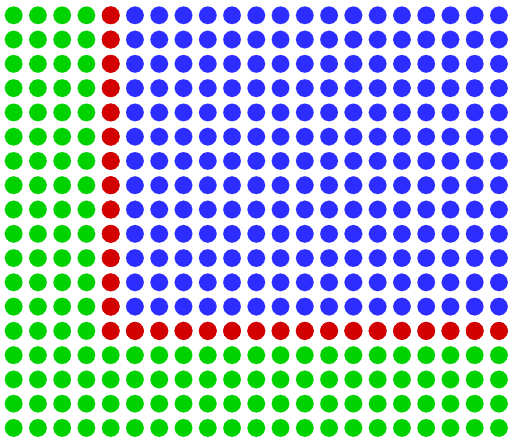

(b)

Figure 3.2. Wall particle definition, red dot: wall particles, blue dot: water particles; green dot: dummy particles

The wall particles should balance the pressure of the inner fluid particles and keep them at appropriate distance from the solid wall, neither penetrating nor going

far away. The velocity boundary conditions are no-slip boundary at solid wall in all the following study. The boundary condition for the velocity and pressure along the wall is expressed by (Cummins and Rudman, 1999)

$$\mathbf{u}_{t+1} = 0 \tag{3.21}$$

$$\frac{\partial p_{t+1}}{\partial n} = 0 \tag{3.22}$$

Cummins (1999) mentioned that these boundary treatments do not satisfy the correct pressure boundary conditions for the incompressible Navier-stokes equations (Gresho and Sani, 1987), but it works well with projection method in SPH.

Since the kernel compact support zone is truncated for a particle near the wall, three approaches have commonly been applied to implement the Dirichlet boundary for the velocity and Neumann boundary for the pressure in ISPH to maintain the fluid particles inside the inner zone: Monaghan (1994) proposed the solid boundary approach that is well known as the repulsive force method. In addition, the mirror particles, which are the reflections of the inner fluid particles within certain support distance from the solid boundary (Cummins and Rudman, 1999), are also widely used. The last approach is called the dummy particle method. As usual, several layers of dummy particles are regularly placed outside along the solid boundary and fixed in space throughout the whole simulations (Shao and Lo, 2003) as shown in Figure 3.2 (b).

3.6.1.1 Density invariant ISPH

In this method, the wall particles are also included in the pressure Poisson equation (3.12). The velocities of the wall particles are set zero to represent the non-slip boundary condition. Several lines of dummy particles are used in order to keep the fluid density at the wall particles to be consistent with that of the inner fluids as shown in Figure 3.2 (b). The layer thickness of the dummy particles can be found in (Shao and Lo, 2003).

3.6.1.2 Velocity divergence-free ISPH

Some literatures have revealed that the fluid particles can penetrate the solid wall which is represented by the stationary particles using the velocity divergence source term. Monaghan and Kajtar (2009) analysed the effect of reducing the boundary particle spacing to certain ratios of the inner fluid particle spacing and showed that the calculation accuracy can be guaranteed without further increasing the computing time. Here I still use the dummy particle method for its simplicity and effectiveness. However, the reduced boundary particle spacing is adopted to prevent the inner fluid particles across the wall boundary. The schematic diagram of the reduced wall particles spacing is shown in Figure 3.3.

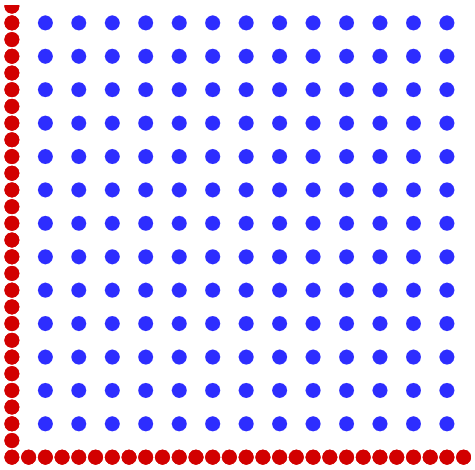

Figure 3.3. Wall boundary, red dot: wall particles, blue dot: water particles

In addition, more layers of the dummy particles are used because more neighbouring particles are needed for the calculation of velocity divergence in the pressure Poisson equation. The schematic diagram of the dummy particles is shown in Figure 3.4. The number of layers required depends on both the boundary particle spacing and the inner fluid particle spacing.

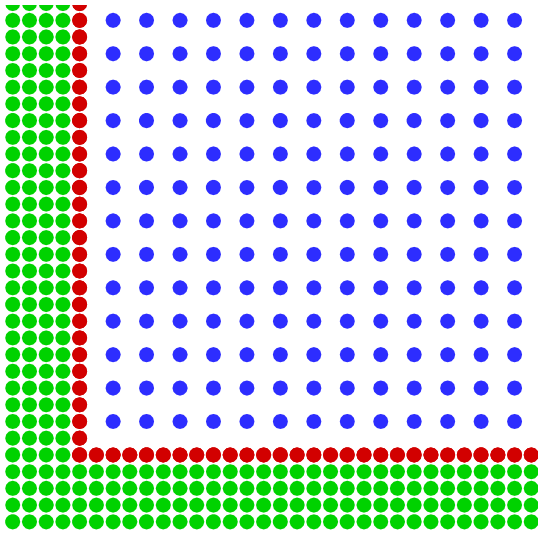

Figure 3.4. Dummy particles, red dot: wall particles, blue dot: water particles, green dot: dummy particles

3.6.2 Free surfaces boundary

Particles contacting with the air are regards as the free surface particles. As for the free surface particles, the number of their neighbouring particles is significantly less than that of the inner fluid particles, since no particle exists in the outer region of the free surface as shown in Figure 3.5.

So the free surface particles can be easily identified by the particle density which drops sharply (Shao and Lo, 2003) as compared with the inner fluid particle density, due to the truncated support zone of the kernel. According to our computational experiences, if the density drop of a particle is below 1% – 10% of the reference value, it can then be regarded as being on the free surface. Usually it makes no difference in identifying the surface particles whether the value of 1% or 10% is used.

A zero pressure is applied to these surface particles in ISPH while the Neumann solid boundary condition is given for solving the pressure Poisson equation. The divergence of particle positions was also used to identify the surface particles (Lee et al., 2008). Similarly, Khayyer et al. (2009) introduced a new surface criterion based on the particle symmetries, in which the summation of either *x*-

coordinate or *y*-coordinate of the particles is used to compare with the initial particle spacing.

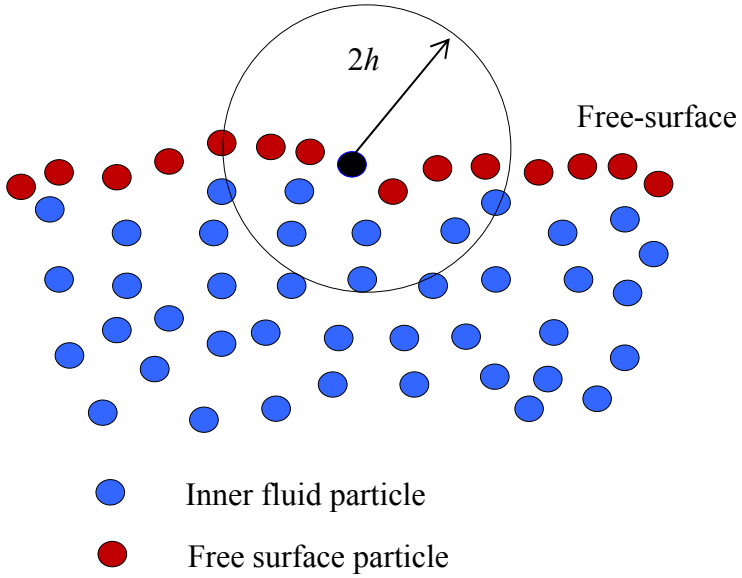

Figure 3.5. Schematic of free surface particles; light blue circle: free surface particles; blue circle: particles under free surface

3.6.3 Wave maker boundary

Normally, the inlet boundary is the position of setting the wave condition used in the study for an open system. In our study, solitary wave will be used to verify and validate the proposed model, because solitary wave is frequently considered to have certain characteristics of tsunamis, storm surges and other long period waves which are of great importance in coastal engineering.

The profile of solitary wave is similar to the curve of normal distribution as shown in Figure 3.7. The wave length is infinite theoretically, as well as the period. Solitary wave is very stable and can keep its profile unchanged during propagation.

The mathematical solution of solitary wave is a function of x and time t, derived from the Boussinesq equations (Lee et al., 1982) as below

$$\eta(x,t) = A\,sec\,h^2\left[\sqrt{\frac{3A}{4d^3}}(x-ct)\right] \tag{3.23}$$

where $\eta =$ water surface elevation, $A =$ wave amplitude or wave height, $d =$ water depth, and the speed of the wave c is given by

$$c = \sqrt{g\left(d + A\right)} \tag{3.24}$$

Generally, a wave paddle is put at one side of the water flume to generate waves and the displacement of the wave paddle can be obtained by the following equations (Ghadimi et al., 2012; Goring, 1979; Orszaghova, 2011),

$$X_P\left(t\right) = \frac{A}{kd} tanh\left(k\left(X_P\left(t\right) - ct\right)\right) \tag{3.25}$$

where $k = \sqrt{\frac{3A}{4d^3}}$.

Since the above equations are implicit and not easy for coding, instead of generating wave with the wave paddle at the incident side of the water flume, other method of generating solitary wave was discussed by Monaghan and Kos (1999) and Shao and Lo (2003) through involving a pile of particles regularly above the free surface at the incident side of the computation domain. The free surface line of these particles is approximate to the profile of the solitary wave described by equation (3.23). The velocities of those particles under the surface were also initialled by equation (3.26). The horizontal velocity at a given point can be calculated by

$$u = \eta\sqrt{g / d} \tag{3.26}$$

At the beginning stage of the simulation, a slightly jagged (Monaghan and Kos, 1999) and unsmoothed surface profile occurred at these points which are the change points of different particle level of vertical position, for instance, the point a and b as shown in Figure 3.6. But this phenomenon will disappear within a few time steps, well before wave reaching the concerned area.

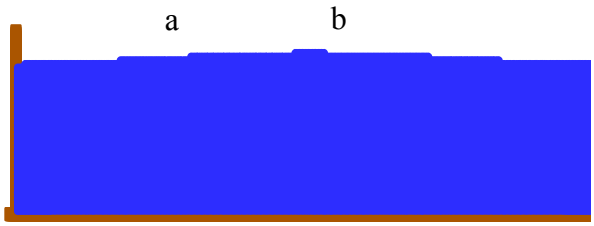

Figure 3.6. Solitary wave generated by putting a pile of particles regularly above the free surface; points a and b are the change points of different particle level of vertical position

Though the methods of Monaghan and Kos (1999) and Shao and Lo (2003) are easy and effective, a very long distance should be required at the incident side of the computational zone duo to the wave length being infinite theoretically. Considering that above two methods are rather complicated and computationally expensive. Orszaghova (2011) proposed a new method which inputs the motion signal directly through a time series data of wave paddle displacement and speed instead. The time series of wave paddle displacement and speed can be obtain from the thesis of Orszaghova (2011).

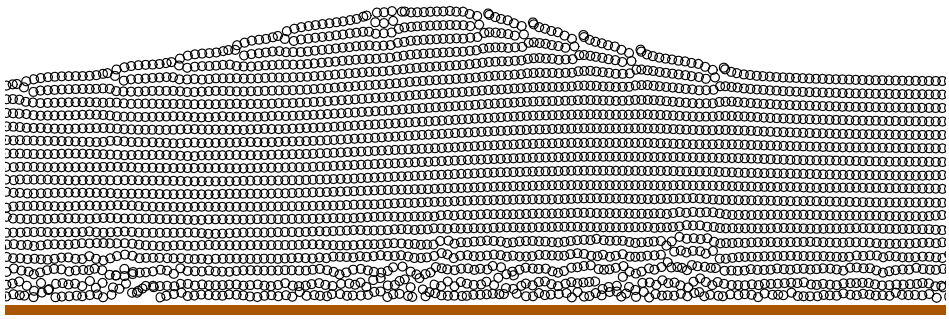

Figure 3.7. Solitary wave in SPH

Figure 3.7 shows the profile of solitary wave generated using the new method in SPH. The result of the free surface in the water tank is smooth enough and fluid

particles are in a regular order. All these indicate that it is and effective and accurate way to generate solitary wave by inputting the time series of wave paddle displacement and speed directly.

3.6.4 Absorbing boundary

In a laboratory flume, when the wave propagates toward the downstream boundary, mostly being a wall, wave reflection occurs and reflected wave will combine with the incident wave to act on the coastal structures. This is not in accord with the real wave condition in reality, where the wave usually goes out of the study zone without reflection.

By having a long enough distance at the downstream side of the simulation water tank, the reflection effect on the concerned area can be reduced. But sometimes it is not practical, especially when the simulation domain is large, requiring a large number of particles to achieve satisfactory accuracy. Also the ISPH model cannot run for an arbitrarily long time. Other method was proposed to solve the problem of wave reflection. For instant, Xu (2010) and Li et al (2012) set up a damping zone to absorb the wave reflection in a way widely used in Boussinesq model (Larsen and Dancy, 1983). Li et al (2012) has demonstrated this method can reduce the velocity effectively in ISPH.

In the damping zone, the fluid particle velocity is a function of the distance from the end side of the water tank, and the damping is as achieved using

$$U_d = U_0 f\left(x\right) \tag{3.27}$$

where U_d is the damped velocity, U_0 is the particle velocity at the start line $x = x_0$ of the damping zone. As for the damping function, it is expressed as

$$f\left(x\right) = 1 - e^{\left(-\beta\left(L_d - \left(x - x_0\right)\right)\right)} \tag{3.28}$$

According to Xu (2010) and Li et al (2012), the value of 2.0 may be chosen for β, and L_d is the length of the damping zone.

3.7 Turbulence

The turbulence is one of the significant aspects for violence flow simulation, especially for breaking wave simulation in the surf zone. As for the laminar flow simulation, the basic SPH model can produce good results. But for turbulence flow, usually, additional turbulence model should be incorporated in the simulation. Lately, a few different turbulence models have been proposed for SPH. For instant, Monaghan (2002; Monaghan, 2004) used a Lagrangian Averaged Navier-Stokes Alpha (LANS-α) model, which is based on the Lagrangian version of Large Eddy Simulation, to get the smoothed velocity and pressure. But this method turned out to be seriously time consuming for particle computation. Later, Violeau and Issa (2007) derived four different turbulence models (eddy viscosity assumption, Prandtl's one-equation model, standard $k-\varepsilon$ equations model and Reynolds Stress Model) for SPH and compared each of them through an open channel flow test. Through significant improvement has been achieved by using the Reynolds Stress Model, differences till exist between the SPH results and the benchmark experiment results. Instead of incorporating turbulence model to the SPH model, Mansour (2008) simulated the full range of turbulence scale via direct SPH numerical simulation and found out that the weakness of the SPH viscosity term at small scales yields weaker strength of inverse energy cascade than expected

Shao & Gotah (2004) first coupled incompressible SPH with Large Eddy Simulation (LES) for progressive wave interaction with curtain-wall type breakwater. Furthermore, LES-SPH model was developed by Shao et al. (2006) to simulate wave overtopping over a horizontal deck and a sea-wall. Dalrymple and Rogers (2006) also used Sub-particle scaling (SPS) combining with Smagorinsky model to simulate breaking waves in SPH method.

For resolving the turbulence effect in the small turbulence scales, the majority of SPH turbulence models focused on combining the Large Eddy Simulation with Smagorinsky model for the sub-grid scale. Based on that fact, Sub-Particle Scale (SPS) turbulence model is applied in this work to obtain the SPS

turbulence stress $\vec{\boldsymbol{\tau}}$. The turbulence stress $\vec{\boldsymbol{\tau}}$ was given in the terms of eddy viscosity

$$\tau_{ij}/\rho = 2v_T\overline{S}_{ij} - \frac{2}{3}k\delta_{ij} \tag{3.29}$$

in which v_T = turbulence eddy viscosity; $\overline{S}_{ij}$ are the components of the strain-rate tensor. δ_{ij} = Kronecker's delta and k = turbulence kinetic energy, which is calculated based on the turbulence model.

Here the widely used standard Smagorinsky model is employed to determine the turbulence eddy viscosity, which is assumed to be proportional to the mixing length ΔX and a characteristic turbulence velocity

$$v_T = \left(C_s\Delta X\right)^2\left|\overline{S}\right| \tag{3.30}$$

where C_s is the Smagorinsky constant, a range of 0.1-0.24 was quoted by Rogallo and Moin (1984). Furthermore, a value of 0.12 (Lo and Shao, 2002) is used here for the reason that Lo and Shao (2002) found it can gain good comparison of the computational results with experimental data of solitary wave breaking on a plane beach.

For the application in SPH, the mixing characteristic length ΔX is reasonably equal to the particle spacing. And $\left|\overline{S}\right|$ = local strain rate, which can be calculated from the resolved variables as below

$$\left|\overline{S}\right| = \left(2\overline{S}_{ij}\overline{S}_{ij}\right)^{1/2} \tag{3.31}$$

in which $\overline{S}_{ij}$ is expressed as

$$\overline{S}_{ij} = \frac{1}{2}\left[\frac{\partial u_i}{\partial x_j} + \frac{\partial u_j}{\partial x_x}\right] \tag{3.32}$$

$$\left(\frac{\partial u}{\partial x}\right)_{i:j} = \frac{u_{ij}}{r_{ji}}\frac{x_{ij}}{r_{ji}} = \frac{u_i - u_j}{r_{ji}}\frac{x_i - x_j}{r_{ji}} \tag{3.33}$$

Here letters i and j denote the spatial direct in x and y, respectively.

Chapter 4

Improved ISPH Model validations and applications

In the previous chapter, the deduction of both of standard source terms in the ISPH algorithm, the commonly used density invariant and velocity divergence free source terms, were described in detail. In this chapter the source term in the standard ISPH algorithm will be formulated into the form of the weighted average of the commonly used density invariant and velocity divergence free source terms at first. Then I will apply the new model to two different wave impact cases, i.e. dam-break flow impact on a wall and solitary wave impact on a beach house and determine the influence of each part in different wave impact situations.

Compared with the existing ISPH models and other similar particle modelling techniques, the key feature of the present model is that it includes both the density invariant and velocity divergence free terms in a simple combination and is computationally efficient involving no additional subroutines in SPH code, which makes it more suitable for the practical engineering application. The model improvement is directed at achieving better representation of wave impact pressures and forces rather than the wave surface profiles and flow velocities, as the former are more susceptible to the particle disorder and pressure noise.

The organisation of this chapter is as follows: The first section is the deduction of the mixed source term. The second section provides the model validation via applying to dam break impact problem. The third section is the application of solitary wave impact on a beach house and the influence of weighting coefficient on maximum wave impact. The fourth section contains a sensitivity analysis to investigate the influence of particle spacing on the weighting coefficient of the density invariant and velocity divergence free terms in the PPE and check the

convergence of numerical scheme. Finally, a semi-empirical approach is found to predict the weighting coefficient in PPE source term based on the energy damping principles.

4.1 Improved PPE source term treatment

Since the incompressible SPH method was introduced by Shao and Lo (2003) based on the density invariant principle, a lot of works have been done to improve this method. Though a variety of SPH techniques, such as the kernel corrections and density filters, were applied to reduce the pressure noises, it is also recognised that an improvement in the accuracy of the ISPH methods may be achieved through improving the PPE source term representation (Xu et al., 2009). Because particle oscillation is related direct to the solution of PPE.

One important development is the use of velocity divergence free source term (Colin et al., 2006; Lee et al., 2008). Recently, another development is that Hu and Adams (2007) and Xu et al. (2009) have tried to combine both source terms alternatively in the solution of PPE to improve the simulation accuracy but this was carried out at the expense of increased CPU time. Because they have solved two pressure Poisson equations separately and used each of them to correct the velocity field and particle positions. As it is a fairly time consuming process to solve two Poisson equations the application is only restricted to some simple flow phenomena.

Furthermore, Khayyer et al. (2009) applied both source term methods to simulate the wave interaction with structure. According to our previous computational experiences, it has shown that despite the velocity divergence source term in ISPH method enhances the accuracy of predictions it is much easier to cause the instability, commonly the particle penetration through the solid boundary (Lee et al., 2008). On the other hand, the ISPH method with the density gradient source term is quite stable but often generates random noises and disturbances for the particle properties.

Quite a few good studies have been carried out to improve the PPE solution in the Moving Particle Semi-implicit (MPS) method originally developed by Koshizuka et al. (1998). For example, Khayyer and Gotoh (2009) used a high-order source term and allowed a slight compressibility to investigate the wave impact problems. Khayyer and Gotoh (2011) further developed a high-order error compensating PPE source term to study different tensile instability problems. The most promising feature of this work was the use of dynamic coefficients in the error compensating terms as functions of the instantaneous flow field.

Kondo and Koshizuka (2011) also proposed a mixed source term formulation with the main part and error compensating part and carried out a detailed study on optimizing the weighting coefficients under the hydrostatic and dam-break conditions. As for the field of incompressible SPH, relatively few works have been documented except that Asai et al. (2012) proposed a hybrid PPE source term formulation combining a divergence free part and a relaxation part which is related to the density variance using a relaxation coefficient. However, as their density variance part was not based on the strict incompressible formulation, the weighting coefficient in their PPE was sensitive to the particle spacing and thus calibrations were always needed whenever the spatial resolution changed. Besides, as the weighting coefficient was calibrated under the hydrostatic condition, it is not quite clear to what extent it is still applicable to the nonlinear violent wave impact problems and how much errors would be generated.

Inspired by these approaches, it seems a good way to combine the two Poisson equations together rather than to solve them separately, so that the advantages of both methods can be fully explored. Though density on the left side of equation (3.12) and equation (3.16) is the intermediate density, it can be assumed as constant density here due to slight difference between intermediate density and constant density. The error rising from this assumption is negligible since the density is the denominator. While the intermediate density ρ_* won't be changed on the right side of the pressure Poisson equation (3.12), because the numerator and denominator are both small value and changing ρ_* may result in calculation failure.

Considering the fluid density being a constant, the left hand side of equation (3.12) and equation (3.16) should be the same. Adding a coefficient to each of the equations and combining them together, the following mixed source term representation can be obtained:

$$(\alpha+\beta)\nabla\cdot\left(\frac{1}{\rho}\nabla P_{t+1}\right)=\alpha\frac{\rho_0-\rho_*}{\rho_0\Delta t^2}+\beta\frac{\nabla\cdot\mathbf{u}_*}{\Delta t} \tag{4.1}$$

Where α and β are the coefficients in PPE source term, being both less than 1 and $\alpha+\beta=1$.

The proposed combined ISPH PPE source term inherits the advantages of both divergence free ISPH (with velocity divergence source term) and density invariant ISPH (with density gradient source term), and thus can maintain enough accuracy and stability while being at an efficient computational cost.

Here it should be noted that although Zhang et al. (2006) proposed similar PPE source term formulation as in this work, their model was based on the MPS solver and also the weighting coefficients in the PPE source term were treated as constants for different applications.

4.2 Case I: Wave impact in dam-break flows

4.2.1 Computation setup

The highly-deformed flows generated by the dam-break and their impact against a vertical wall have been widely used as a benchmark test case for the assessment of numerical methods (Lee et al., 2010) and thus this is also used here for testing the proposed mixed source term algorithms.

In this case, a rectangular column of water (0.68m wide and 0.12m high) is contained in a tank (1.18m wide) and the flows are allowed to move towards the right wall driven by the gravity. The configuration of the experimental setup is shown in Figure 4.1 and consistent with the numerical study of Khayyer et al. (2009) and the physical experiment of Hu and Kashiwagi (2004). In the figure, *A* denotes

the point where the pressure was recorded. The particle size used in the present ISPH simulation is D_0 = 0.004m, as also used in Khayyer et al. (2009). The bottom and walls of two sides are solid boundary. Referring to the same assumption of Khayyer et al. (2009), the boundary effects is not considered here. According the discussion of slip and non-slip boundary condition in Hu and Kashiwagi (2004), this assumption might lead to certain error of pressure after the first peak of pressure curve.

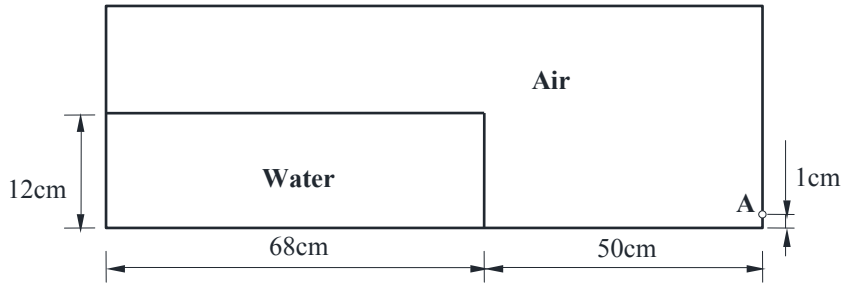

Figure 4.1. Schematic sketch of the simlated dam break problem

The most important task is to evaluate the weighting coefficient α that appeared in the PPE source term equation (4.1). As pointed out by Khayyer and Gotoh (2011) in their MPS formulations, coefficients of this type can be highly dependent on the nature of the flow conditions, thus I did not attempt to calibrate this coefficient by using some simpler flow cases, such as the hydrostatic problem. Instead I took a semi-empirical approach by following a trial-and-error procedure.

By examining equation (4.1), it could be anticipated that the weighting coefficient α would take smaller values in case of more violent wave impact problems such as when the flow surface is broken. In this situation, the divergence free part in PPE source term should contribute more to the stability and accuracy of the solution. On the other hand, in less violent wave breaking conditions or when the free surface is relatively smooth, α would take larger values so that the density invariance part contributes more to the solution. In the present computations, I started by using α = 0% (i.e. the PPE source term is totally a divergence free formulation) and gradually increased its value by a step of 1%, until the computed

peak pressure and whole curve are close to that reported in the experiment. Then I kept this α-value unchanged and carried out the whole simulation again in order to predict the arrival time of peak pressure and the pressure time histories. By adopting this procedure, the coefficient α = 5% was used in this dam-break flow test.

4.2.2 Results comparison

The snapshots of computed water particles and the pressure contours for the flow at different times t = 0.04, 0.1, and 0.2s are depicted in Figure 4.2. And times t = 0.34, 0.5, and 0.66s are depicted in Figure 4.3. Times t = 0.74, 0.8 and 1.0s are depicted in Figure 4.4. From Figure 4.2, it can be seen that the pressure distribution inside the fluid follows the hydrostatic law at the initiation of dam-break (t = 0.04s) and the maximum pressure is close to the hydrostatic pressure of 1200 N/m^2. At t = 0.1s a water tongue forms and flows along the horizontal wall after the dam water broke quickly. Later on this water tongue hits upon the vertical right wall and the peak impact pressure is generated at this instant. After this initial impact, the water tongue rises upwards along the wall and becomes a violent water jet with water spraying around. Soon later the jet overturns under the action of gravity and an air pocket is formed as shown at t = 0.66s from Figure 4.3. At later times as shown from Figure 4.4, the jet impacts on the underlying water surface and a secondary jet is generated from the impact point.

The velocity field of water particles with pressure contour at different times t = 0.04, 0.1, and 0.2s are depicted in Figure 4.5. And times t = 0.34, 0.5, and 0.66s are depicted in Figure 4.6. Times t = 0.74, 0.8 and 1.0s are depicted in Figure 4.7. From Figure 4.5, it can be seen that the particle velocities are small at the initiation of dam-break (t = 0.04s) and some particle velocities at left bottom are close to zero. At t = 0.1s particle velocities continue to increase and water tongue particles have the maximum velocity value. Later on water tongue hits upon the vertical right wall with large velocity. After this initial impact, the water tongue particles have large vertical velocity value. Soon later the jet overturns under the action of gravity and the horizontal velocity of particles are changed to the opposite direction at t = 0.66s as shown in Figure 4.7.

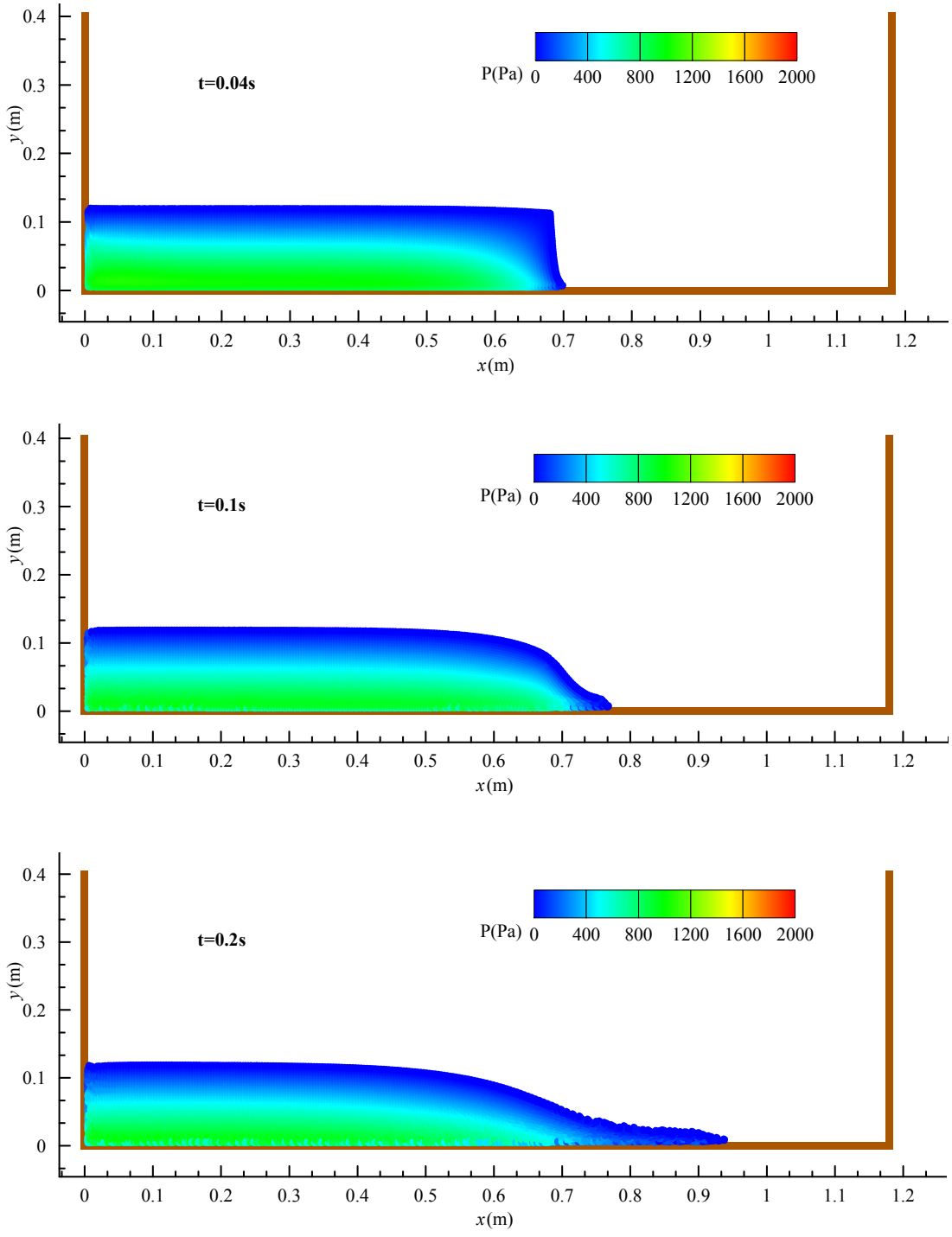

Figure 4.2. Snapshots of water particles with pressure contour at different times: t = 0.04s, 0.1s and 0.2s

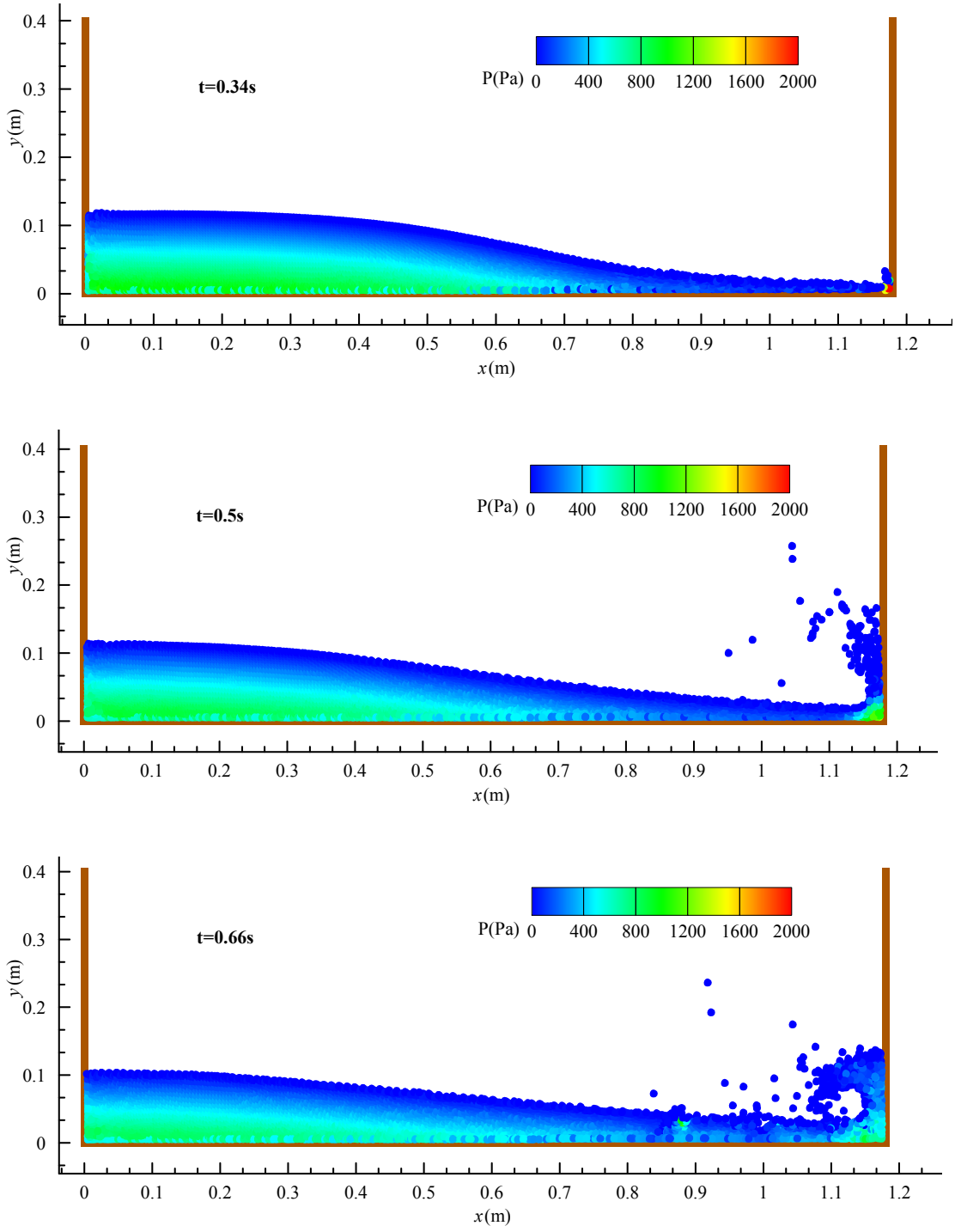

Figure 4.3. Snapshots of water particles with pressure contour at different times: t = 0.34s, 0.5s and 0.66s

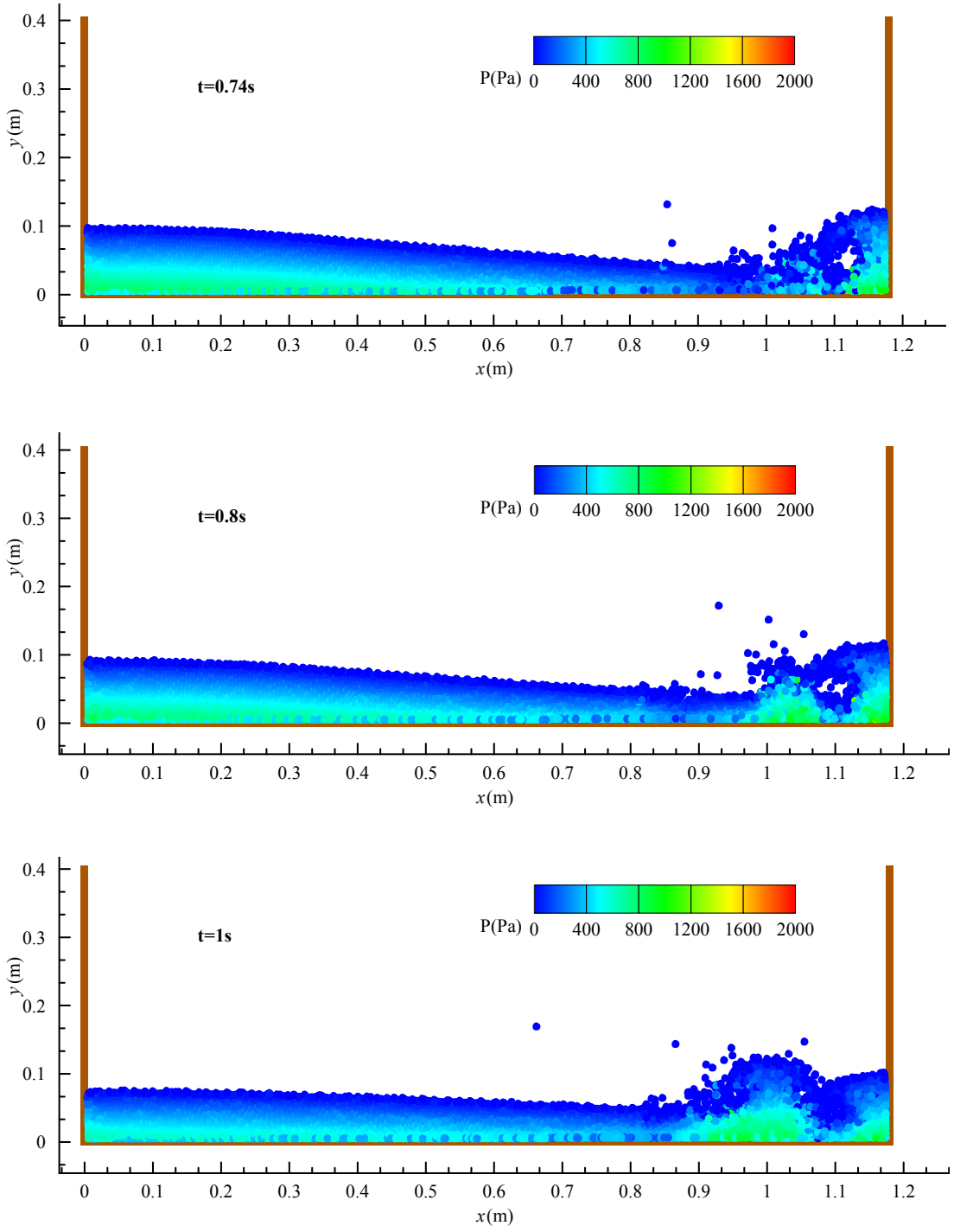

Figure 4.4. Snapshots of water particles with pressure contour at different times: t = 0.74s, 0.8s and 1s

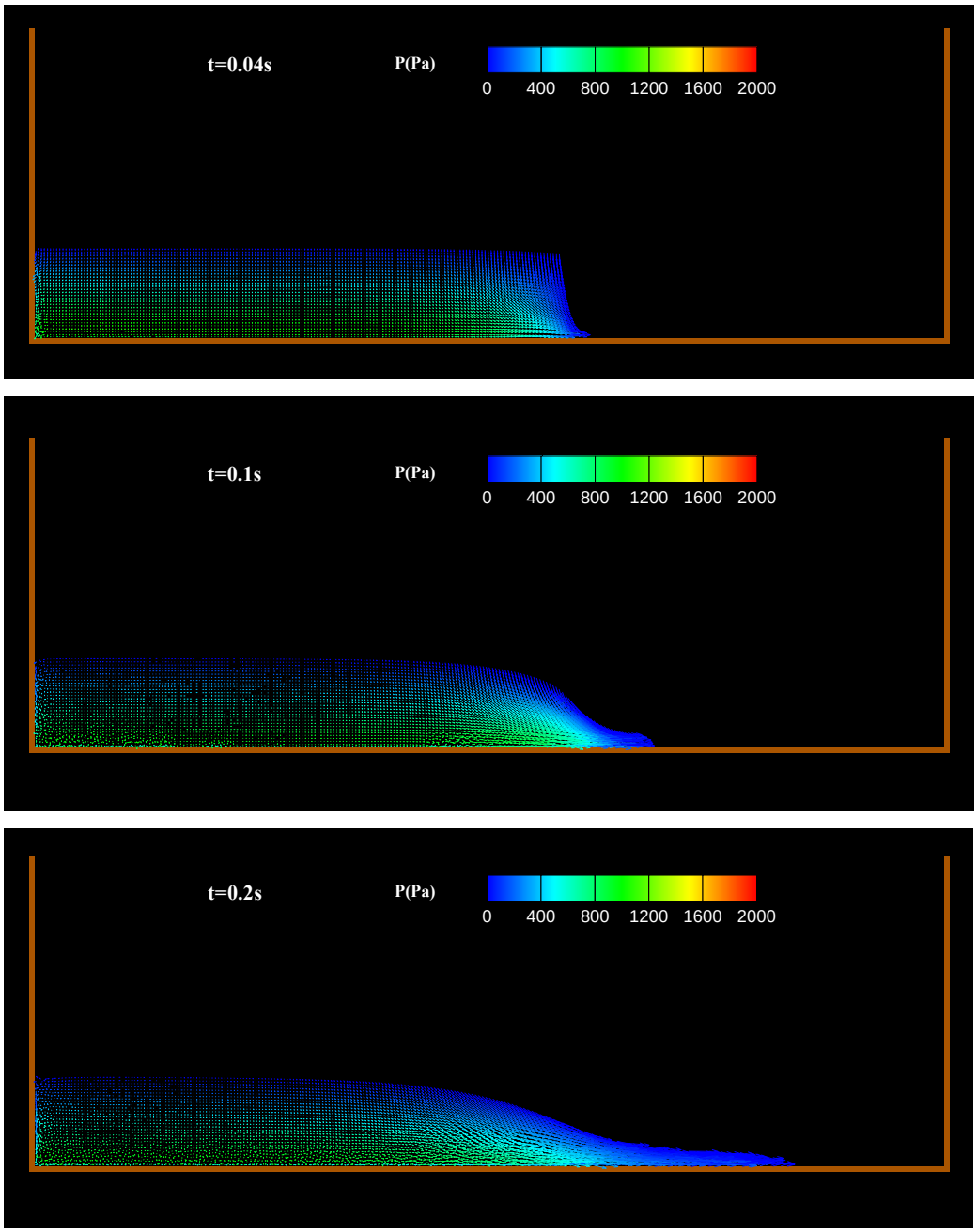

Figure 4.5. Velocity of water particles with pressure contour at different times: t = 0.04s, 0.1s, and 0.2s

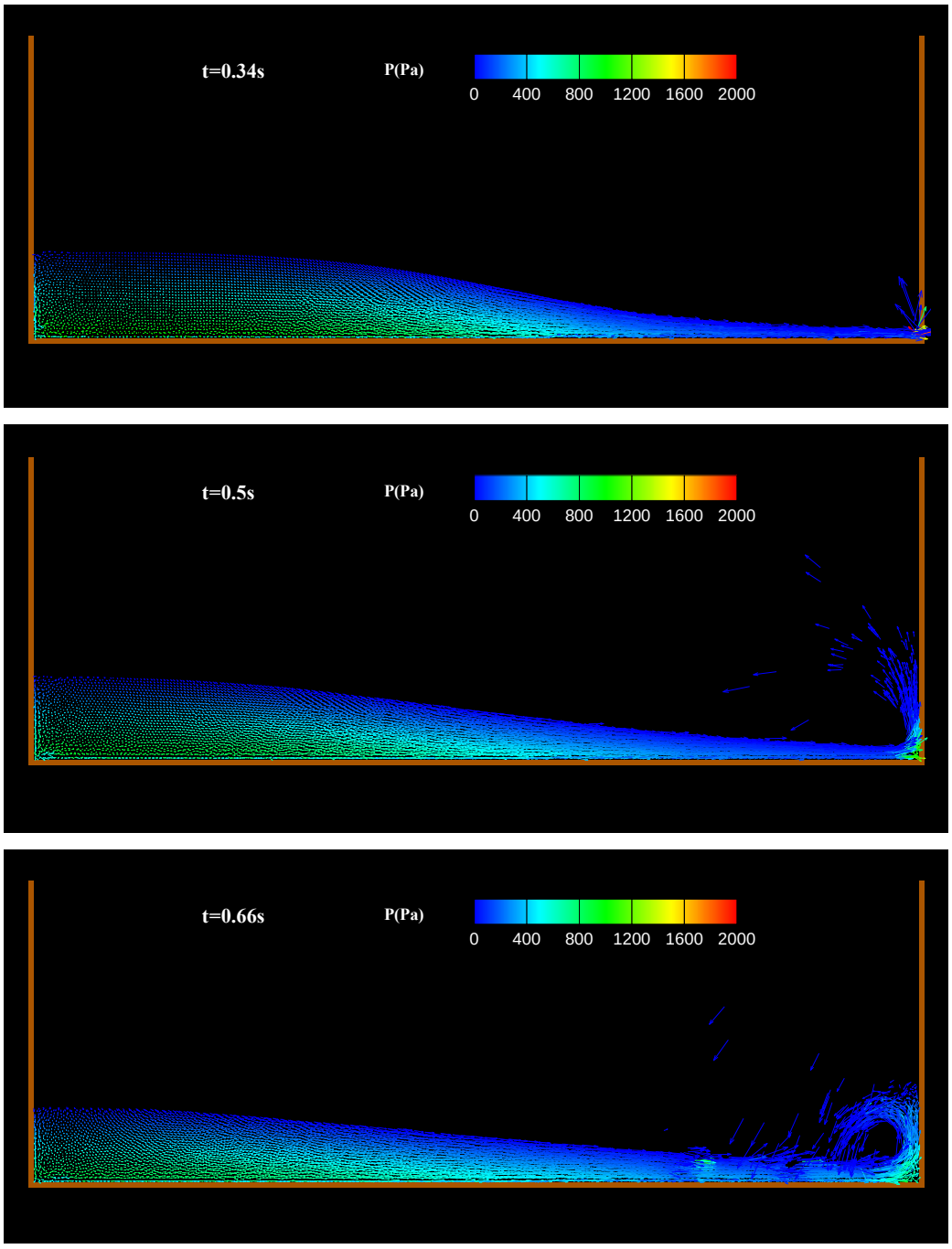

Figure 4.6. Velocity of water particles with pressure contour at different times: t = 0.34s, 0.5s, and 0.66s

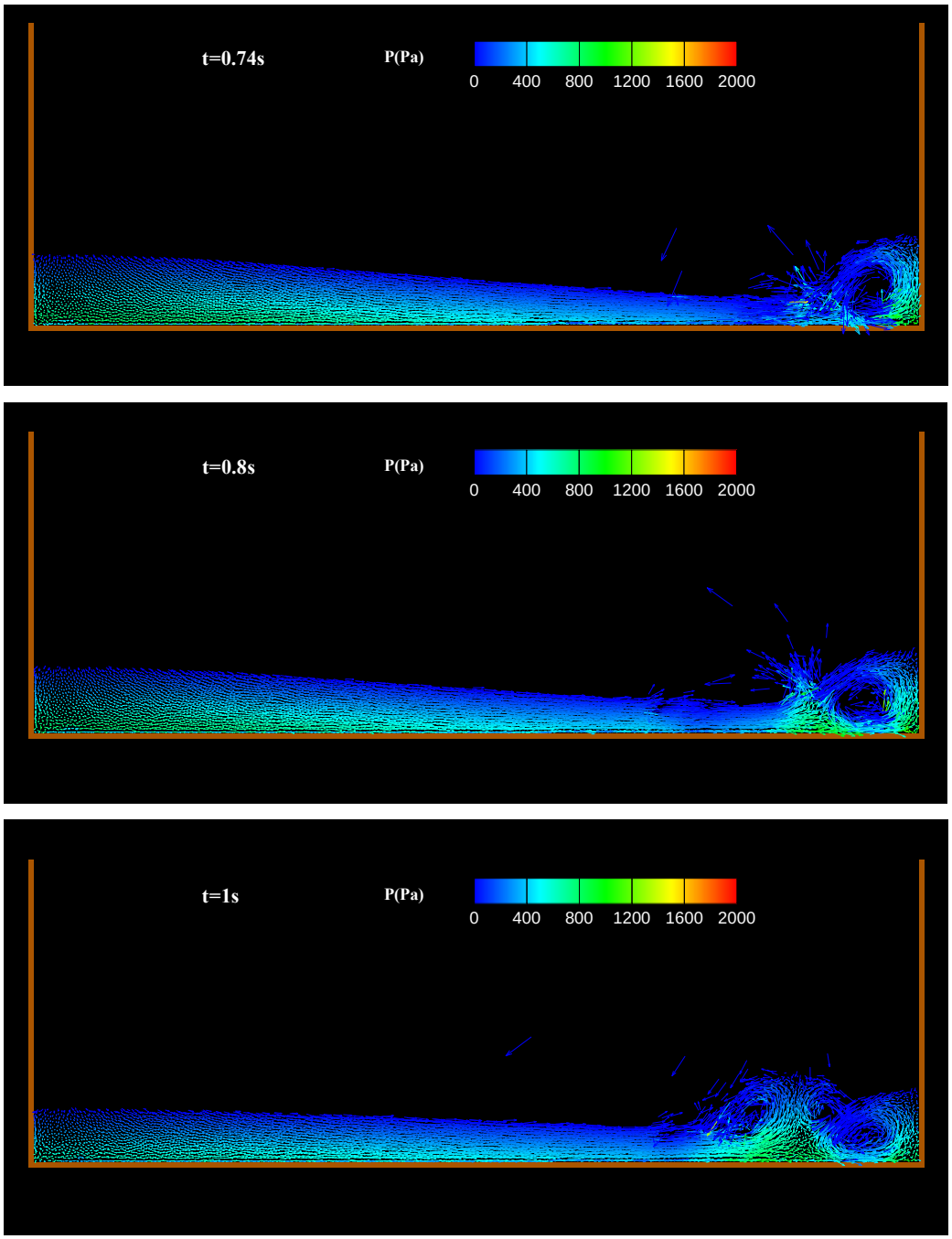

Figure 4.7. Velocity of water particles with pressure contour at different times: t = 0.74s, 0.8s and 1.0s

Figure 4.8 shows the time histories of the computed pressures at point A by ISPH using the mixed source term in pressure Poisson equation and the numerical

ISPH results of Khayyer et al. (2009), together with the laboratory data of Hu and Kashiwagi (2004). The laboratory data is the mean value of eight-time series of repeatedly measured pressure data. Although there was no precise information available on the sampling rate of the measured pressures in Hu and Kashiwagi (2004), the ISPH computational time step Δt being less than 0.001s suggested that the numerical sampling rate is likely to be much higher than the experimental one as indicated in their paper. Thus I could expect that the peak impact pressures were appropriately captured.

The computed pressure in SPH at measuring point *A* was obtained by interpolating the pressures of wall particles adjacent to point *A* on the right wall. In Figure 4.8, the green line with square represents the Corrected ISPH with Higher Order Source Term (CISPH-HS) results by Khayyer et al. (2009), who used a full velocity divergence free source term in their model. It shows that the first peak pressure of the experiment occurs at the instant when the dam-break wave hits the wall (t = 0.348s) with an averaged value of 1576.90 N/m^2, while the second peak is at t = 0.750s with an averaged value of 1192.30 N/m^2, which was a result of the first jet hitting on the underlying water surface. Both ISPH models (i.e. the one with the proposed mixed source term and the Khayyers' et al. (2009) overestimated the first peak, with a value of 1668.23 N/m^2 at t = 0.347s for the proposed ISPH and 1762.19 N/m^2 at t = 0.345s in Khayyer et al. (2009). This pressure over-prediction is most likely due to the influence of air compressibility, which was not taken into account in both the ISPH models. According to Peregrine (2003), a two-phase liquid-air formulation may be needed to more accurately capture the underlying physics during the violent wave impact process.

The second peak pressure calculated by Khayyer et al. (2009) slightly underestimated the experiment, which was 1177.72 N/m^2 at t = 0.752s, while the ISPH with mixed source term predicted a higher value of 1222.93 N/m^2 at t = 0.737s. However, it is shown that the computed pressure lines of Khayyer et al. (2009) showed some fluctuations and the results also contained several unreasonable zero-pressure points. To avoid these singular zero-pressures, additional surface boundary treatment was used in Khayyer et al. (2009). This illustrates that the pressure Poisson

equation with the proposed mixed source term can effectively reduce the pressure noises in a standard ISPH formulation, and meanwhile, good accuracy in predicting the peak impact pressures is achieved. However, the comparisons in Figure 4.8 indicated a relatively larger discrepancy between the numerical and experimental data after the first and second pressure peaks.

For the pressure overestimation after the second peak, a reasonable explanation is the 3D nature of the flow as Hu and Kashiwagi (2004) had observed that the flow at this stage in the experiment was already highly three-dimensional and severely broken. Therefore, a 2D simulation cannot be expected to reproduce the measurements precisely.

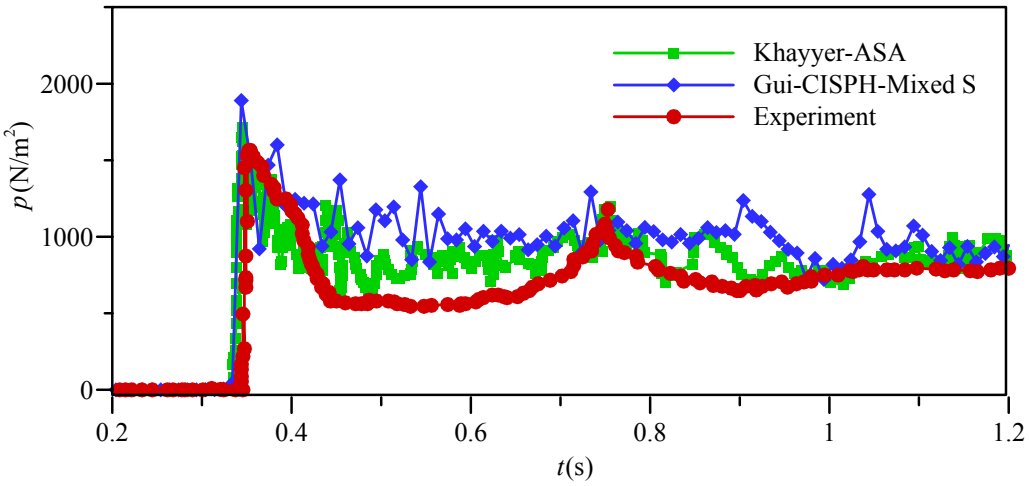

Figure 4.8. Time histories of computed and experimental pressures at measuring point A

As for the pressure over-predictions after the first peak which was also observed in the ISPH computational results of Khayyer et al. (2009), the exact nature of the problem is yet to be known but one possible cause may be related to the SPH treatment of the solid boundary conditions. Hu and Kashiwagi (2004) found that the enforcement of free-slip and non-slip boundaries could generate significant differences in the flow velocity and pressure structures near the solid wall corner, and thus change the pressure time histories. Another potential cause could be due to

the lack of two-phase representations in the present model, which cannot adequately address the effect of air compressibility during the violent dam break wave impact. As a final and perhaps most important cause, the flow turbulence is expected to be strong during the severe wave breaking after the first wave impact. As for this case, turbulence part is not considered in the model. So being lack of adequate energy damping mechanism, this computation is likely to over-predict the pressure histories.

It is well known that the incorporation of a velocity divergence-based source term will result in the violation of volume conservation. To evaluate the conservation of fluid incompressibility in the proposed mixed source term model, in which the proportion of density invariant part contains only 5%, I have calculated the time variations of particle densities and compared this with a strict density invariant ISPH model (Shao and Lo, 2003) in Figure 4.9.

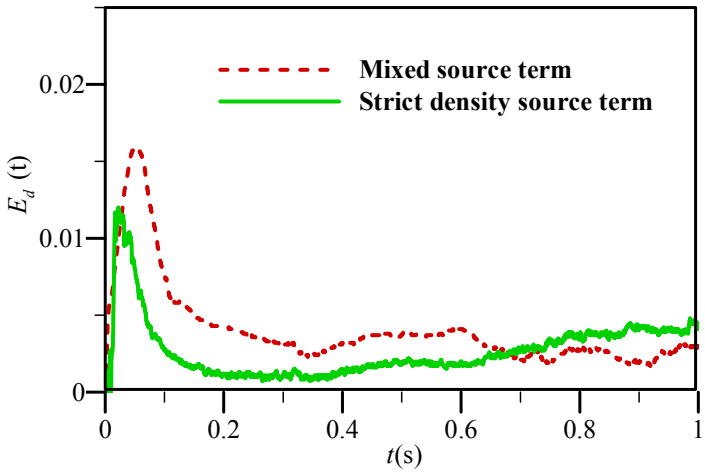

Figure 4.9. Time variations of normalized particle density errors in mixed source term and strict density invariant ISPH computations

The normalized particle density error was obtained by

$$E_d(t) = \frac{1}{N'} \sum_{i=1}^{N'} abs[\rho_i(t) - \rho_0] / \rho_0 \tag{4.2}$$

where ρ_i is the density of particle i calculated after correction step. $\rho_i(t)$ is the density time series of particle i. The summation is taken over the inner fluid particles only.

Figure 4.9 shows that the overall accuracy of the mixed source term model in view of satisfying the incompressibility is good, when being compared with a strict density invariant ISPH model. The maximum density error of the former is 0.016 and it is 0.012 for the latter. The density errors in both models increased at the beginning of computation due to the initial rapid adjustment of the particles, but decreased thereafter without further accumulation. The density errors started to re-rise slightly again after the first pressure impact around time t = 0.35s as a result of the large deformation of particles, but remained generally stable after that.

4.3 Case II: Solitary wave impact

4.3.1 Computation condition

The solitary wave propagating along a mild plane slope is a popular case to study wave interactions with the structures (Hsiao and Lin, 2010; Monaghan and Kos, 1999). The impact of a solitary wave on an idealized beach house has been simulated by Xiao and Huang (2008) by means of the incompressible Reynolds-average Navier-Stokes (RANS) model and $k-\varepsilon$ turbulence equations. In this section, the proposed ISPH model with mixed source term is used to study this case focusing primarily on calculating the wave run-up and the resulting wave force on the beach house. Because this case involves different wave flow features depending on the different locations the house is situated on the beach, it provides a good test for the PPE source term treatment presented herein.

Here two issues should be clarified: First, the wave run-up and breaking in the fields are always 3D but in this study I treated the problem as 2D, as the wave height to depth ratio is 2/5 which is not too high, and also no obvious violent wave breaking was observed in the computed run-up. Thus I expect a 2D representation could provide reasonable results at an efficient CPU load. Second, in this type of

engineering applications, the main concern is the structure stability requiring the determination of the total fluid force rather than fluid pressure at certain points. Thus the detailed impact pressure studies were not attempted in this section.

The slope of the planar beach is 1/20. The still water depth is 5m and the incident wave height is 2m. The dimension of the computational domain depends on the different house elevations. A solitary wave is generated at the offshore boundary by using the first order analytical solution for a solitary wave (Lo and Shao, 2002). The computational domain starts at 171m on the left boundary from the initial shoreline, including 100m of horizontal distance of the plane beach and 71m of the horizontal section wall as shown in Figure 4.10.

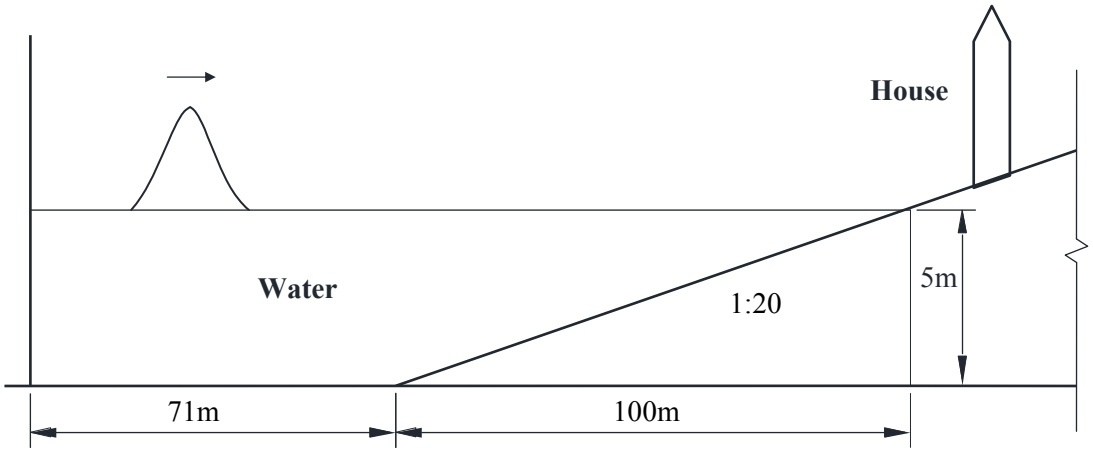

Figure 4.10. Schematic sketch of the solitary wave run-up, breaking and interaction with a beach house

The bottom, slope dike and walls of house are solid boundary. The initial wave crest is located 150m from the initial shoreline and the used ISPH particle spacing is D_0 = 0.2m. This spatial resolution is close to that used in Xiao and Huang (2008), in which a 0.3m × 0.1m uniform grid was used. According to Xiao and Huang (2008), the maximum vertical wave run-up height R was 2.52m. Then the idealized beachfront house is placed at different locations corresponding to five different fractions of the wave run-up height (-R/4, 0R, R/4, R/2, 3R/4). Here I will study all the situations when the beach house is located at or above or below the initial shoreline. Generally, the wave impact would be more violent due to the free surface

breaking as compared with the situation when the house is submerged under the water.

4.3.2 Results analysis and comparison

In the ISPH computations, by following the same procedure as used in the previous dam break flow study, I used the trial-and-error method to obtain the weighting coefficient α in the PPE source term equation (4.1) when the beach house is located at the initial shoreline. Then I fixed this value for all the other cases to compute the wave impact force to check the consistency of the coefficient. As expected, as these five house locations are all near the initial shoreline boundary and the nature of wave impacts should be similar, a unified weighting coefficient α around 50-60% worked quite well. It is also noted that in this solitary wave impact case, the wave flow situation is less violent (from free surface breaking) as compared with the previous dam break flow, so the weighting coefficient α becomes larger and both the velocity divergence free part and the density invariance part play an equal role in the PPE source term.

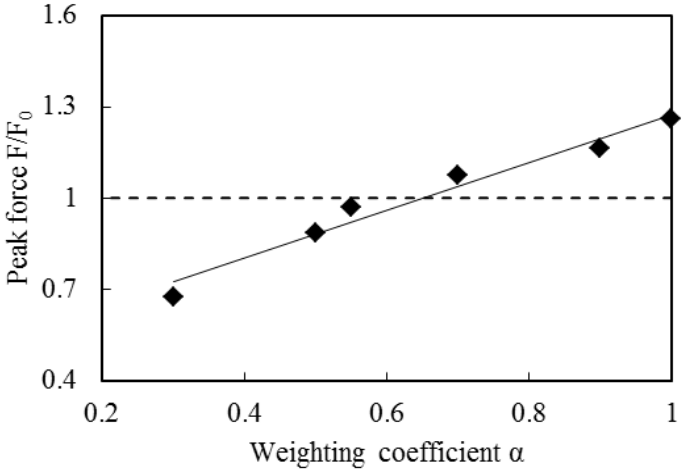

Figure 4.11. ISPH computed maximum wave forces based on different weighting coefficients α

To demonstrate the influence of weighting coefficient α in equation (4.1) on the maximum wave force predictions, Figure 4.11 shows a series of ISPH

computations based on different α values. It showed that the predicted peak force (normalized by the peak force F_0 in Xiao and Huang (2008), for the case of house location at initial shoreline 0R) varies from 0.65-1.25 for a variation of the weighting coefficient α from 0.3-1.0.

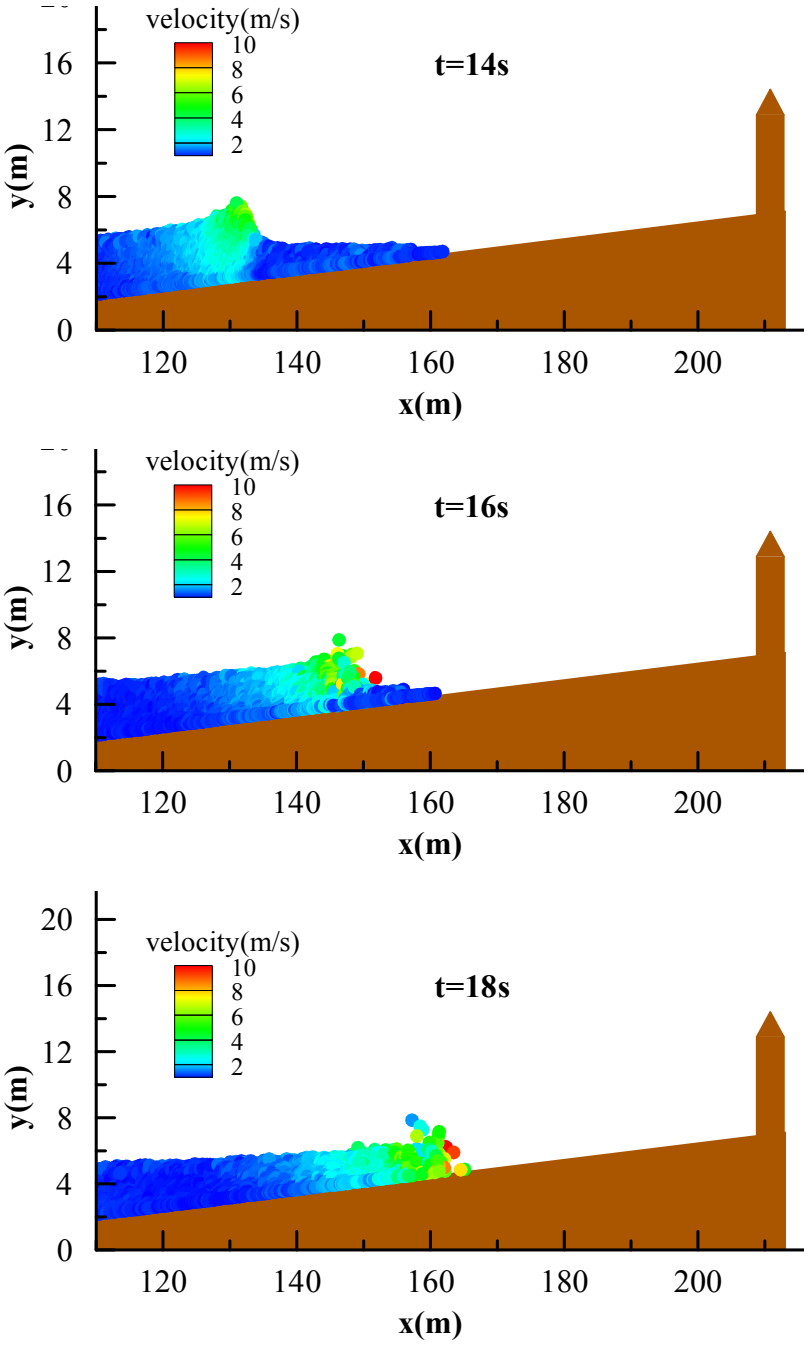

Figure 4.12. Wave run-up and interaction with the house located at 3R/4 above the initial shoreline

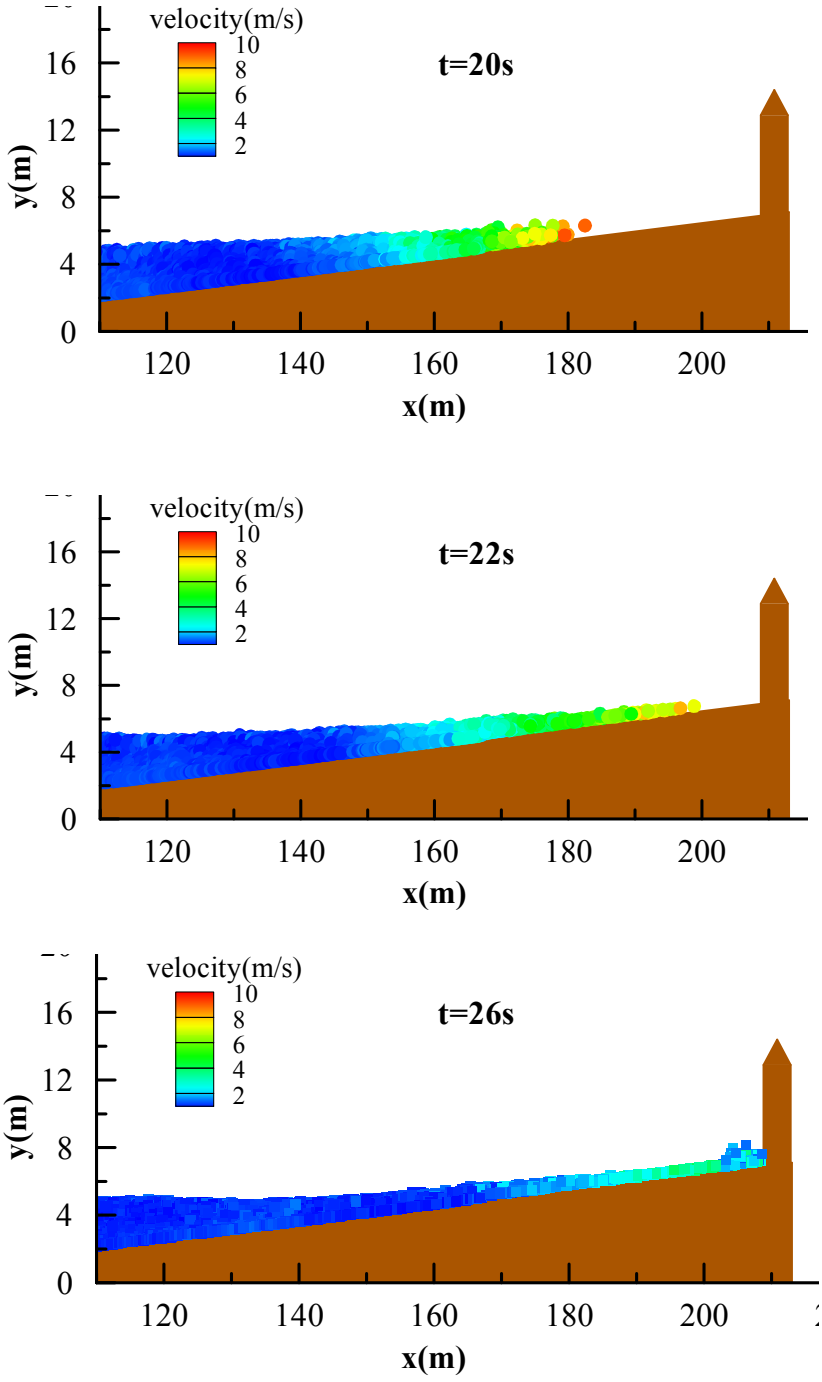

Figure 4.13. Wave run-up and interaction with the house located at 3*R*/4 above the initial shoreline

Figure 4.13 shows the snapshots of water particles together with the velocity fields during the wave run-up and interaction with the house located at 3*R*/4 above the initial shoreline. The free surface is captured by identifying the free surface particles, which have a smaller particle density as compared with the inner fluid particle density.

As the solitary wave approaches to the initial shoreline, the water depth decreases gradually. Consequently, the wave front becomes steeper until it reaches the maximum height around time t = 14s, which is the wave breaking point. It is hard for the particles on the edge of the wave front to remain on the water surface due to their high velocities, resulting in large wave deformation and subsequent breaking (t = 16s). Then the broken wave continues to deform with high speed particle velocity towards the initial shoreline (t = 18s). After passing the initial shoreline, it runs up along the slope and then hits the beach house.

Figure 4.14 shows the snapshots of water particles together with the velocity field of wave run-up and interaction with the house which is located at *R*/2 above the initial shoreline. The wave shoaling, breaking and run-up are nearly the same as the previous case with the house being located at 3*R*/4 above the initial shoreline, but in this case the breaking wave hits the house at an earlier time.

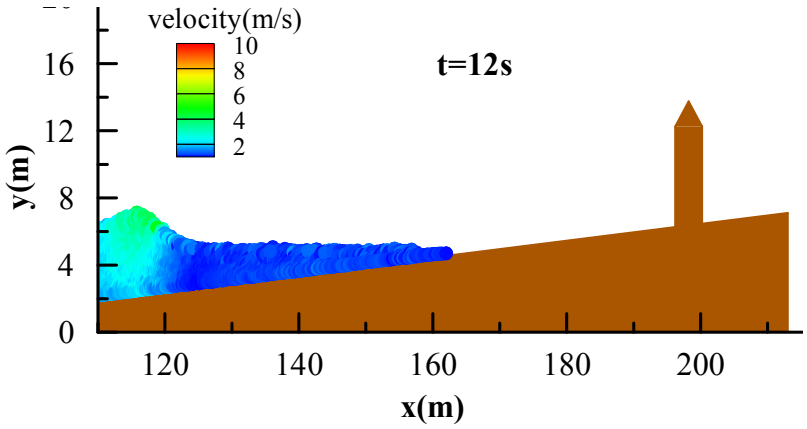

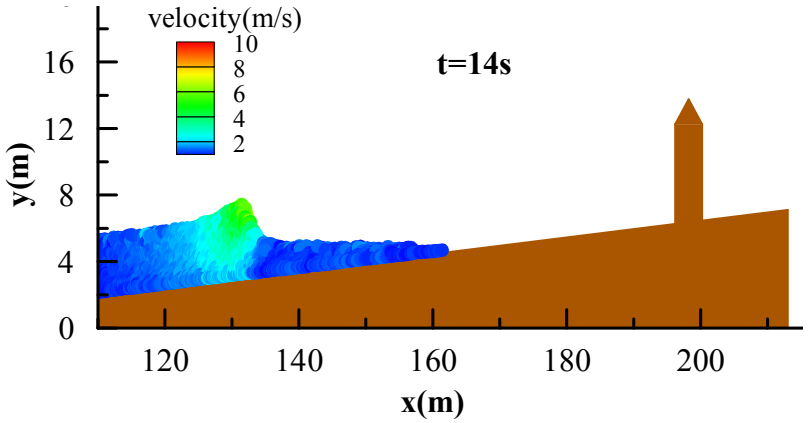
velocity(m/s)
10
8
6
4
2
t=14s
y(m)
0
4
8
12
16
120
140
160
180
200
x(m)

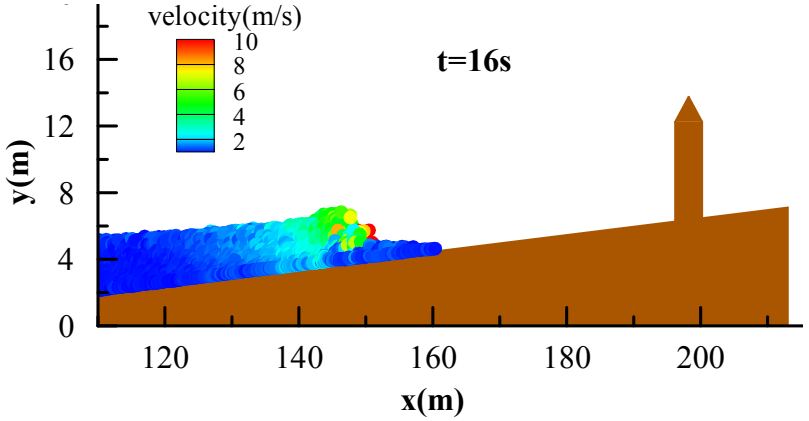
velocity(m/s)
10
8
6
4
2
t=16s
y(m)
0
4
8
12
16
120
140
160
180
200
x(m)

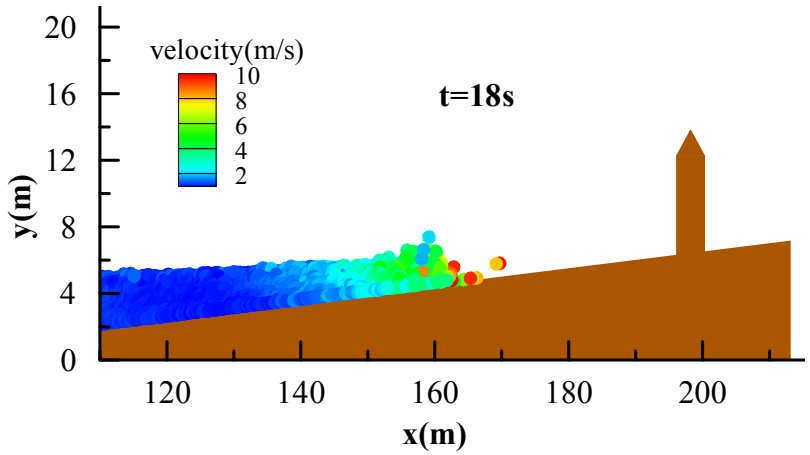
velocity(m/s)
10
8
6
4
2
t=18s
y(m)
0
4
8
12
16
20
120
140
160
180
200
x(m)

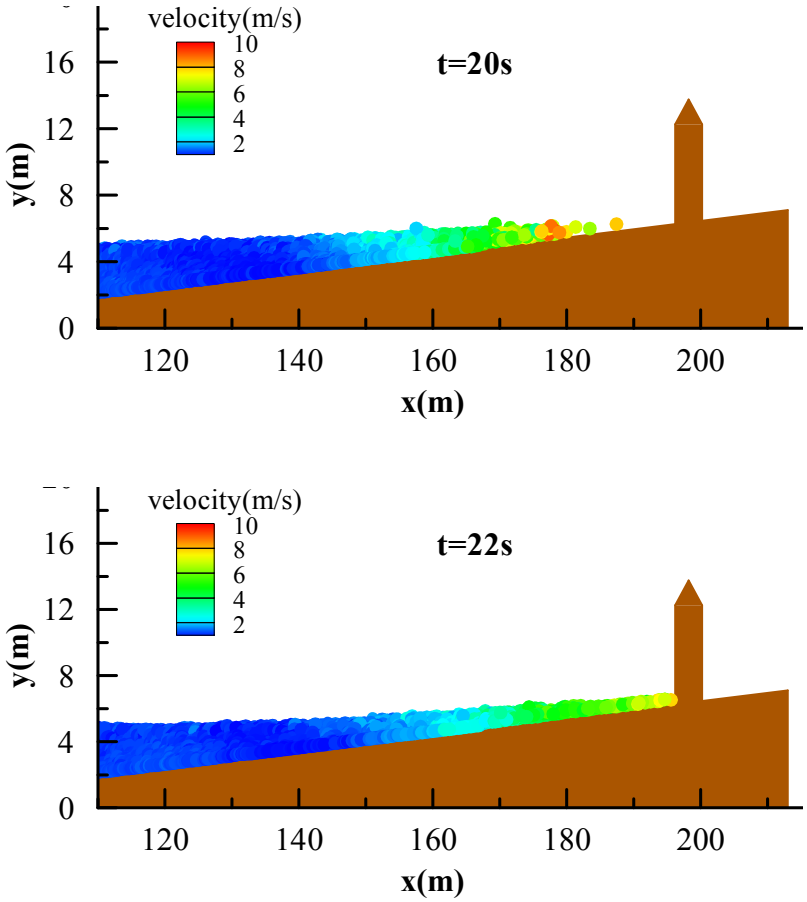

Figure 4.14. Wave run-up and interaction with the house located at $R/2$ above still water surface

Figure 4.15 and Figure 4.16 show the snapshots of water particles together with the velocity field of wave run-up and interaction with the house which is located at $R/4$ above the initial shoreline. The wave shoaling, breaking and run-up are nearly the same as the previous case with the house being located at $3R/4$ above the initial shoreline. As the house gets closer to the initial shoreline, the breaking wave hits the house at an earlier time and clear reflection of the breaking solitary wave occurs in front of the house.

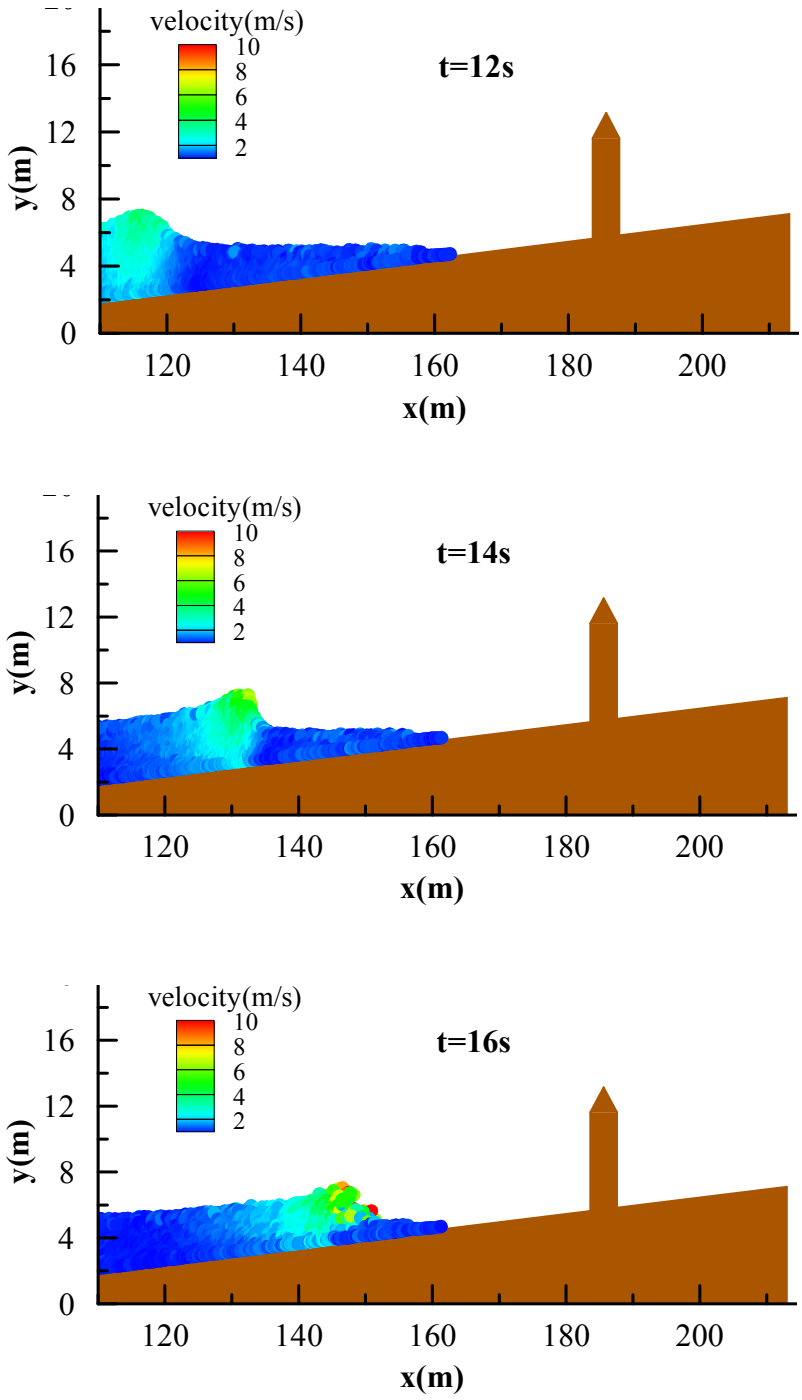

Figure 4.15. Wave run-up and interaction with the house located at *R*/4 above still water surface

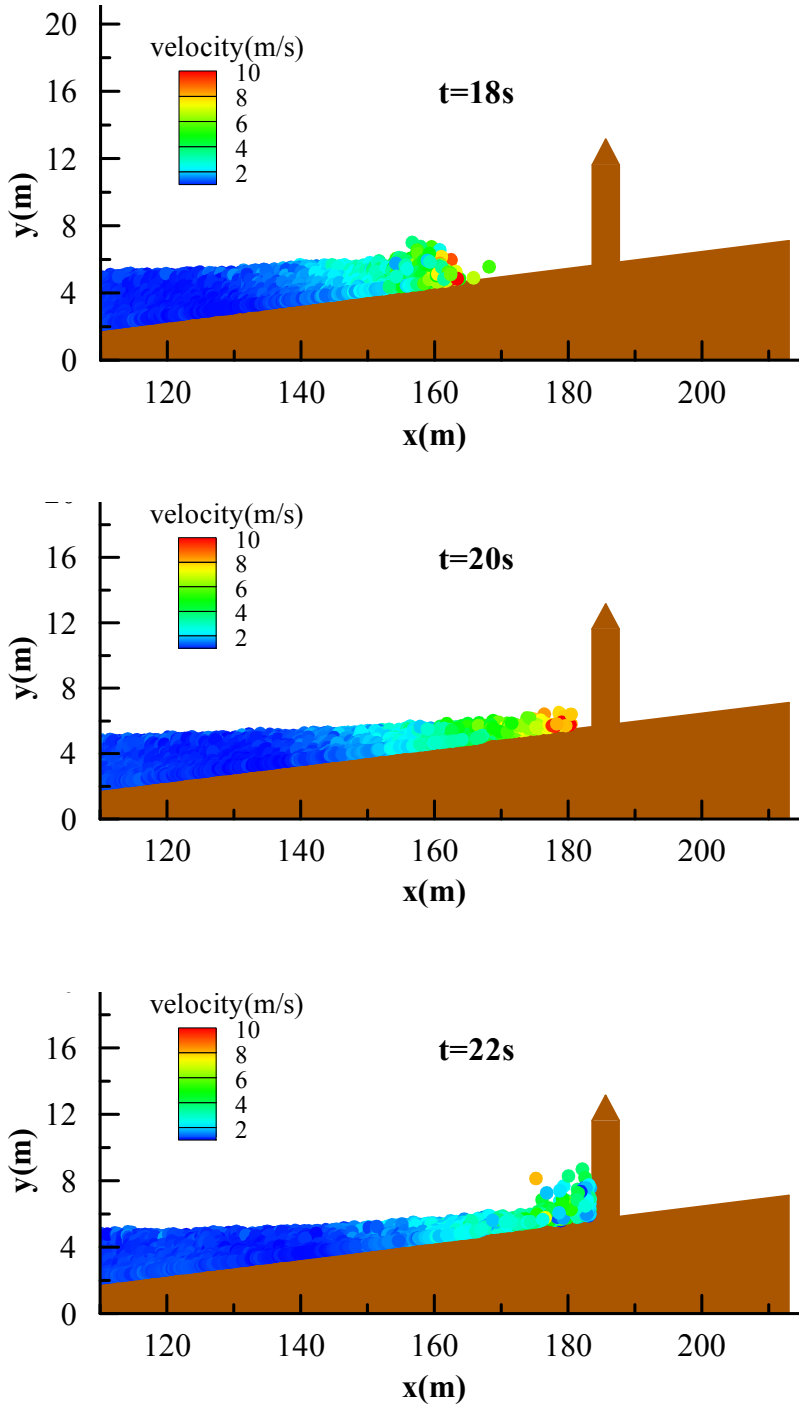

Figure 4.16. Wave run-up and interaction with the house located at *R*/4 above still water surface

Figure 4.17 and Figure 4.18 show the snapshots of water particles together with the velocity fields during the wave run-up and interaction with the house when

it is located at the initial shoreline (0*R*). The main difference between this case and the previous one is that more water piles up in front of the house, which causes the strong reflections of the wave.

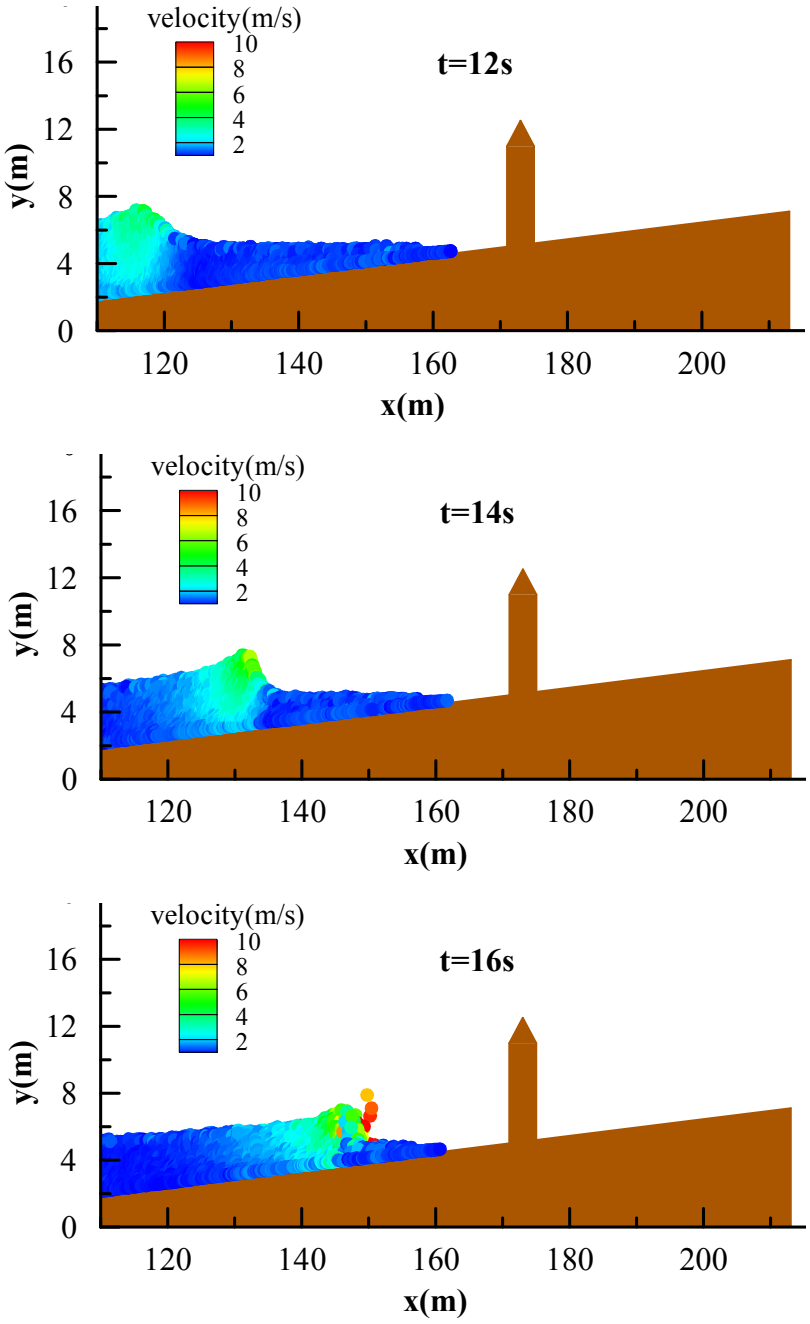

Figure 4.17. Wave run-up and interaction with the house located at the initial shoreline

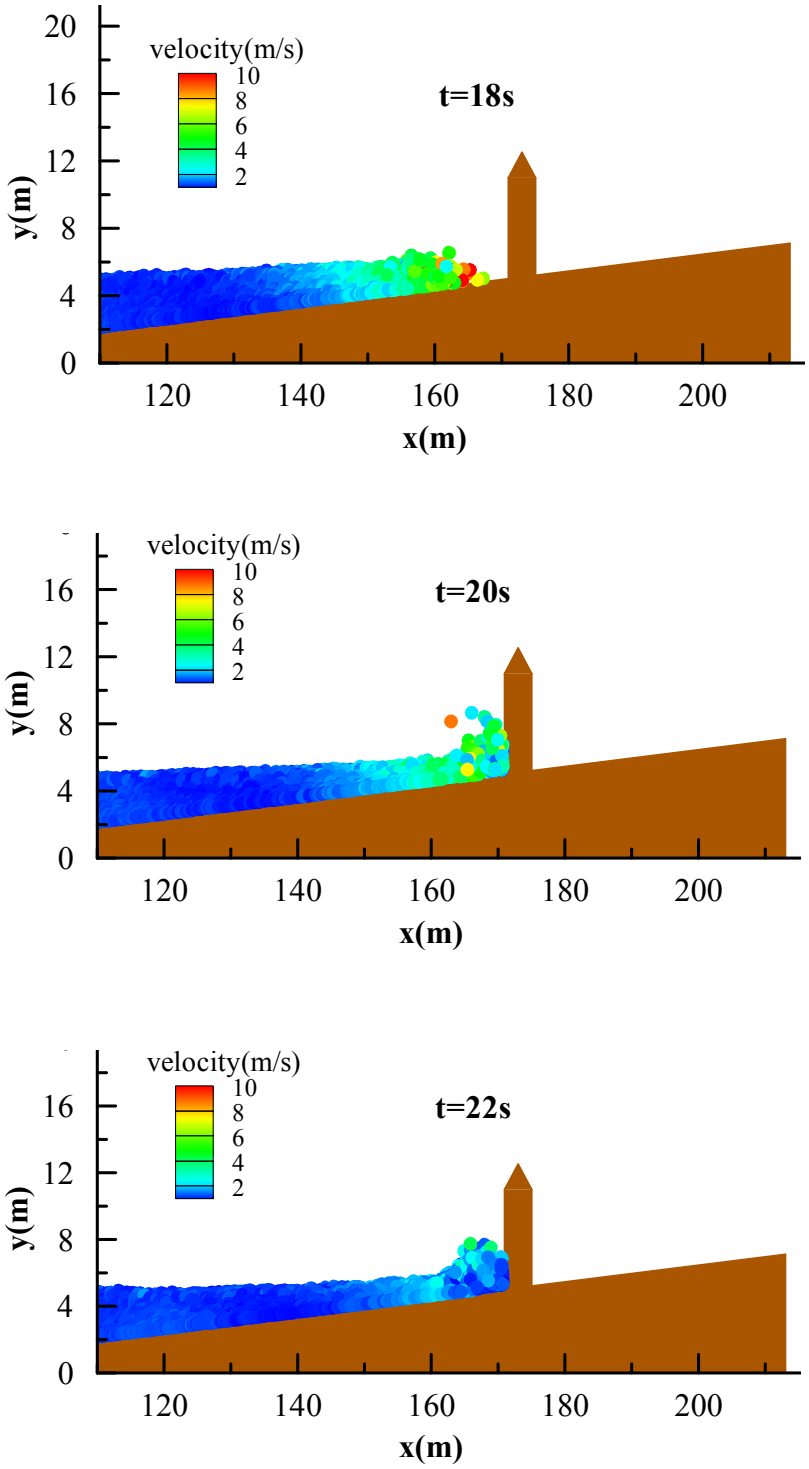

Figure 4.18. Wave run-up and interaction with the house located at the initial shoreline

Figure 4.19 shows the snapshots of water particles together with the velocity field of wave run-up and interaction with the simplified house when it is located at *R*/4 below the initial shoreline. In this case, the subsequent breaking wave run-up process does not happen. The wave hits the house just a short time after it breaks. Only a few water particles spray and the bulk of water just piles up in front of the house and wave reflection is therefore stronger.

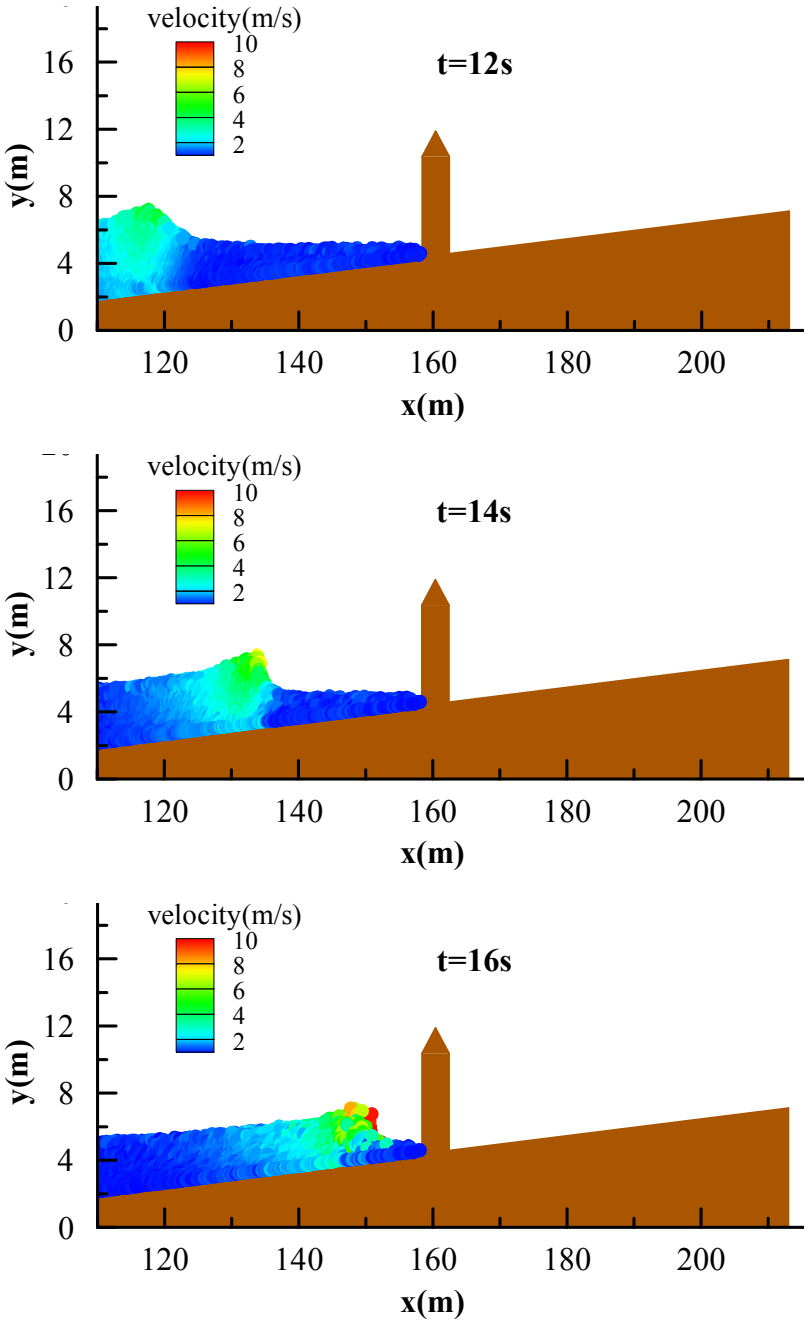

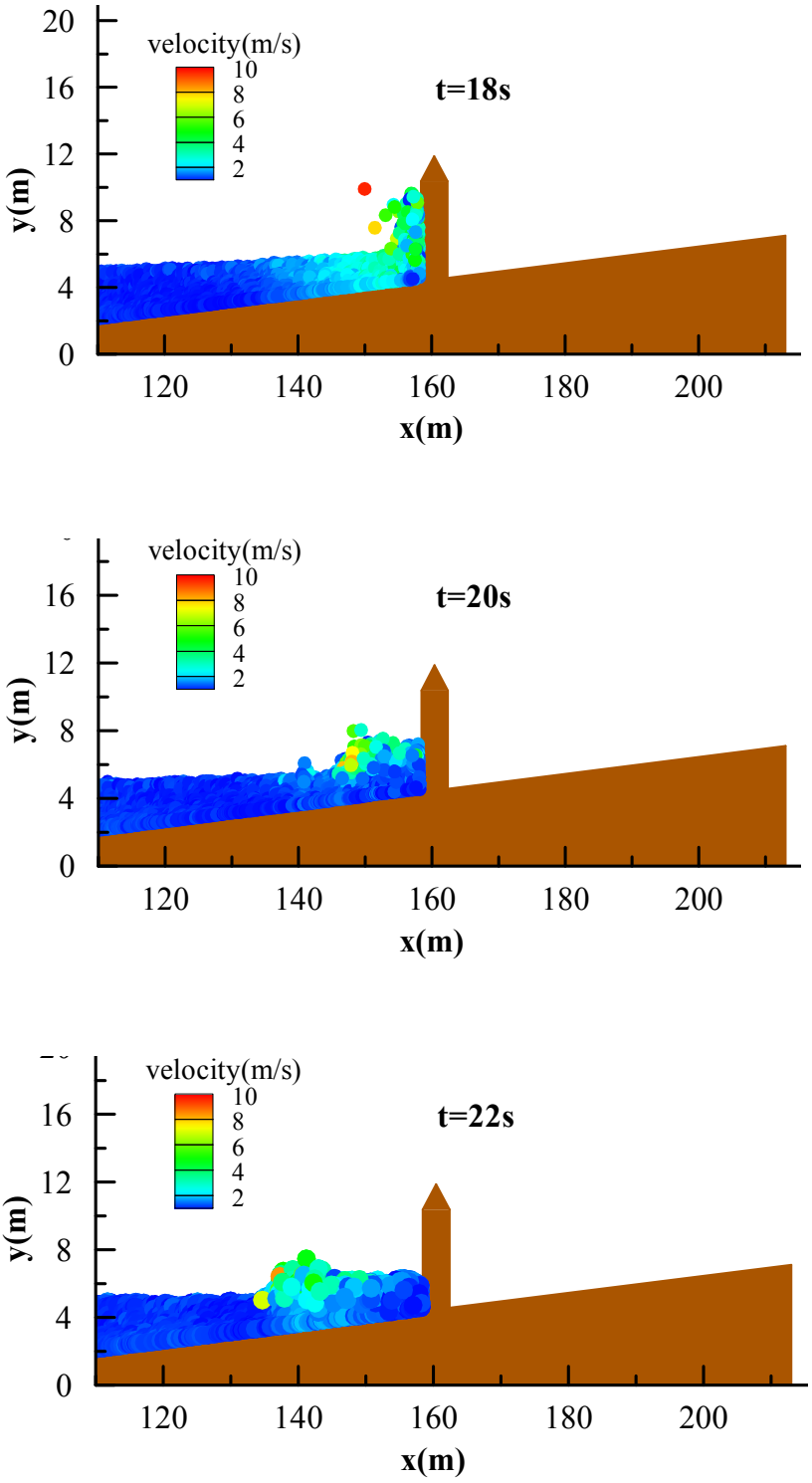

Figure 4.19. Wave run-up and interaction with the house located at *R* /4 below still water surface

Figure 4.20 to Figure 4.24 show the time histories of the normalized wave forces computed by the ISPH with mixed source term in PPE and the simulation results of Xiao and Huang (2008) by using a RANS model with VOF surface tracking. The wave force of ISPH on the house was obtained by computing the integral of the particles pressures on the weather side of the house. The results are presented for the beachfront house locations being at five different fractions of the wave run-up height (-*R*/4, 0*R*, *R*/4, *R*/2, 3*R*/4).

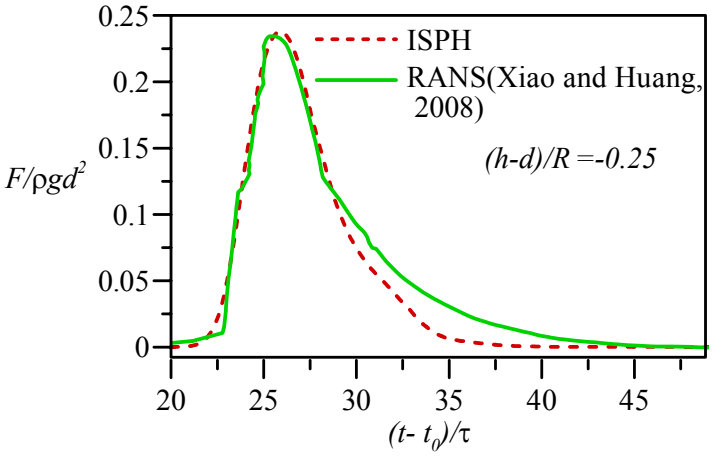

Figure 4.20. Time histories of normalized wave force computed by ISPH and RANS (Xiao and Huang, 2008): $(h-d)/R = -0.25$

In these figures, the wave force F is normalized by $\rho g d^2$ and time t by $(t-t_0)/\tau$, where ρ is the density of water, d is the still water depth and g is the gravitational acceleration. t_0 the time origin defined at when the wave crest is 150m away from the initial shoreline and τ is given by $\tau = (d/g)^{1/2}$. The green lines in the figure represent the calculated values by Xiao and Huang (2008), while the red dashed lines represent the results from the ISPH model with mixed source term. h is the elevation of the house location. In all cases it is shown that the wave impact forces increased rapidly when the waves approached the house and the peak forces occurred when the wave fronts hit the house. Since the reflected water particles

returned back with a lower speed, the force curves went down slowly until they reached the initial zero levels.

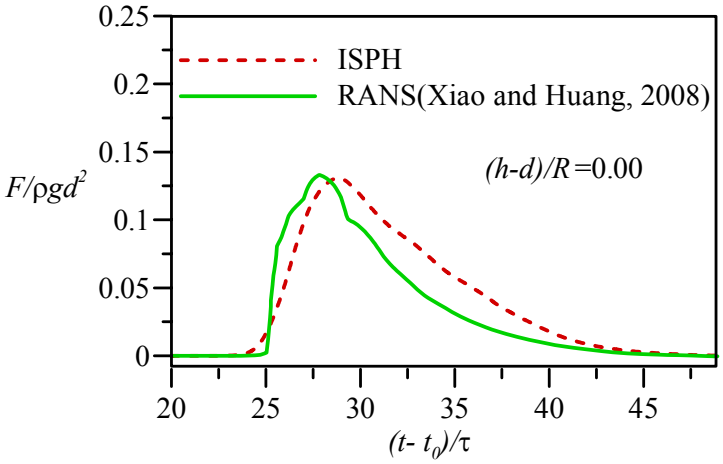

Figure 4.21. Time histories of normalized wave force computed by ISPH and RANS (Xiao and Huang, 2008): $(h-d)/R=0.00$

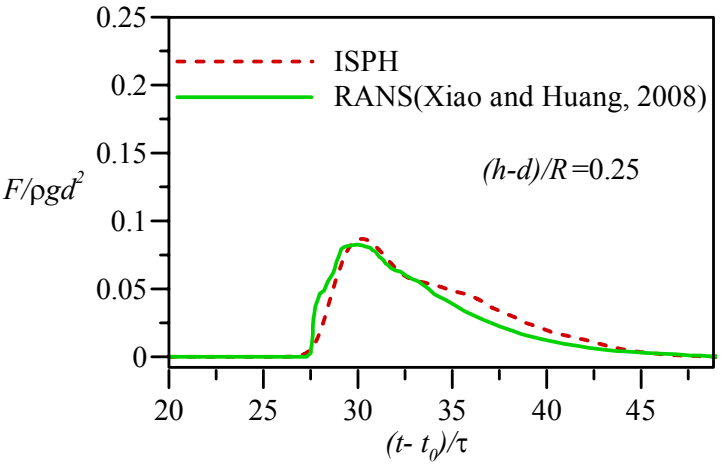

Figure 4.22. Time histories of normalized wave force computed by ISPH and RANS (Xiao and Huang, 2008): $(h-d)/R=0.25$

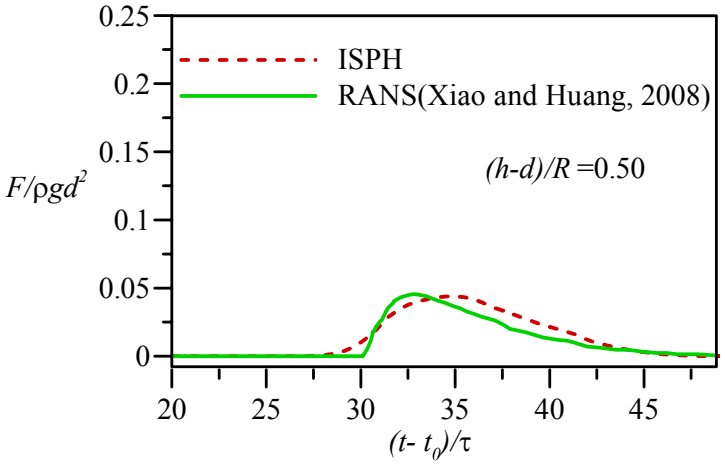

Figure 4.23. Time histories of normalized wave force computed by ISPH and RANS (Xiao and Huang, 2008): $(h-d)/R=0.50$

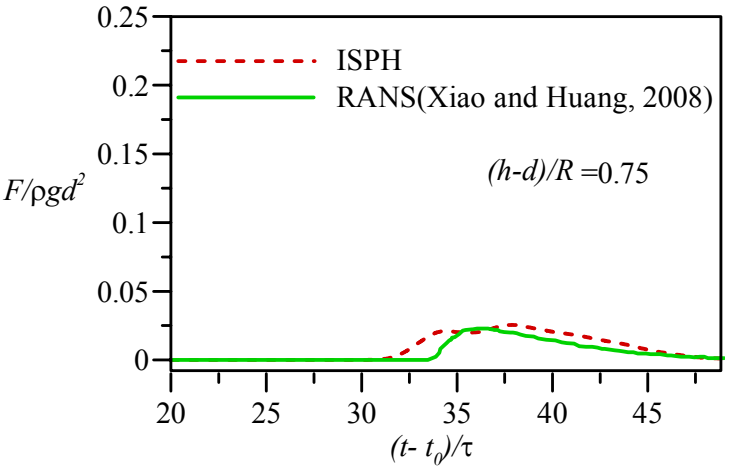

Figure 4.24. Time histories of normalized wave force computed by ISPH and RANS (Xiao and Huang, 2008): $(h-d)/R=0.75$

Overall the ISPH results agree well with the RANS results of Xiao and Huang (2008). The maximum normalized wave force is 0.238 for ISPH and 0.236 for Xiao and Huang (2008) when the house is located at R/4 below the still water surface, so the error is just 0.8%. The errors of the other four cases with

$(h-d)/R = 0.75$, 0.50, 0.25 and 0.00 are 12.3%, 3.5%, 2.8% and 2.3%, respectively. The errors become smaller as the house location is closer to the initial shoreline, when the wave particle configuration is still in order. It is noted that the curve span of the ISPH results is broader than the RANS's when the house is located at 3*R*/4 above the initial shoreline ($(h-d)/R = 0.75$), while it is nearly the same when the house is located at the initial shoreline ($(h-d)/R = 0.00$). However, the force curves of Xiao and Huang (2008) rise up and go down more quickly at the early stage of the wave reflection. The peak force computed by the ISPH occurs later than that computed by Xiao and Huang (2008) for the house location at *R*/2 above the initial shoreline ($(h-d)/R =$ 0.50). The maximum difference in the two model computations is found for the house location at 3*R*/4 above the initial shoreline ($(h-d)/R = 0.75$), when the wave has fully broken and thus the oscillations of water particles lead to more inaccuracies.

4.4 Sensitivity of new model on Particle Spacing

In order to investigate the convergence of the numerical model and also find out the dependence of the weighting coefficient α in PPE source term on the particle spacing D_0, additional numerical runs are carried out by alternating the particle spacing for the previous two wave impact cases and the results are compared with the original runs, the purpose of which is to check whether the weighting coefficient α would remain the same or not if the spatial resolution changes.

4.4.1 Dam break flow

First, for the dam break flow, three additional computations were done by using the refined particle spacing D_0 = 0.003m, 0.002m and 0.001m, respectively (further reduction of the particle spacing caused a significant increase in the CPU time and thus was not attempted), and the time histories of the computed pressures at the measuring point are compared with the original ones (in which a particle spacing of

D_0 = 0.0004m was used) in Figure 4.25. In ISPH computations the weighting coefficient α has been kept the same for all the runs. Figure 4.25 shows that as the particle spacing decreases, i.e. the spatial resolution increases, more smoothed pressure curves are obtained and the differences between the adjacent results become smaller, indicating the convergence of the model. Besides, it also clearly shows that based on the same weighting coefficient α = 5% for the PPE source term, the pressure results are insensitive to the selected particle size.

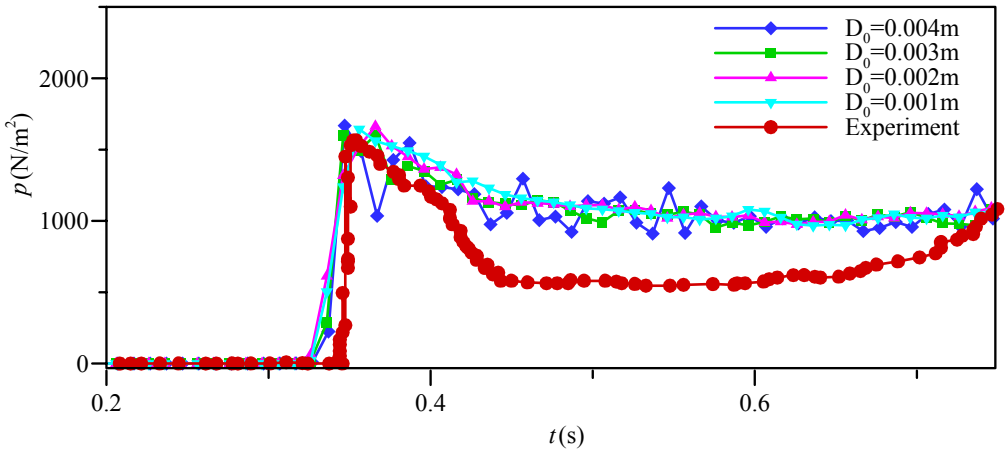

Figure 4.25. Time histories of computed pressures of original and two refined ISPH runs for dam break flow

4.4.2 Solitary wave impact

To provide further evidence on the above analysis, similar sensitivity tests were also made for the solitary wave impact on the different house locations. Here I only present the wave force comparisons when the house location is $R/4$ above the initial shoreline, because similar phenomena can also be observed for the other three locations. In this case, due to the fact that the decrease of particle spacing D_0 would lead to a large number of particles at the expense of CPU power, only one refined run was made by using a particle spacing 0.1m, as compared with the original run in which a particle spacing of 0.2m was used.

Figure 4.26 shows that the normalized wave forces computed by two different spatial resolutions in the ISPH lead to very similar results based on one identical PPE source term weighting parameter α = 55%. This has provided another strong indication that the weighting coefficient in the proposed mixed PPE source term is largely independent of the particle size, because a strict incompressible formulation was used. On the other hand, the weighting coefficient in Asai et al. (2012) also depended on the particle spacing, which was due to that their formulation of the mixed PPE source term involved a relaxation term.

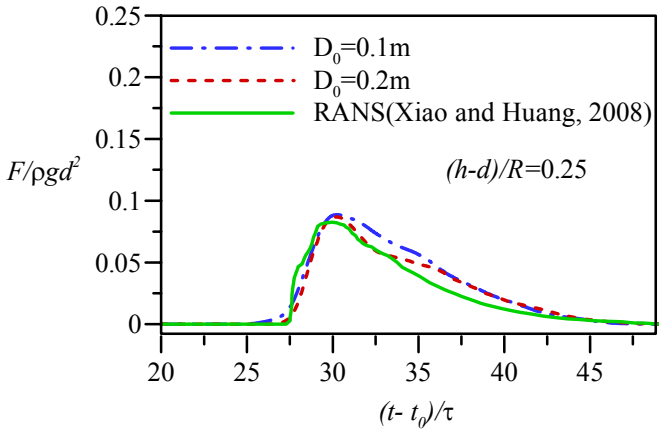

Figure 4.26. Time histories of normalized wave forces of original and refined ISPH runs for solitary wave impact

From Figure 4.8 and Figure 4.25 in the dam break flow study, it was found that although the peak impact pressures were well computed, the pressure evolutions were poorly predicted after the first peaks. In spite that the particle resolutions have been refined several times, no significant improvement in prediction is achieved. The convergence analysis in Figure 4.25 shows that the refinement of spatial resolutions could effectively eliminate the pressure oscillations but does little to affect the pressure predictions.

4.5 Effects of turbulence in ISPH

The pressure over-predictions after the first peak which was also observed in the ISPH computational results of Khayyer et al. (2009), many reasons was discussed in previous text. Besides those reasons, the most important reason might be that the turbulence wasn't considered in the previous computation. But the flow turbulence is strong during the severe wave breaking after the first wave impact.

To evaluate the turbulence effect, another computation was made by incorporating an eddy viscosity based Sub-Particle-Scale (SPS) turbulence model. The details of this model can be found in Gotoh et al. (2004). By using a Smagorinsky constant of approximately 0.25, the recomputed time histories of pressure are shown in Figure 4.27, also compared with all of the original data in Figure 4.8. It is very interesting to notice that the turbulence modelling results significantly improved the non-turbulent modelling and reduced the prediction errors after both the first and second pressure peaks by about 50%. This is a strong indication that the turbulence model in SPH plays an indispensable role in predicting

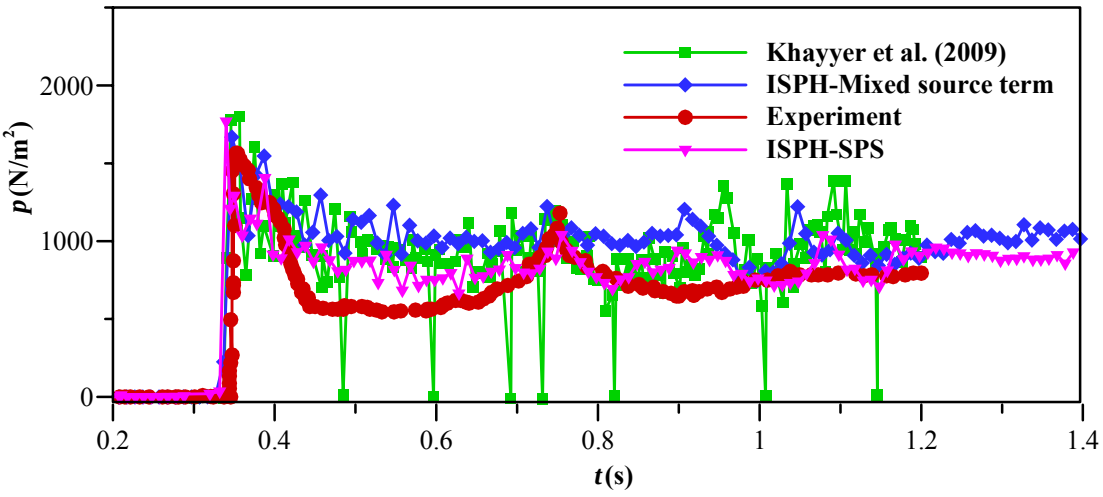

Figure 4.27. Time histories of pressures computed by non-turbulence and turbulence SPS models

violent flows, especially when the spatial resolution is not fine enough to capture the small scale flow details.

As for violence wave, such as wave breaking, turbulence can't be neglected in the numerical simulation. Case I Dam break impact have demonstrated that the using turbulence modelling in ISPH can significantly improve the inviscid modelling capacity and thus reduce the prediction errors in the time history of pressures in the dam break flow. So the inclusion of turbulence model could be of great importance for wave pressure prediction when free surface of the flow is highly broken and large deformation, the turbulence generation is influential. Further investigations are needed for different flow conditions.

4.6 Determination of PPE source term parameter

In practical engineering applications of the model the PPE source term parameter α in equation (4.1) needs to be estimated as in these situations, the α value cannot be easily calibrated by using the available data. A simple analytical reasoning would imply that the coefficient α should physically represent the flow energy dissipation mechanisms, which are related to the typical height and length scales of the flow under consideration. In the dam break, such flow scale parameters could be the dam height and horizontal section length from the dam site, while in the wave run up, it could be the wave height and the horizontal section length of the slope over which the wave deformation occurs. Thus the ratio of the height to length scales H/L is expected to represent the flow energy dissipation scale, similar to the surf similarity parameter widely used in the coastal hydrodynamics.

In the previous dam break and wave run up studies, the H/L values were 0.24 and 0.02, and the corresponding α values were 0.05 and 0.55, respectively. In order to find a general relationship between these two parameters, additional three test cases are considered in this section. They are related to the problems of dam break flow (Lee et al., 2011), in which the ratio of H/L is 0.67; breaking solitary wave impact (Thao et al., 2008), in which H/L is 0.06; and Tsunami bore forces

(Robertson et al., 2011), in which H/L is 0.037 and 0.0085, respectively. In the ISPH computations, the mixed source term coefficient α values were obtained by matching the numerical wave peak pressures with the documented data. Meanwhile, the computations have suggested that the pressure time histories were also well predicted by these calibrated α.

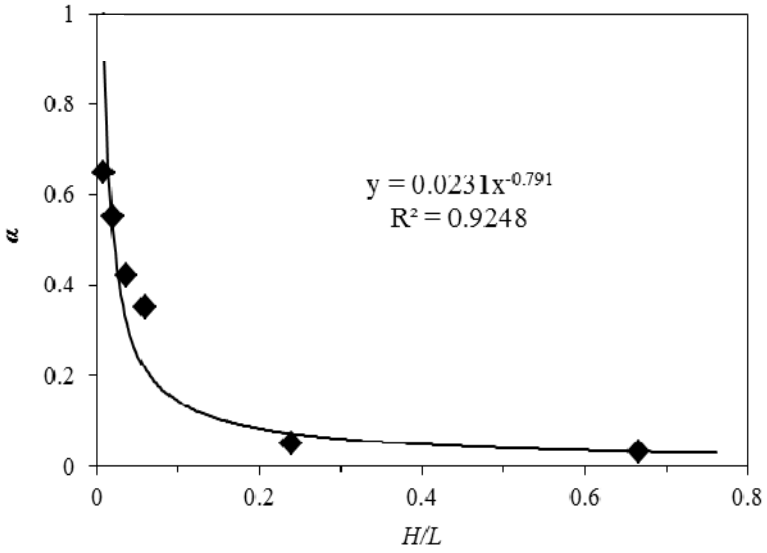

Figure 4.28. Relationships between flow height to length scale ratio (H/L) and weighting coefficient (α) in PPE mixed source term

Based on the original two and additional three runs, Figure 4.28 shows the relationship between H/L and α. The figure demonstrated a very satisfactory correlation between the two parameters which can be fitted by a hyperbolic line also shown in the figure with a correlation coefficient 0.9248. This figure clearly indicated that as H/L increases, in which the flow becomes more violent, the α value decreases accordingly, so that the density invariant part plays a smaller role in equation (4.1) and the divergence free part is more important, and vice versa. This finding gives quantitative support to the previous discussions on the selection of α values in the ISPH computations. Besides, the figure also indicates that the change of the curve is more in the middle range of H/L while it tends to stabilize at the very large and small H/L values. Figure 4.28 provides a useful reference to approximately predetermine the value of the mixed source term parameter in a wave

impact problem where no documented data is available. Since the smaller coefficient α points are obtained all from the solitary wave cases, this relation may not applicable when H/L has a large value, such as 0.7, in a solitary wave case due to the uncertainly of the flow field. The solitary wave may reflect from dike or break severely.

4.7 Summary

A new pressure Poisson equation source term with the weighted combinations of the density invariant and velocity divergence terms is proposed to improve the stability and accuracy of the ISPH method for wave impact simulations. The model is evaluated by applying it to two typical wave impact cases: one is the dam breaking wave impact on a vertical wall and the other one is the solitary wave running up and impact on a coastal house. The computational results have indicated that the combined source term treatment can well predict the wave impact pressure and force. Sensitivity studies have shown that the weighting coefficient in the mixed source term is quite independent of the particle spacing in a converged solution and thus can be practically treated as a constant.

Through model validations against the documented data, we could find that the proposed ISPH model with improved PPE source term could well predict the dam break wave impact with much less pressure noises and also satisfactorily reproduce the solitary wave impact forces computed by the established RANS model. Although the total CPU cost of the mixed model is comparable to the model in which either the pure density invariant or velocity divergence free PPE source term is used, the computational accuracy has considerably improved based on the minimum modifications of the numerical algorithm. The tests also demonstrated that the model should be applicable to different wave impact situations with consistent behaviour of the weighting coefficient in the PPE source term for each application, thus it would be expected to provide a potential promising tool to predict real wave impact problems with sufficient accuracy. This would be of particularly interest to

the breakwater design, in which accurate integrations of the wave force and moment are required. However, depending on different flow applications, the weighting coefficient could vary considerably. For the more violent wave impact case, the divergence part is found to play a more prominent role in ensuring accurate force simulations, while in the less violent wave impact problems, the density part seems to be more important. For the two investigated wave impact cases, the weighting coefficient ranges from α = 5% in the dam break impact to 50% in the solitary wave impact.

Also, by performing additional three numerical tests and carrying out relevant analysis, it was found that there existed a close correlation between the ratio of flow height to length scales H/L and the weighting coefficient α in the mixed pressure source term. The relationship curve changes more notably in the middle range of H/L but varies very little near its lower and upper bounds. This result could be used to pre-determine the PPE source term coefficient and thus predict wave impacts in a practical engineering application where no measurements are available.

Chapter 5

PPE source term errors in the incompressible SPH Models

5.1 Introduction

A number of studies have been carried out recently on the pros and cons of WCSPH and ISPH for the free surface flow simulations. Hughes and Graham (2010) studied two standard dam-break problems and one regular water wave impact against a vertical wall and they found that the WCSPH performs at least as well as ISPH, and in some respects clearly performs better. Shadloo et al. (2012) studied the bluff body flow problems such as flow over an air foil and a square obstacle and their predictions of a variety of flow parameters indicated that the WCSPH method with the suggested implementations produced numerical results as accurate and reliable as those of the ISPH. Chen et al. (2013) investigated three benchmark hydrodynamic problems including a liquid sloshing and they concluded that their improved WCSPH is more attractive than the ISPH in modelling free surface incompressible flows as it is more accurate and stable with comparable or even less computational efforts. It should be noted that these WCSPHs have included some additional numerical treatments to improve the model performances, such as the MLS density filter or XSPH schemes, while there were no corresponding treatments in the ISPHs used so the comparisons of the two techniques reported may not have been done on the equal basis. To investigate this finding, in this chapter I consider a benchmark -- dam break problem for comparing with available WCSPH results.

On the other hand, Khayyer and Gotoh (2012) pointed out that the treatment of PPE Laplacian and source terms could heavily influence the simulation accuracy

of particle-based models. Motivated by these studies, in the present work I aim to make a quantitative investigation of the numerical errors of PPE source terms that are commonly used by the two different ISPH projection schemes, i.e. density-invariant and divergence-free, and evaluate their influences on the fluid impact predictions. As far as the present knowledge is concerned, there are several documented works on the study of density accumulation errors in the ISPH projection scheme based on the velocity divergence-free approach (Cummins and Rudman, 1999; Szewc et al., 2012), but there is almost no detailed study reported for the divergence errors in a density-invariant ISPH approach. The pressure noises and particle oscillations in a density-invariant ISPH could be attributed to quite a few complicated mechanisms but the velocity divergence errors could be due to just one important factor that caused the inaccuracy. In this work I will show that with the decrease of the divergence errors the pressure noises and prediction inaccuracies can also be reduced accordingly.

After presenting the hybrid PPE source term in last chapter, I rewrite the mixed source term as below

$$\nabla \cdot (\frac{1}{\rho} \nabla P_{t+1}) = \theta \frac{\rho_0 - \rho_*}{\rho_0 \Delta t^2} + (1-\theta) \frac{\nabla \cdot \mathbf{u}_*}{\Delta t} \tag{5.1}$$

for convenience in this chapter, in which θ is weighting coefficient.

However, quantifying the value of weighting coefficient θ in different applications is not an easy task. By trading off between the pressure fluctuations and fluid volume conservations, Koh et al. (2013) recommended a value of 0.5 for their benchmark sloshing problem. In Asai et al. (2012), they found that the coefficient is not a constant and can be largely depended on the particle spacing. Even the similar combination was applied in Asai et al. (2012), but they used the density at time *t* in the density gradient term while intermediate density is used in my equation. So this difference may lead to different feature of the coefficient from Asai et al. (2012) and mine. In Gui et al. (2014), they used the energy dissipation principle and related the weighting coefficient with the representative height depth ratio of the flow system. An even more advanced weighting coefficient has been developed by Khayyer and

Gotoh (2011) basing on the dynamic instantaneous flow field. It is clear that more works are still required in evaluating the weighting coefficient for this type of mixed source terms. In the present study, I shall focus on evaluating the density and divergence errors of three different projection schemes in equation (3.12), equation (3.16) and equation (5.1), and no further attempt is made to investigate the choice of the weighting coefficient θ.

In this chapter, three different ISPH projection schemes are used to study three benchmark hydrodynamic problems, i.e. two dam break flows and one solitary wave impact, respectively. The aim is to show the computational accuracy of different source term treatments and investigate the fundamental flow behaviours of different impact scenarios. The ISPH computations results are compared with the numerical MPS results of Lee et al. (2011) and experimental data of Robertson et al. (2013). Besides, the computational results are also compared against the numerical data based on the WCSPH. Finally, an extensive numerical analysis is carried out to quantify the density and divergence errors of three different ISPH numerical schemes for the dam break flow.

5.2 Case I: Dam break flow simulations

The numerical simulation is carried out in a 2D tank, as shown in Figure 5.1. The dimension of the numerical tank is 1.6 m by 1.6 m in square. The initial static water column of 0.4 m wide and 0.8 m high is retained by an instantaneously removed vertical wall. The bottom and walls of two sides are solid boundary. Then the water flows along the horizontal bed and hits the right wall generating a high impact pressure. To validate the accuracy of ISPH pressure computations, a reference point (P) located on the right wall at a distance of 0.02 m from the bottom is used to record the ISPH data. The ISPH computed pressures are compared with the improved MPS results by Lee et al. (2011) who used a step by step improvement in the numerical algorithms.

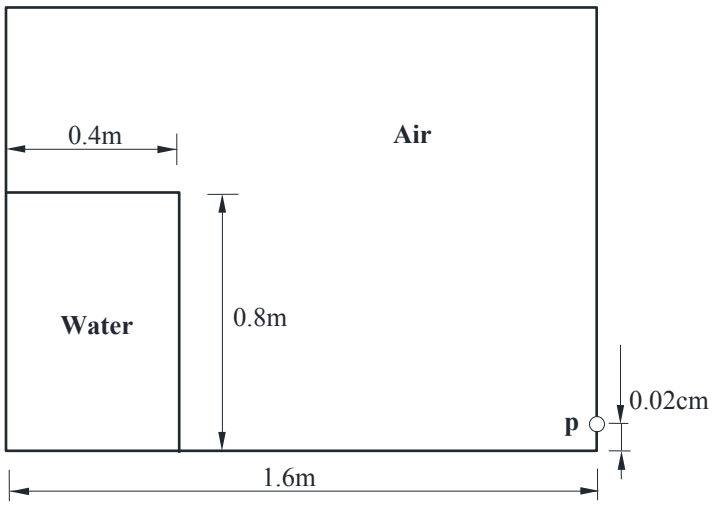

Figure 5.1. Schematic sketch of dam break problem in Lee et al. (2011)

In the ISPH simulations, to be consistent with Lee et al. (2011) the initial particle spacing was selected as D_0 = 0.01 m and thus 3200 fluid particles in total were used. The simulation was carried out up to 3 s. Here it should be noted that in a series of numerical MPS improvements adopted by Lee et al. (2011), a mixed PPE source term that is similar to equation (5.1) was also included and they recommended the weighting coefficient in the equation to be 0.01 ~ 0.05. In the ISPH model, the determination of weighting coefficient θ in equation (5.1)was made on the energy dissipation mechanisms which is related to the height-depth ratio of the flow H/L (Gui et al., 2014). By using this principle, θ was evaluated to be around 0.03, which falls nicely within the value range of 0.01 ~ 0.05 in Lee et al. (2011).

Figure 5.2 shows the comparison of computations made by the ISPH with mixed source term equation (5.1) and the improved MPS proposed by Lee et al. (2011). It demonstrated a quite satisfactory agreement between the two numerical time histories of the wave impact pressures. Both results reported almost identical peak wave arrival time at three different time instants: the first largest one that happened before time t = 0.5 s, which is due to the dam break wave hitting the right side wall and thus generating a quite large pressure impact; the second one that

happened around $t = 1.3$ s, which is due to the falling water plunging down towards the water surface; and the third one that happened about $t = 2.8$ s, which is due to the reflected return dam break wave impacting on the right wall but this time at a much smaller amplitude. The ISPH computations matched the first two peak values well but under-predicted the third one. In the step-by-step improvement of the MPS algorithms in Lee et al. (2011), quite a few numerical treatments include the optimisation of collision coefficient, revision of the source term and gradient model, and improvement of the surface particle search, while in the proposed ISPH only the mixed source term formulation is adopted and it can already give comparable predictions. Here it should be clarified that the computed pressure at measuring point P was obtained by interpolating the pressures of wall particles adjacent to point P on the right wall.

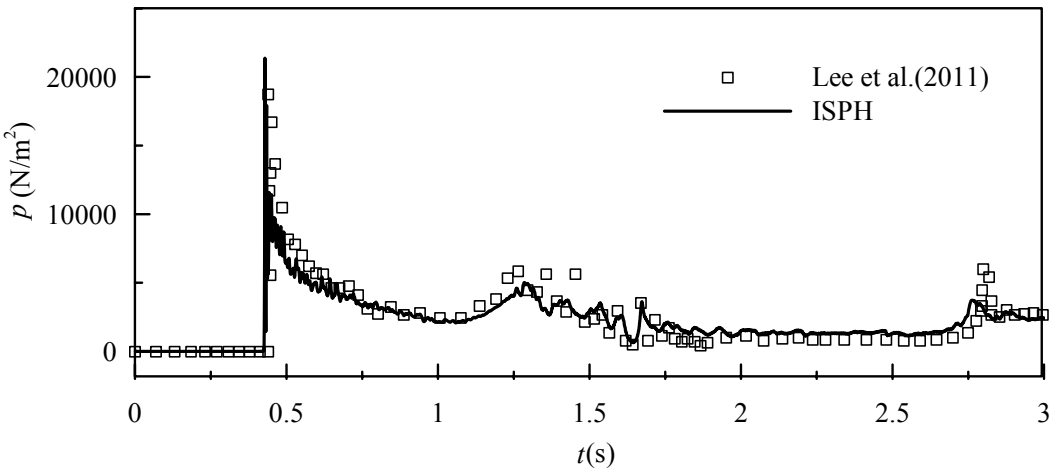

Figure 5.2. Time histories of computed pressures at measuring point P by ISPH and improved MPS of Lee et al. (2011)

To demonstrate the general dam break flow features, the computed ISPH particle snapshots with the velocity contours are shown in Figure 5.3, Figure 5.4 and Figure 5.5 at several typical times. The computations showed the dam break flows impacted on the right wall at time $t = 0.44$ s and ran along against the wall to reach maximum height at $t = 0.6$ s. Then the flows plunged down on the water surface and

created a second splash at $t = 1.34$ s. The velocity contours indicated that larger flow velocities always appear near the flow front and smaller flow velocities are found upstream of the original dam site.

Also, by comparing the particle snapshots computed by Lee et al. (2011) with the original and improved MPS in Figure 5.6, it can be seen that the present ISPH simulations are much better than the original MPS in view of reducing the particle oscillations. However, the ISPH simulated particle snapshots still contain more noises than the improved MPS results, as the latter used several complementary numerical schemes to improve the model performance. It can be concluded that the good agreement in the time histories of impact pressure is an indication that these local particle snapshot noises did not influence the accuracy of predictions on the wave impact pressures underneath the water.

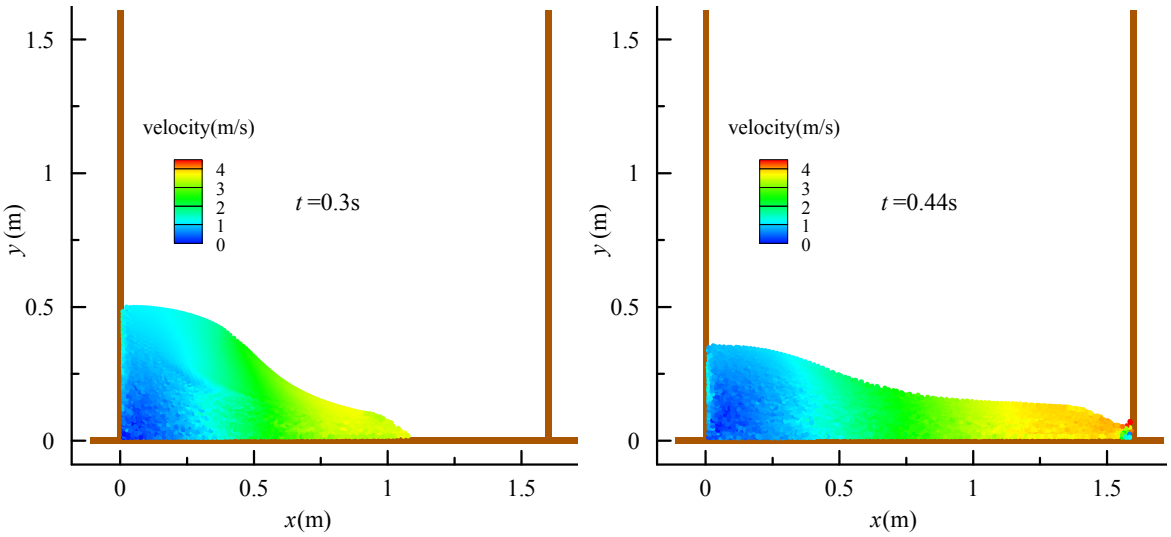

Figure 5.3. Particle snapshots with velocity contours at different times: $t = 0.3$ s and $t = 0.44$ s

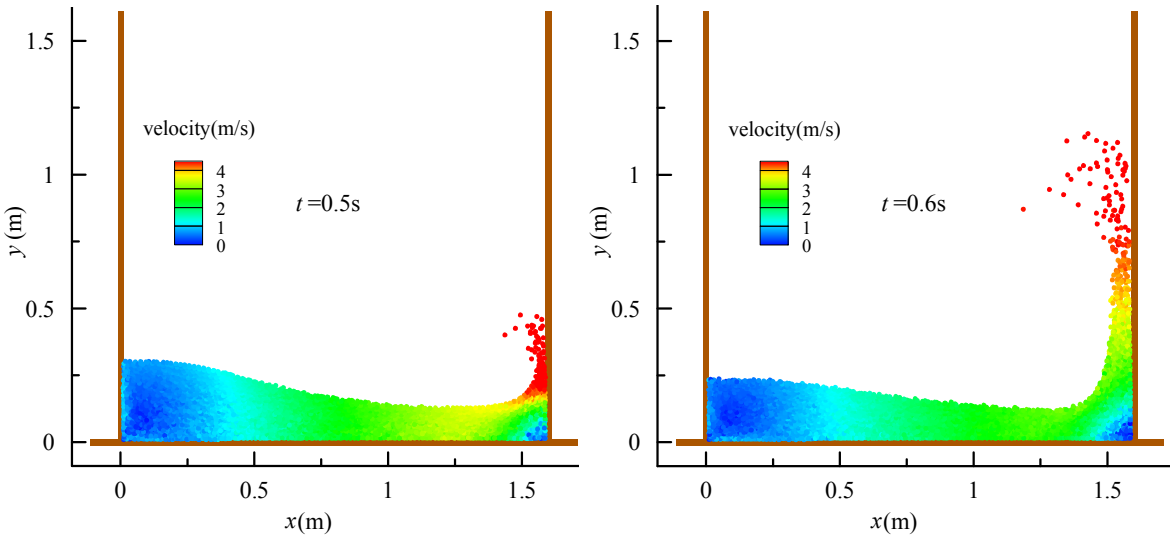

Figure 5.4. Particle snapshots with velocity contours at different times: $t = 0.6$ s and $t = 0.6$ s

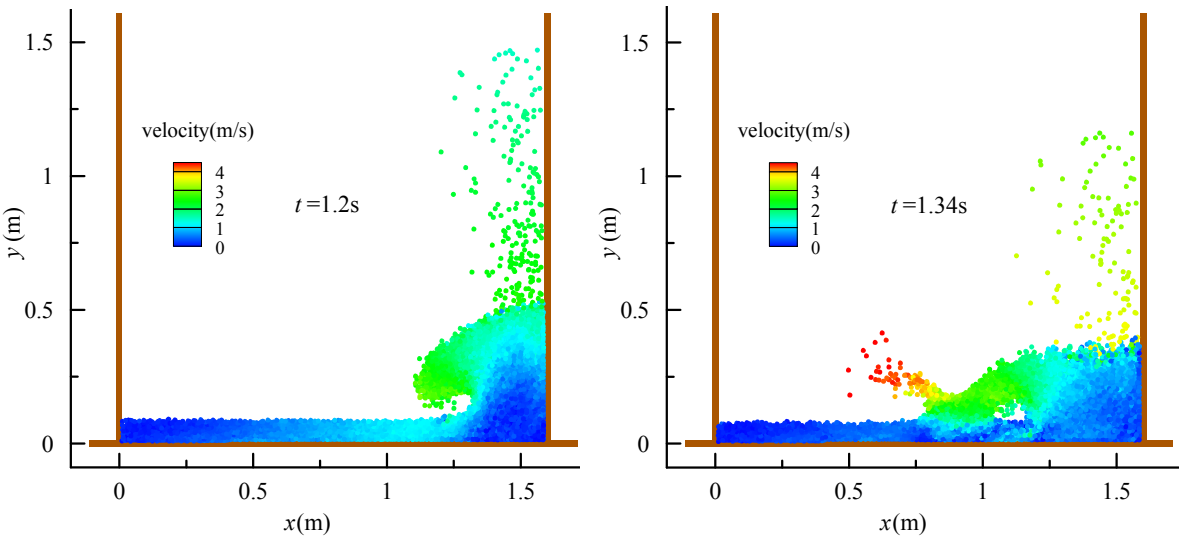

Figure 5.5. Particle snapshots with velocity contours at different times: $t = 1.2$ s and $t = 1.34$ s

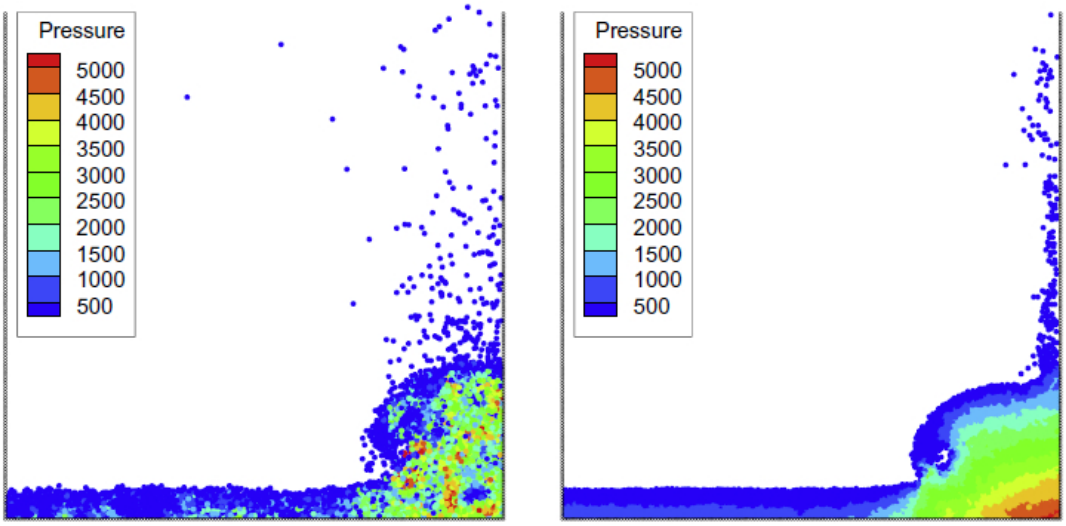

(Oroginal MPS) (Improved MPS)

Figure 5.6. Particle snapshots with pressure contours computed by Lee et al. (2011) with the original and improved MPS

To further demonstrate the differences in prediction results using different ISPH PPE source term formulations, additional two runs were made in which only the density-invariant or the velocity divergence-free scheme as given by equation (3.12) and equation (3.16) was used, and the simulation results of time history of wave impact pressures are compared with the mixed source term results based on equation (5.1) and the improved MPS computations of Lee et al. (2011) in Figure 5.7. It showed that the pure density-invariant ISPH model predicted a consistently higher pressure evolution and also relatively larger pressure fluctuation. Although general pressure time histories follow the correct trend, the pressure amplitude at some time instants can be overestimated by up to several times due to the existence of pressure noise. On the other hand, the pure velocity divergence-free ISPH model predicted a much smaller and smoother pressure process without any pressure fluctuations observed. However, it can barely capture the first pressure peak and fail completely in predicting the second and third pressure peaks, due to the numerical damping caused by the compressions of the fluid volume. The pressure amplitudes

can also be significantly underestimated as a result. In comparison, the mixed source term ISPH model provided the most promising results.

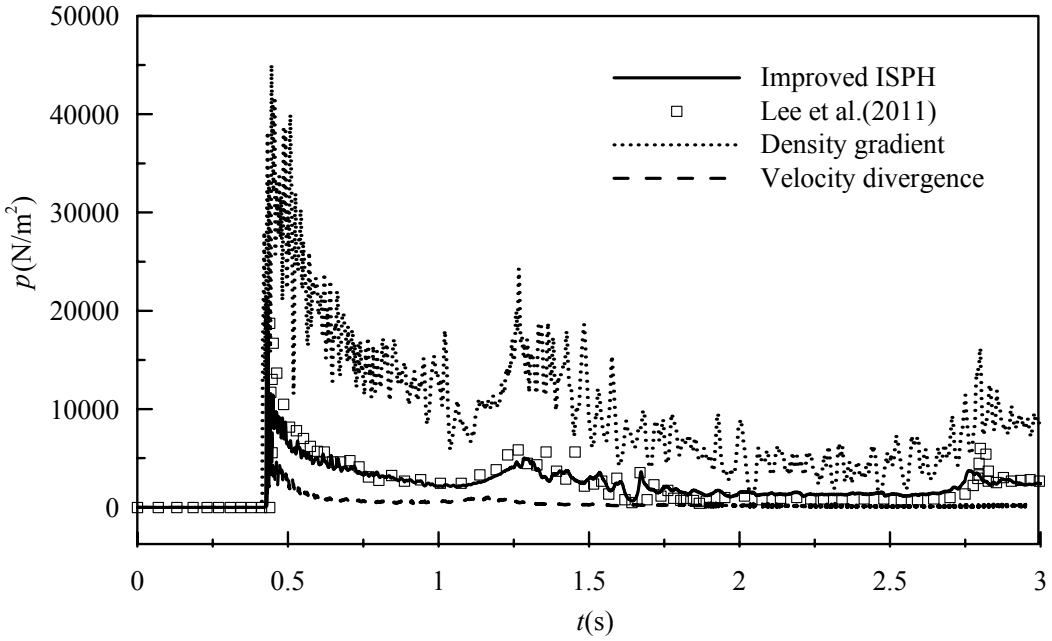

Figure 5.7. Time histories of computed pressures at measuring point P by three different ISPH source terms and improved MPS of Lee et al. (2011)

5.3 Case II: Solitary wave propagation and impact

In this section, the proposed ISPH model is used to reproduce a physical experiment (Robertson et al., 2013) involving a solitary wave propagating and shoaling over a 1:12 beach slope and a flat reef, then turning into a turbulent bore and colliding with a solid wall which is located 83 m away from the offshore wave maker. According to Robertson et al. (2013), the width of the wave flume was 3.7 m, although this parameter is not needed in the present 2D ISPH model. To approximate the actual field tsunami situations, some standing waters were retained in front of the onshore solid wall at the start of the simulation (Robertson et al., 2013). In the ISPH computations, I only reproduced one of the experimental tests carried out by Robertson et al. (2013), i.e. the initial constant water depth in the flume was 2.66 m

and still standing water depth in front of the solid wall was 30 cm. Two different wave heights were studied, which are 53.2 cm and 106.4 cm, respectively. The schematic setup of numerical wave flume is shown in Figure 5.8.

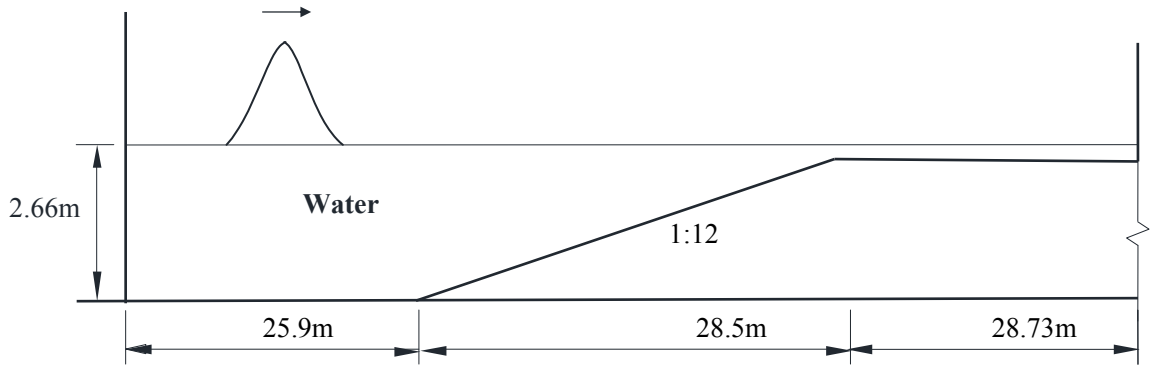

Figure 5.8. Schematic setup of numerical flume for solitary wave propagation and impact (Robertson et al., 2013)

In the ISPH runs, dimensions of the computational domain followed exactly the physical experiment. The particle spacings of D_0 = 0.088 m and 0.1 m were used for the two different wave heights, respectively and thus totally 17000 and 13000 particles were involved in the simulations. The generation of initial solitary wave profile was based on the SPH particle arrangement following the solitary wave analytical solutions, in which a wave profile and velocity field using the particle variables were set at the beginning of the computation. The bottom and walls of right side are solid boundary. Three different ISPH source term formulations, equation (3.11), equation (3.16) and equation (5.1), are used to compute the tsunami wave forces on the solid wall. The computed pressures are compared with the high-resolution pressure gauge measurements by Robertson et al. (2013).

The ISPH computed time histories of wave impact forces on the wall by using the mixed source term formulation equation (5.1)are compared with the experimental data of Robertson et al. (2013) in Figure 5.9 (a) and Figure 5.9 (b), for the initial wave height H = 53.2 cm and 106.4 cm, respectively. It is shown that

each time history is characterized by a rapid increase in the force load to its maximum, which is the result of direct wave collision with the solid wall and water climbing up the wall. The increase is much more obvious in the larger wave height case than the smaller one. As to the maximum force arrival time, it is $t = 17.67$ s for the smaller wave and $t = 14.63$ s for the larger wave. Here it should be noted that the time origins in the present ISPH and in Robertson et al. (2013) are different. The former was defined at the start of solitary wave propagation while the latter was defined when the wave impact started. After the wave force reached its peak value, it started to decrease slowly due to the running down of the flow. A reflective bore has also formed travelling away from the wall and thus the residual force loads dissipated over the time.

Figure 5.9 shows that the ISPH computations agreed quite satisfactorily with the experimental data of Robertson et al. (2013) in that both the force amplitudes and evolution features are well reproduced. However, relatively large errors appeared in case of the larger wave height of $H = 106.4$ cm during the violent wave impact. The experimental data exhibits a monotonous increase in the measured force before the peak being reached and a narrow peak zone, while the ISPH predicted a much wider peak force zone and also the force curve has double peaks during the initial wave impact around time $t = 14.5$ s, although the first small peak is not very distinguishable. The first small force peak happened just a little earlier than the second and much larger peak. Although this phenomenon needs to be further investigated, it may be caused by the nonlinear nature of the wave. The present solitary wave has a height-depth ratio of 0.4, thus it is highly nonlinear.Another reason might be that the particle spacing ($D_0 = 0.1$ m) is not small enough to simulating standing water (depth=0.3m) in front of the solid wall.

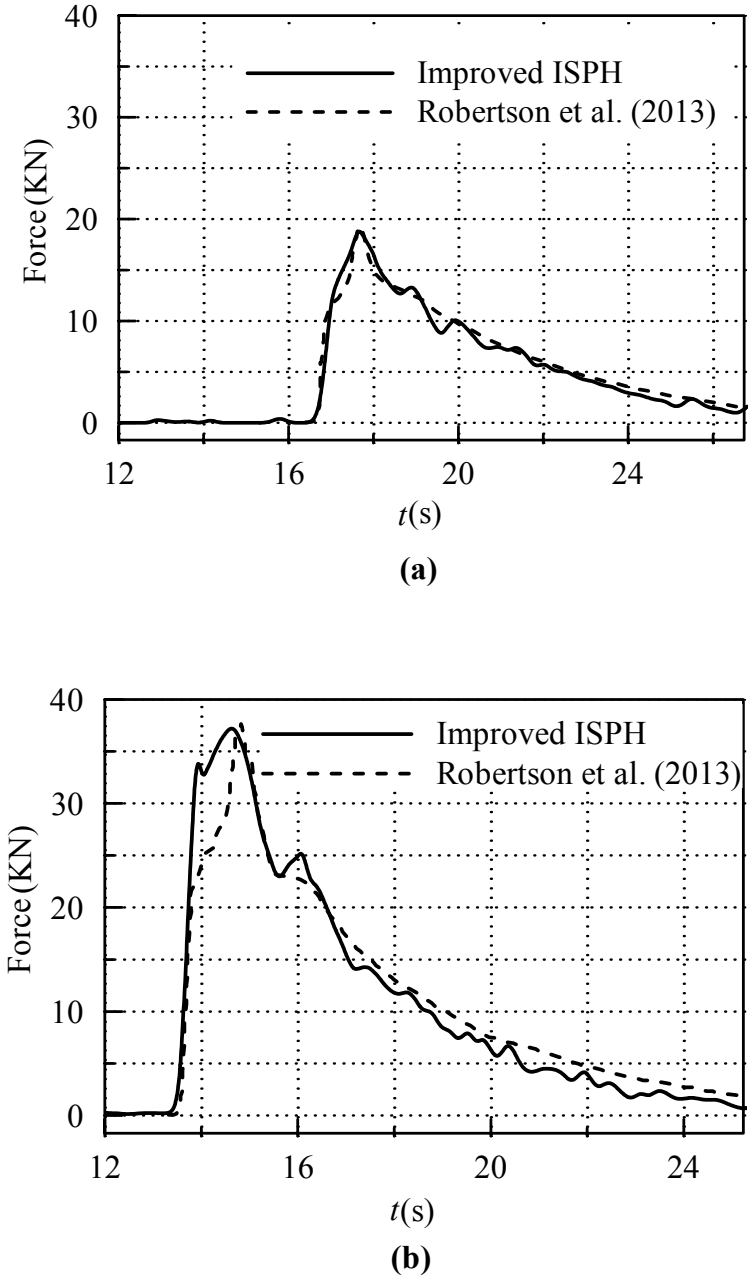

Figure 5.9. Time histories of computed wave forces by ISPH and experimental data of Robertson et al. (2013). (a) Wave height H=53.2 cm; (b) Wave height H=106.4 cm

To reveal the spatial and temporal evolution features of the solitary wave during the whole simulations, the computed particle snapshots are shown in Figure

5.10 at several typical times for the case of larger wave height of 106.4 cm. To study the pressure distributions of the wave flow, the pressure contours are also shown in the same figure. Figure 5.10 shows that the wave started to propagate over a flat bed at time $t = 2$ s, shoaled over the slope at $t = 4$ s and broke and plunged downward onto the water at $t = 7.2$ s. After the wave breaking, it turned into a fully turbulent bore running along the horizontal reef at $t = 9.0$ s. The initial wave impact on the right wall happened at $t = 13.8$ s, after which the wave ran up along the wall to its maximum height around $t = 14.2$ s. Finally, the wave flow returned down and reflected back as a returning bore at time $t = 15.8$ s.

Besides, it is also seen that the pressure distributions in most of the flow region are nearly hydrostatic, which is indicated by the fact that the pressure contours are equally spaced and consistent with the free surface levels. However, during the wave breaking at $t = 7.2$ s and wave impact at $t = 13.8$ s, etc, the local pressure patterns deviated markedly from the hydrostatic law, and the pressure values are much larger than the hydrostatic values. For example, during the initial wave impact at $t = 13.8$ s, very large impact pressure was generated at the impact point on the right wall.

These findings imply that the hydrostatic assumption used in the Shallow Water Equations (SWEs) type models can be used for the wave propagation problems with enough accuracy up to the violent wave breaking and impacting point but additional algorithms must be included to address the local pressure variations around the breaking and impacting zones, otherwise relatively large errors could be induced due to the hydrostatic pressure assumptions. It is worth mentioning that recently quite a few SWEs based SPH models have been developed with promising potentials in simulating the shallow water flows (Chang and Chang, 2013; Vacondio et al., 2013; Xia et al., 2013).

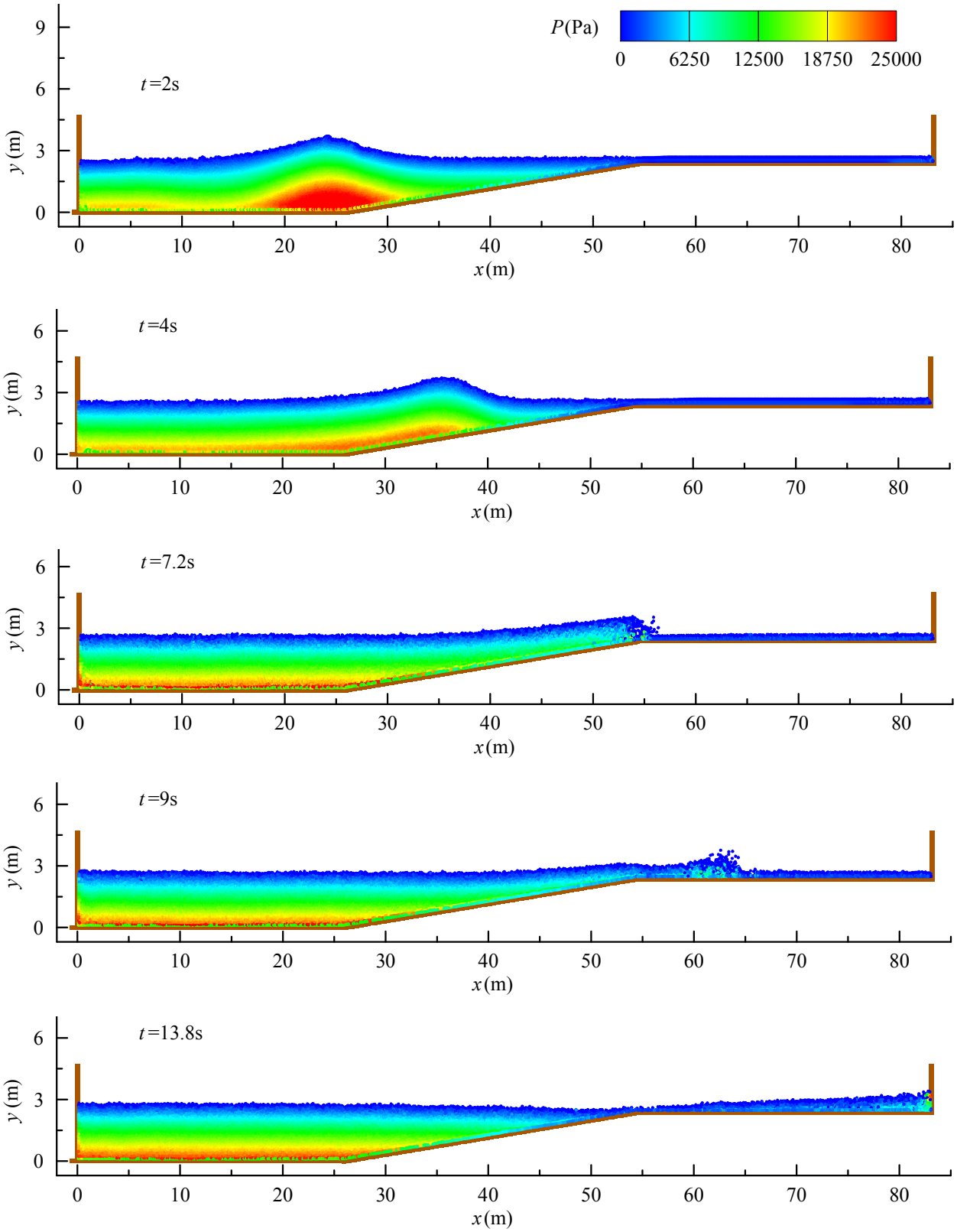
P(Pa)
0
6250
12500
18750
25000
t=2s
t=4s
t=7.2s
t=9s
t=13.8s
y (m)
x (m)
0
3
6
9
0
10
20
30
40
50
60
70
80

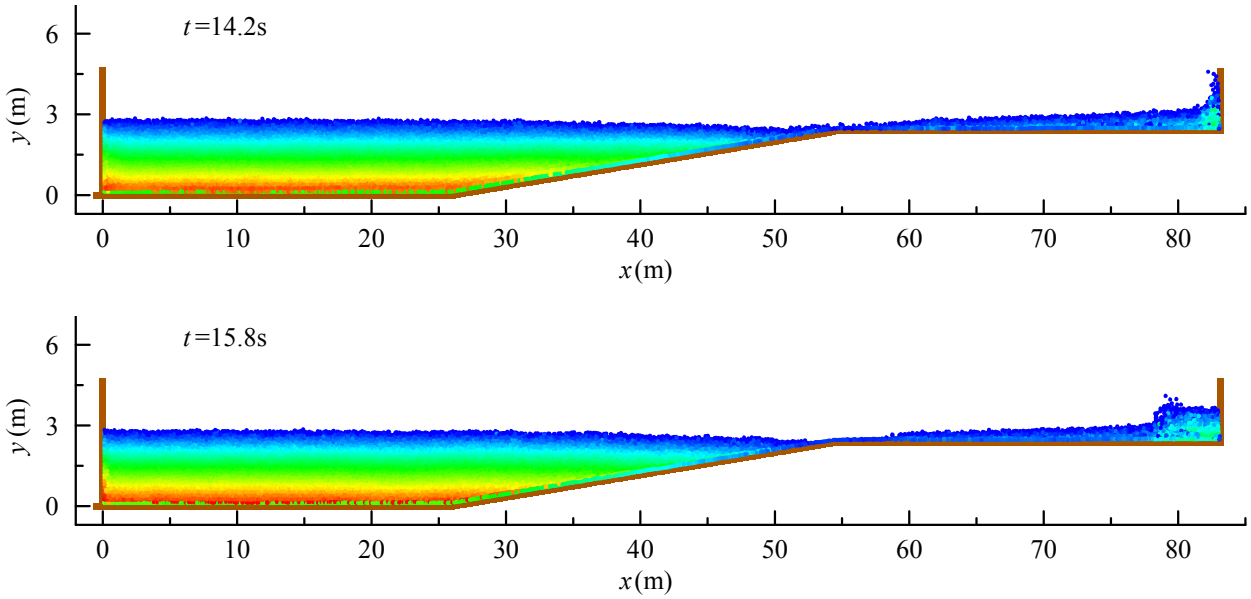

Figure 5.10. ISPH computed particle snapshots with pressure contours at different times (wave height H=106.4cm)

To evaluate the performance of different PPE source term treatments in ISPH for the wave force predictions, the density-invariant source term equation (3.12) and velocity divergence-free source term equation (3.16) are separately used to re-compute the time histories of wave impact forces on the right wall based on the same computational settings. The results are shown in Figure 5.11 (a) and Figure 5.11 (b), for the initial wave height of 53.2 cm and 106.4 cm, respectively. Meanwhile, the mixed source term results based on equation (5.1) and experimental data of Robertson et al. (2013) are also shown for a comparison. It can be seen that the computed wave forces follow the same trends as the wave impact pressures in the previous dam break simulation, in that the pure density-invariant model predicted a higher and more fluctuating force evolution while the pure divergence-free model predicted a smaller and smoother force evolution, but the ranges of over- and under-prediction are much less than those in the dam break case due to the integration of pressures which greatly reduced the large fluctuations. For both wave heights, the pure density-invariant ISPH model overestimated the peak wave forces by 55% ~ 60%, while the pure divergence-free ISPH model under-predicted the peak wave forces by 65% ~ 70%.

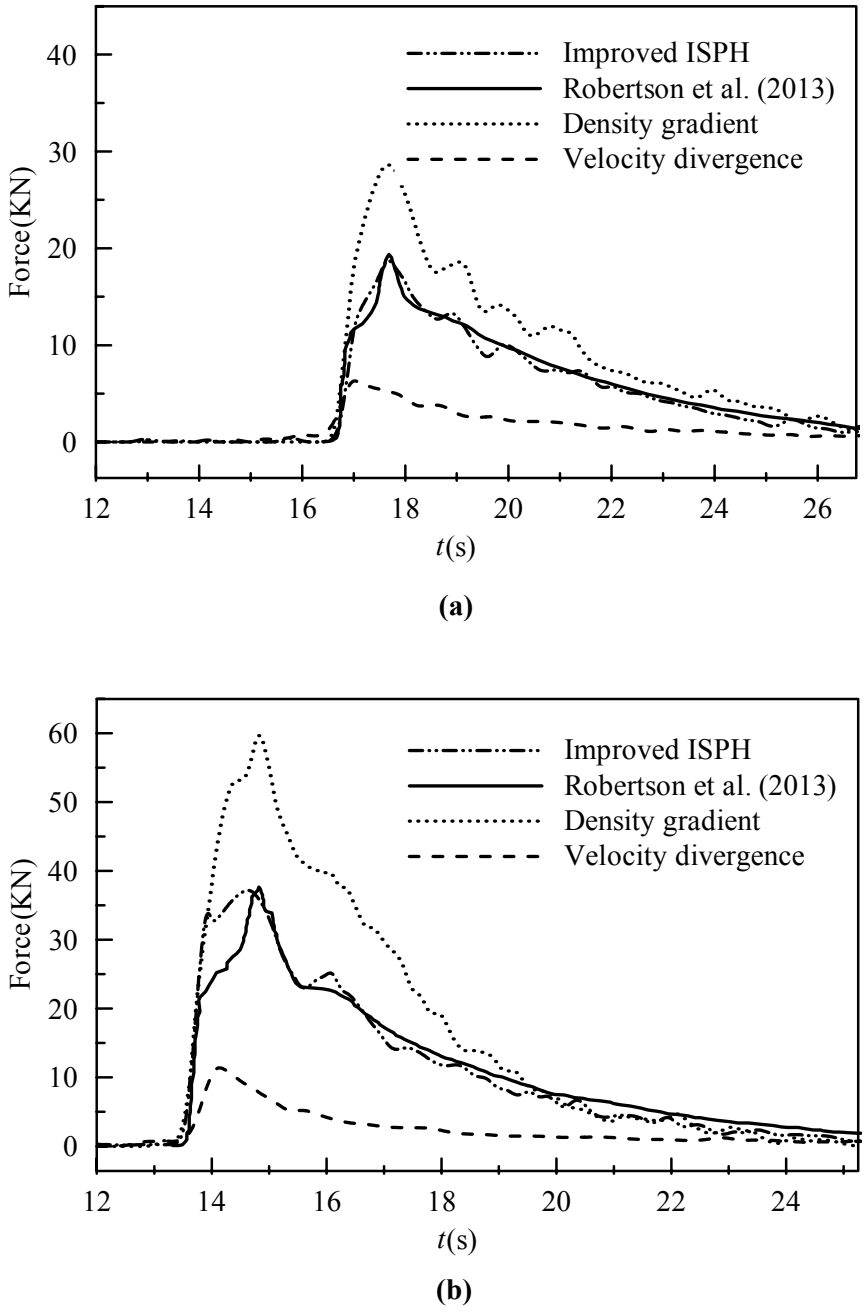

Figure 5.11. Time histories of computed wave forces using the three different ISPH source terms and experimental data of Robertson et al. (2013). (a) Wave height H=53.2 cm; (b) Wave height H=106.4 cm

5.4 Comparisons with WCSPH solutions

As recently found in some SPH studies (Chen et al., 2013; Hughes and Graham, 2010), the WCSPH could perform better in the fluid impact pressure simulations in view of obtaining a more stable and smoother pressure field. To investigate this finding, in this section I consider another benchmark dam break problem for which a wide range of WCSPH results were available. Here the dam break problem as described by Colagrossi and Landrini (2003) is studied.

The initial column of water covered a rectangular dimension of 2 m wide and H=1 m high, and the right wall of the numerical tank is positioned 5.366 m from the left wall. A schematic view of the numerical tank is shown in Figure 5.12. Adami et al. (2012) used the WCSPH with an improved solid boundary treatment to compute the impact pressures measured in the bottom region of the right wall. An initial particle spacing of D_0 = 0.01 m was used in their simulations.

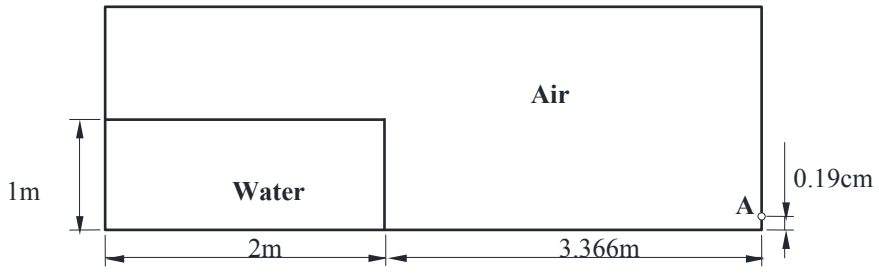

Figure 5.12. Schematic view of numerical tank for dam break flow (Colagrossi and Landrini, 2003)

On the other hand, Marrone et al. (2011) used a novel δ-SPH scheme based on the addition of a numerical diffusion term into the continuity equation to compute similar dam break problems with an initial particle spacing D_0 = 0.015 m ~ 0.001875 m. Smaller particle spacing could reduce the particle oscillation to some extent as well as provide a less fluctuation pressure time history. D_0 = 0.02 m is used here due to the limitation of compute performance. I will compare our ISPH

results computed by using the PPE source term equation (5.1) with these two WCSPH solutions to show the robustness of the mixed source term formulation.

For quantitative validations, in Figure 5.13 I compare the temporal pressure profiles at the downstream wall for three different SPH results as mentioned above with the experimental data of Buchner (2002). It is shown that the pressure profiles obtained with Adami et al. (2012) contain some high frequency oscillations although the main pressure plateau is reasonably captured. According to Adami et al. (2012), the strong pressure peak around $t(g/H)^{1/2} = 6$ was caused by the plunging wave rolling-up after the flow hit the wall and the numerical peak occurred slightly later because the air cushion effect was not considered in their single phase simulations. However, it should be noted that Adami et al. (2012) results have been obtained without the XSPH and normalization of density. Thus it can be compared on the equal basis with the proposed ISPH model in which no additional numerical smoothing techniques were used.

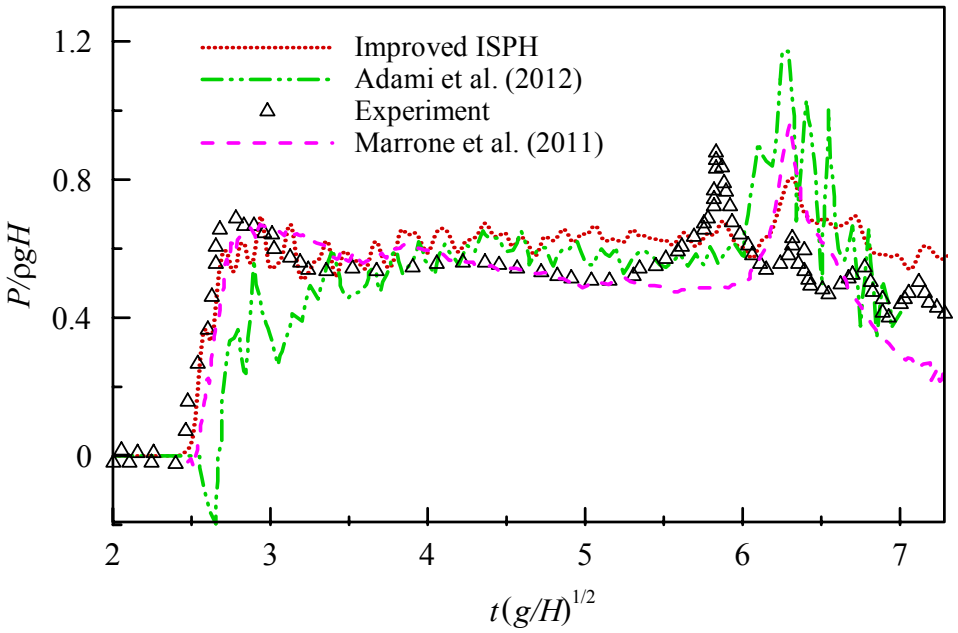

Figure 5.13. Time histories of computed pressures by the present ISPH, improved WCSPH (Adami et al., 2012), δ-SPH (Marrone et al., 2011) and experimental data (Buchner, 2002)

The ISPH results in Figure 5.13 indicated that the mixed source term formulation provided a very promising pressure time history in that not only pressure noises were reduced but also several smaller pressure peaks after time $t(g/H)^{1/2}$ = 6 as observed in the experiment of Buchner (2002) were well captured. Although the largest pressure peak was also delayed in the ISPH computations, the amplitude of pressure has been much better reproduced.

On the other hand, the ISPH results are slightly poorer than the δ-SPH results of Marrone et al. (2011) until time $t(g/H)^{1/2}$ = 6, which is due to that the latter included more advanced numerical treatment by including the artificial diffusive term into continuity equation to remove the spurious high-frequency pressure oscillations. Nonetheless, Marrone et al. (2011) only reproduced the largest pressure peak around time $t(g/H)^{1/2}$ = 6 (based on the particle spacing D_0 = 0.015 m) and then the pressure curve drastically dropped down. In contrast, the ISPH recorded two subsequent smaller pressure peaks that were also found in the experimental data. The fact that Marrone et al. (2011) also reproduced these smaller pressure peaks using the most refined particle spacing D_0 = 0.001875 m and the ISPH achieved similar results by using D_0 = 0.02 m is a good indication that the proposed mixed source term model is effective in both reducing the pressure noises and accurately predicting the pressure histories.

5.5 Numerical error analysis of different source term treatments

The preceding model applications have served to demonstrate that the mixed source term ISPH model performed much more promisingly than the corresponding source term model by using either a density-invariant or a velocity divergence-free formulation. In this section, I will carry out a series of numerical error analysis to quantify the PPE source term errors and thus provide a theoretical rational for the robustness of the mixed source term model.

Generally there are two main errors arising from any ISPH projection scheme which are the particle density error and the velocity divergence error. The former is due to the change of the particle volume from either the compression or expansion, while the latter is due to the non-conservation of the particle flow fields. In a pure density-invariant ISPH approach such as Shao and Lo (2003), we would expect that the conservation of particle volume is well observed, but in a pure divergence-free ISPH approach such as Cummins and Rudman (1999), we would expect that the conversation of particle velocity field is well followed. As far as the present knowledge is concerned, only a limited number of works have been carried out to quantify the particle density errors in the ISPH projection scheme, such as Cummins and Rudman (1999), Asai et al. (2012) and Szewc et al. (2012). However, with regard to the evaluation of the velocity divergence errors no documented results have ever been reported. The understanding of these fundamental errors would be very useful for understanding and improving the ISPH modelling performance, as they could greatly influence the model predictions of the macro flow properties such as the flow impact pressures and forces, etc.

In the following error analysis, the particle density error is quantitatively evaluated through the normalized density errors between the corrected and initial constant densities as:

$$E_{den}\left(t\right)=\frac{1}{N'}\sum_{i=1}^{N'}\left|\rho_i\left(t\right)-\rho_0\right|/\rho_0 \tag{5.2}$$

where ρ_i is the density of particle i calculated after correction step. $\rho_i\left(t\right)$ is the density time series of particle i. The search of the neighbouring particles includes the inner fluid particles only. For the velocity divergence error, it is quantified through the average of divergence values of the corrected particle velocities as

$$E_{div}\left(t\right)=\frac{1}{N'}\sum_{i=1}^{N'}\left|\nabla\cdot\mathbf{u}_i\left(t\right)\right| \tag{5.3}$$

where $\nabla \cdot \mathbf{u}_i$ is the velocity divergence of particle *i* calculated after correction step. $\nabla \cdot \mathbf{u}_i(t)$ is the velocity divergence time series of particle *i*.

5.5.1 Numerical error in temporal domain

Based on the numerical simulations in the previous section for the dam break flow of Lee et al. (2011), Figure 5.14 and Figure 5.15 showed the time histories of the particle density and velocity divergence errors, respectively, for the three different source term formulations as represented by equation (3.12), equation (3.16) and equation (5.1). Figure 5.14 showed that the particle density error is the smallest for a strict density-invariant ISPH model, in which the variation of particle volume is under 1%. In contrast, the particle density error is quite large in a pure divergence-free ISPH model, in which not only the largest error reached 24% but also the error curve fluctuated greatly.

By closely examining the relevant particle snapshots and velocity fields as shown in Figure 5.5, we could easily understand that these large fluctuations are associated with the rapid flow deformations and impacts. For example, in Figure 5.14 the first peak error around time t = 0.44 s is the result of dam break flow impacting on the right wall, the second peak error before t = 1.5 s is due to the returning flow plunging onto the water surface, and the last peak error corresponds to the generated bore flow hitting on the left wall. Figure 5.14 also shows the density error for the mixed source term model is only 2% ~ 3% larger than that of the strict density-invariant model, but it is significantly smaller than the error produced by the pure divergence-free model. Some previous works (Xu et al., 2009) found that the divergence-free ISPH model could become unstable in certain circumstances and this could be due to the violation of particle volume conservation, or the compression of the fluids. The mixed source term formulation improved the volume conservation of fluid particles and thus made the computation more stable.

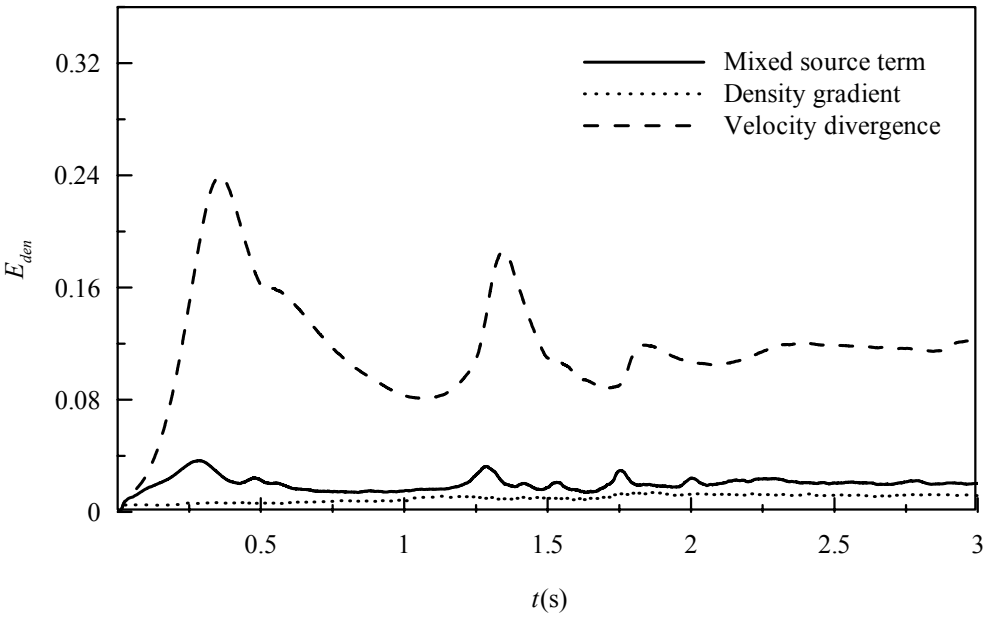

Figure 5.14. Time histories of source term errors due to different formulations: Density error

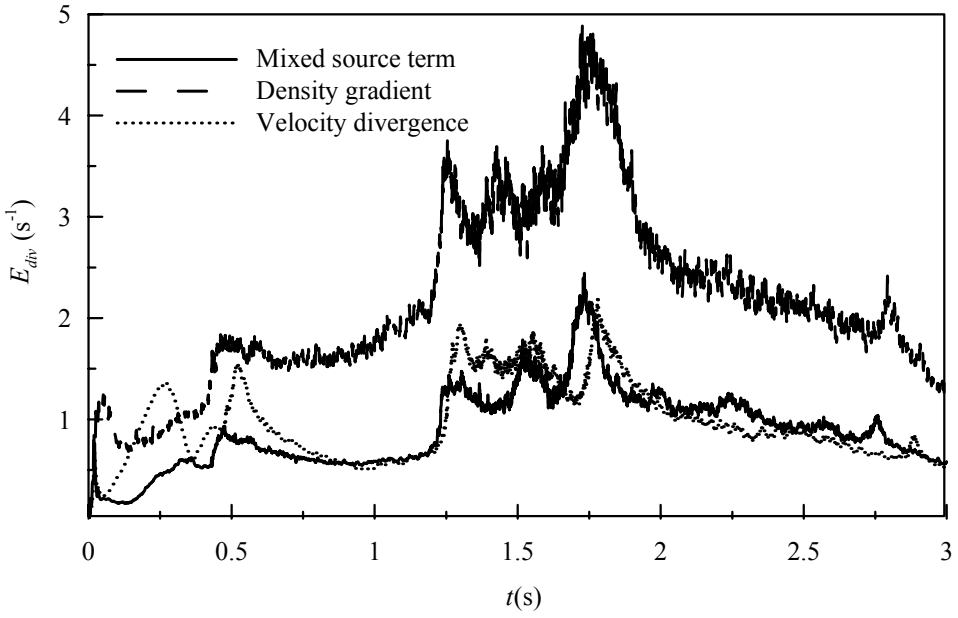

Figure 5.15. Time histories of source term errors due to different formulations: Velocity divergence error

On the other hand, examining the velocity divergence errors in Figure 5.15 reveals that a strict density-invariant ISPH formulation could generate relatively large divergence errors while a strict divergence-free ISPH formulation could reduce this error by about 50%. It is interesting to notice that the fluctuation features of divergence errors in Figure 5.15 are quite consistent with those of the density errors in Figure 5.14, in that the peak errors appear around the same time instants when the flows are undergoing the severe impacts and free surface deformations.

However, it is also found out that the divergence errors in Figure 5.15 appear to be similar for both the mixed source term model and the pure divergence-free model. The reason is likely to be that the density and divergence errors are internally interrelated with each other. In a strict divergence-free model, as the particle volume conservation is not satisfied as shown in Figure 5.14, this could also influence the correct projection of the particle velocity fields. Thus the simple imposition of divergence-free condition alone in a particle method cannot achieve the best divergence-free flow field, which is different from the grid modelling techniques. In comparison, in the mixed source term model, as the particle volume conservation is guaranteed and the density error is reduced, this can also make the projection of particle velocity fields more accurate. As a result, the mixed source term ISPH scheme achieved the same velocity divergence errors as the pure velocity divergence-free model.

As a further investigation on the different source term formulations, the time histories of the particle density and velocity divergence errors are determined as shown in Figure 5.16 and Figure 5.17, for the three source terms as represented by equation (3.12), equation (3.16) and equation (5.1), based on the previous numerical simulations of dam break flow of Colagrossi and Landrini (2003). Besides, similar results are also presented for the solitary wave impact case of Robertson et al. (2013) in Figure 5.18 and Figure 5.19, for the small wave height of 53.2 cm.

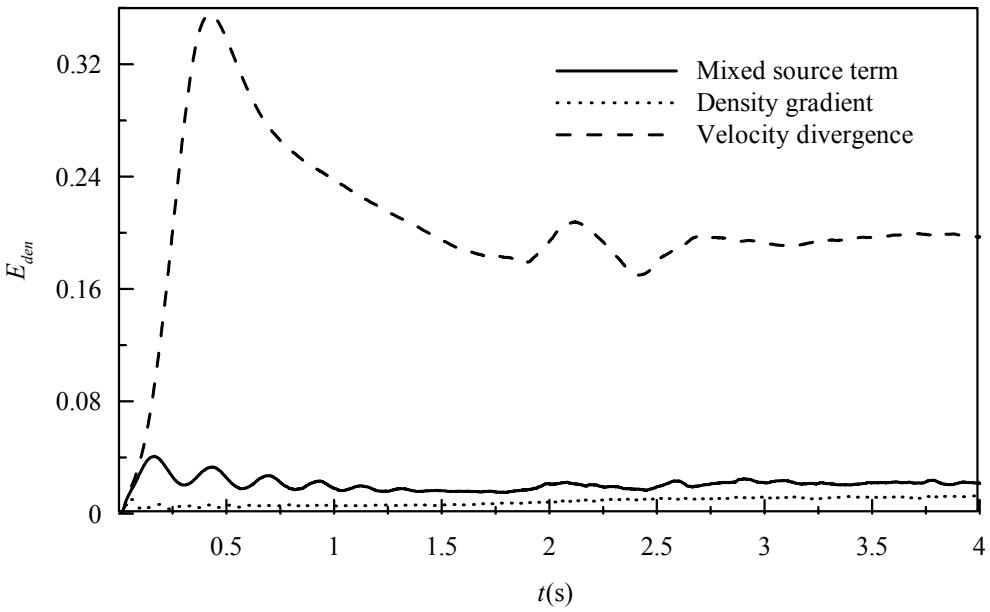

Figure 5.16. Time histories of errors from different source term formulations for dam break flow of Colagrossi and Landrini (2003): Density error

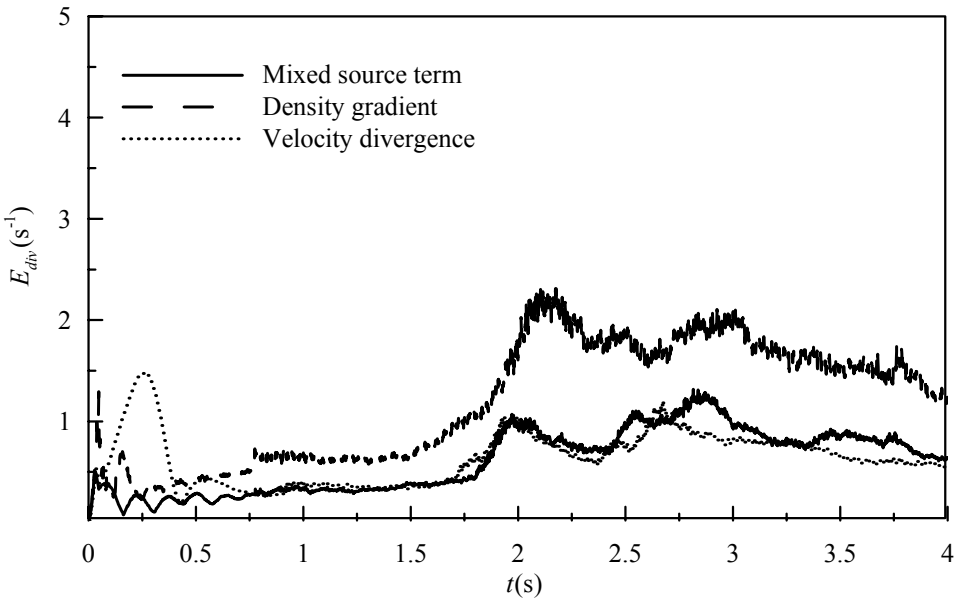

Figure 5.17. Time histories of errors from different source term formulations for dam break flow of Colagrossi and Landrini (2003): Velocity divergence error

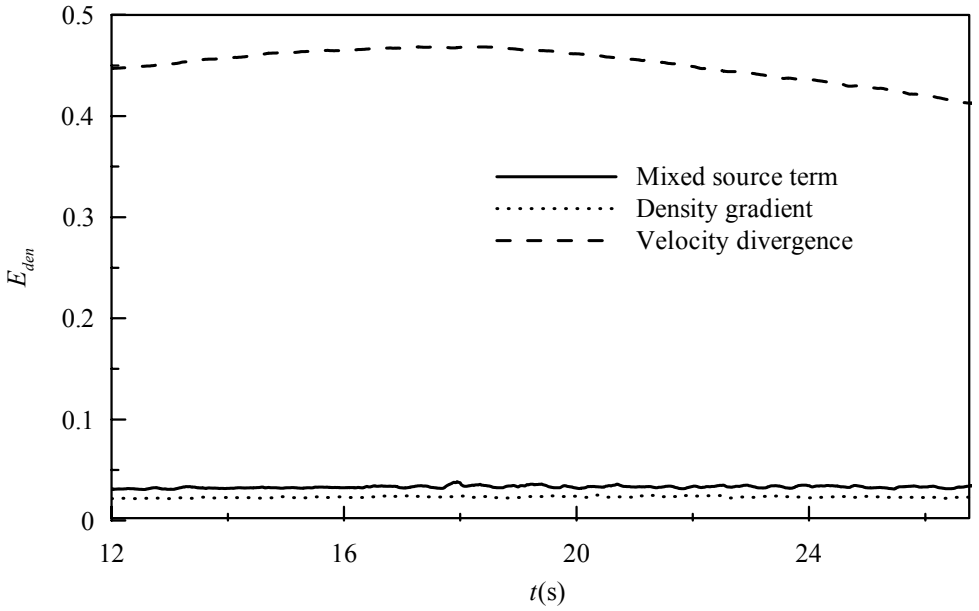

Figure 5.18. Time histories of errors from different source term formulations for solitary wave impact of Robertson et al. (2013): Density error

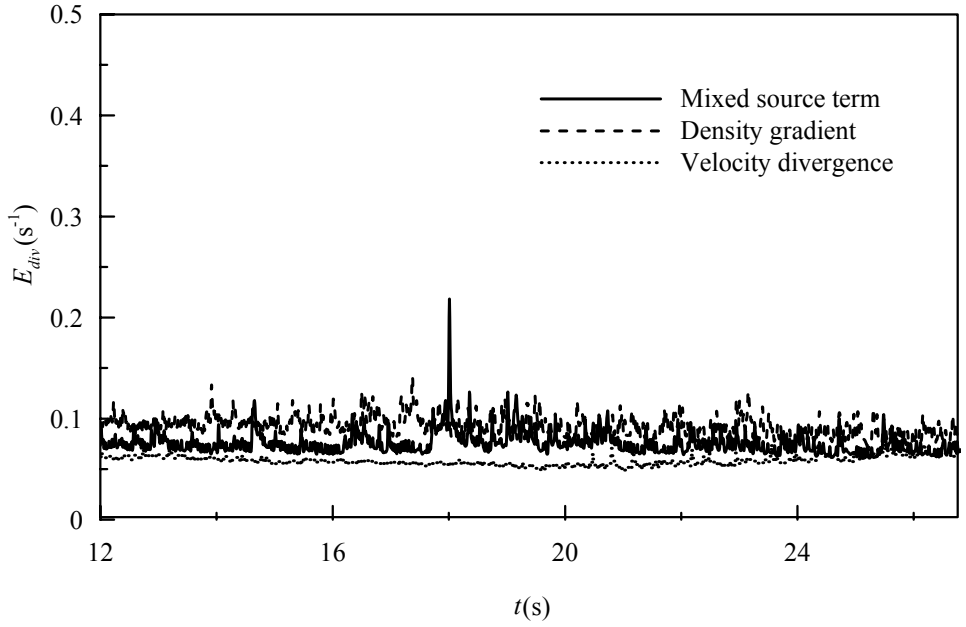

Figure 5.19. Time histories of errors from different source term formulations for solitary wave impact of Robertson et al. (2013): Velocity divergence error

Figure 5.16 and Figure 5.17 showed the same error features as those in Figure 5.14 and Figure 5.15, in that the mixed source term model achieved the most optimum numerical performance in view of reducing the density and divergence errors, and also the two errors are consistent with each other for the appearance of peak values. In fact this is of no surprise as both cases are for the instantaneous dam break flows and thus should have similar hydrodynamic mechanisms. On the other hand, the density and divergence errors of solitary wave impact as shown in Figure 5.18 and Figure 5.19 have somewhat different evolution patterns. For example, Figure 5.18 demonstrated that the density error for a pure divergence-free source term formulation could be as large as 45% in a long time simulation, while Figure 5.19 indicated that the divergence error for the mixed source term lies somewhere between that of the pure density-invariant and divergence-free models, rather than close to the latter as in the two dam break flow cases. At this stage we could only attribute this discrepancy to the different hydrodynamic features of the flow and the duration of simulation time. However, a very promising phenomenon observed is that both the dam break flows and solitary wave impact shared some similar features such as: (1) the mixed source term could achieve the optimum density and divergence errors simultaneously; (2) the peak density and divergence errors always appear during the violent fluid motions such as wave impact. For example, in the solitary wave case, the maximum density and divergence errors both occurred around time t=18 s as shown in Figure 5.18 and Figure 5.19, while in the violent wave impact case they happened at t=17.67 s as shown in Figure 5.9 (a).

5.5.2 Numerical errors in spatial domain

In the preceding analysis, we found that relatively large density and velocity divergence errors are always associated with the rapid flow deformation and impact. To numerically support this statement here we further examine the spatial distribution of these errors for the dam break flow of Lee et al. (2011), during the violent flow impact on the right wall. Figure 5.20 (a) and (b) showed the density and divergence errors for the mixed source term model equation (5.1), while Figure 5.21 (a) is the density error for the density-invariant model equation (3.12) and Figure

5.21 (b) is the velocity divergence error for the divergence-free model equation (3.16), respectively.

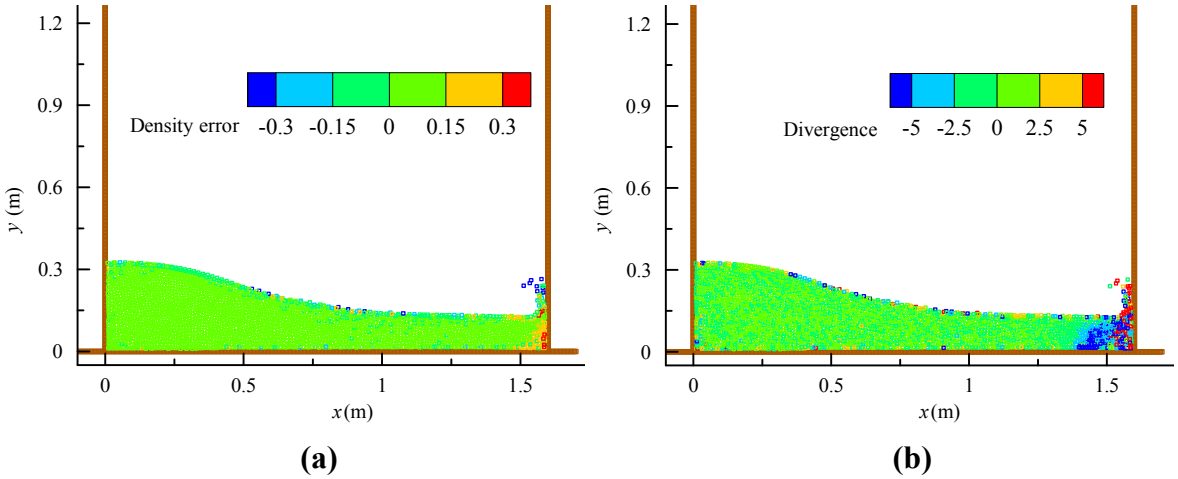

Figure 5.20. Spatial distributions of errors from different source term formulations for dam break flow of Lee et al. (2011): (a) Density error for mixed source term; (b) Velocity divergence error for mixed source term;

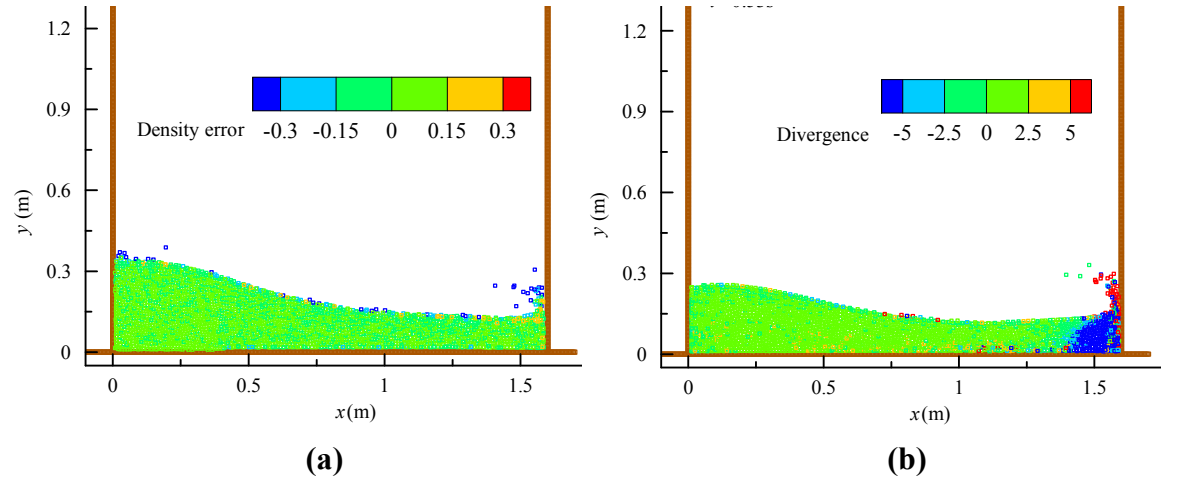

Figure 5.21. Spatial distributions of errors from different source term formulations for dam break flow of Lee et al. (2011): (a) Density error for density-invariant model; (b) Velocity divergence error for divergence-free model

Figure 5.20 and Figure 5.21 clearly demonstrate that large density and divergence errors are concentrated within the impact region near the right wall, especially around the upward flowing jet where the water surface undergoes large deformation. Besides, some of the larger density and divergence errors are also found on the free surface particles across the computational domain. In comparison, these errors are quite small within the inner fluid region away from the solid boundary and free surface.

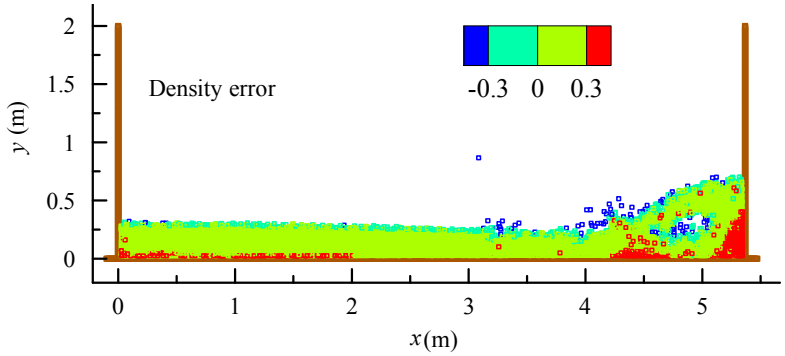

(a)

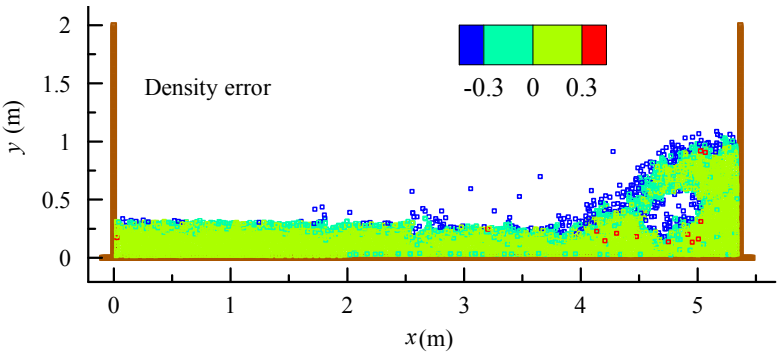

(b)

Figure 5.22. Spatial distributions of density errors for dam break flow of Colagrossi and Landrini (2003): (a) Divergence-free source term and (b) Mixed source term

In some earlier results, we have observed that the velocity divergence errors in the pure divergence-free source term model may have arisen from the particle

volume conservation. To provide a rational for this, Figure 5.22 (a) and (b) showed the spatial plot of particle density errors at the time when the velocity divergence error is large, for the divergence-free source term equation (3.16) model and mixed source term equation (5.1) model, respectively. The result is based on the dam break flow of Colagrossi and Landrini (2003) at the stage when the flow overturned from the right wall and plunged onto the water surface at normalized time $t(g/H)^{1/2}=$ 6.25 as shown in Figure 5.13. Figure 5.22 (a) showed that for a pure divergence-free source term model the density error or particle volume non-conservation is obviously larger especially within the impact region near the solid boundary, while these errors have been effectively reduced in the mixed source term model as shown in Figure 5.22 (b).

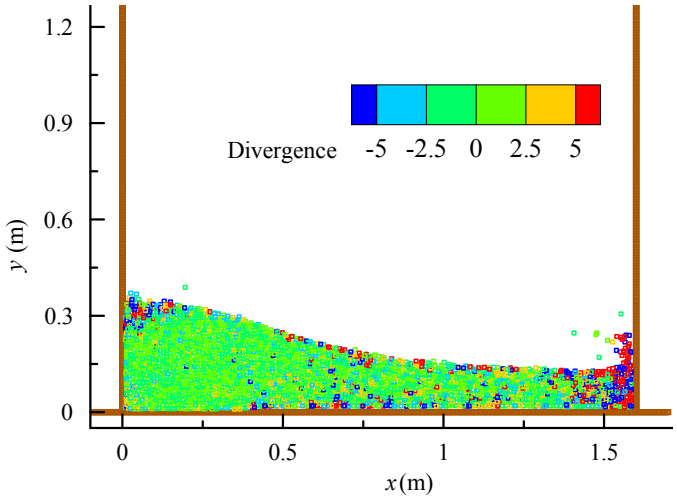

Figure 5.23. Spatial distributions of velocity divergence errors for density-invariant source term model for dam break flow of Lee et al. (2011)

Finally, to further investigate why the velocity divergence error is large for the density gradient source term, the spatial plots of the velocity divergence errors and pressure fields for the dam break flow of Lee et al. (2011) during the flow impact on the right wall are shown in Figure 5.24 (a) and (b), respectively, for the density-invariant source term equation (3.12) model. Figure 5.23 demonstrated a noisy divergence field that is closely correlated with the noisy pressure and velocity

distribution patterns near the dam site as well as impact zone, as shown in Figure 5.24.

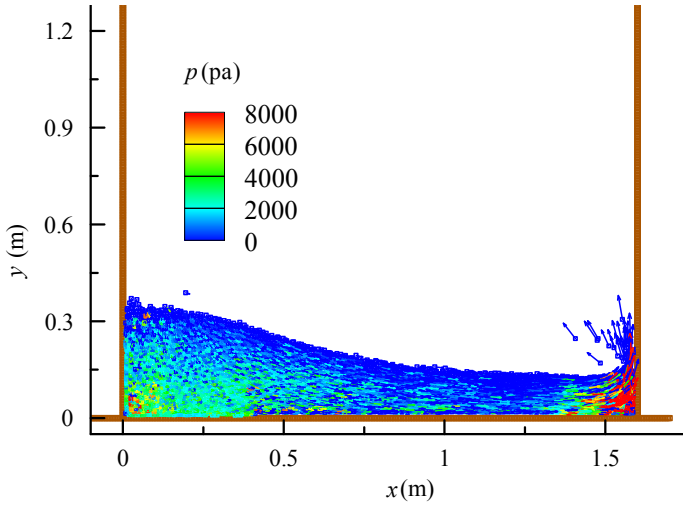

Figure 5.24. Spatial distributions of pressure and velocity fields for density-invariant source term model for dam break flow of Lee et al. (2011)

5.6 Summary

To improve the ISPH modelling capacity a mixed source term model has been proposed by combining the standard density-invariant and the velocity divergence-free formulations in a weighted average form. The new model was applied to two benchmark dam break flows and one solitary wave impact problem for two different wave heights. By comparing with the documented experimental data and numerical results, it was found that the mixed source term ISPH model predicted more accurate impact pressure and force as compared with the results obtained by using either the density-invariant or the velocity divergence-free ISPH model.

To further quantify the numerical errors generated from different ISPH source term treatments, the temporal and spatial distributions of the particle density and velocity divergence errors were investigated. Not only we have found that the numerical errors were closely linked with the violent fluid deformation and impact,

but also it has been disclosed that a strict density-invariant model could generate relatively larger divergence error while a strict divergence-free model could generate relatively larger density error. The mixed source term model can effectively reduce both errors in an optimum manner and thus gave the best numerical performance in predicting the macro flow behaviours.

Chapter 6

Development of ISPH model for porous structures

Permeable structures such as rubble-mound breakwaters are widely used to protect coastal facilities and beaches from wave attack. Unlike impermeable structures, the interaction between waves and porous structures takes place both outside and inside of the structure. When reaching the porous structure waves are usually partially reflected by the structure and some of the incoming wave energy dissipates outside the porous structure. However, inside the porous structure such as rubble mount breakwaters, the violent flow in the pores can destabilise individual armour stones and may sometimes threaten the stability of the whole structure eventually. Therefore, the ability to quantify accurately the flow motion in and around the porous structure is vital for understanding the mechanism of structure instability induced by wave action.

6.1 Introduction

Sollitt and Cross (1972) developed one of the earliest models for describing flow through permeable structures by adding inertial and nonlinear resistance forces into the momentum equations to account for the effect exerted on the porous flow by the solid skeleton of the porous structure. Since then many improved models have been proposed to investigate a wide range of wave propagation problems including wave transmission, reflection and dissipation around and through arbitrarily shaped breakwaters with porous layers. The notable models include those based on potential flow theory (Sulisz, 1985; Yu and Chwang, 1994), the mild-slope equation

(Rojanakamthorn et al., 1989), and the shallow water equations (Kobayashi and Wurjanto, 1990; Wurjanto and Kobayashi, 1993). Unfortunately, the predictive capability of these simplified models are rather restricted as they are unable to account for some essential flow processes such as nonlinearity (mild slope equation), frequency dispersion (shallow water equation) or wave breaking (potential flow equations).

In the recent decades, more general and rigorous models have been developed starting from the model by van Gent (1995) based the Reynolds-averaged Navier-Stokes equation and also including those by Huang et al. (2003) and Liu et al. (1999). Liu et al. (1999) derived the Reynolds-averaged Navier-Stokes equations for the porous flow to study the wave overtopping on the porous breakwater. To solve the governing equations, they employed the resistance force formulas proposed by van Gent (1995) and calibrated the linear coefficient against simple physical experiments, while keeping the inertial and original nonlinear frictional coefficients unchanged. In addition, $k-\varepsilon$ turbulence model was incorporated to determine turbulent stresses for flow outside the porous media. Similarly Hsu et al. (2002) used the Volume Averaged RANS equations (VARANS) to describe the flow motion around the porous structure, Karunarathna and Lin (2006) applied their VARANS models to study the wave damping over a porous seabed later. Garcia et al. (2004) and Lara et al. (2006) used the numerical model of Liu et al. (1999) to investigate wave interactions with a low-crested permeable breakwater and validated their model with the laboratory measurements. Huang et al. (2003) coupled the unsteady 2D laminar NS equations model and Navier–Stokes type model to solving the flow outside and inside the porous structure separately for the solitary wave interaction with submerged permeable breakwater. More recently, Huang et al. (2008) also studied the wave damping over a porous seabed by using their coupling model and compared the numerical results with theoretical and experimental data. After pointing out that none of the approaches, even the widely used volume averaged RANS equations (VARANS) (Hsu et al., 2002; Slattery, 1999) and time averaging volume-averaged equations (de Lemos, 2006), are sufficient to reproduce data for

different coastal applications, del Jesus et al. (2012) derived a new unified equation--VARANS equations for simulating porous flow.

All of the above-mentioned models are based on the Eulerian approach and, for large free surface deformation, require an explicit surface capturing scheme to determine the wave profile. In comparison, the Lagrangian SPH model is much more advantageous as it can determine the free surface profiles simply by tracing the particle positions both outside and within the porous structures.

Zhu (1999) developed a SPH model for the low Reynolds number incompressible flows inside the porous media and imposed a periodic porous boundary condition at both ends of the computation domain. The porous solid skeleton was discretized and represented by fixed SPH particles in detail. Tartakovsky and Meakin (2006) also applied the SPH method to simulate the pore-scale flow transportation and analysed the effect of fluid wetting behaviours and surface tensions. Herrera (2009) derived a new SPH formulation for the simulation of advective-dispersive solute transport in heterogeneous porous media based on the Navier-Stokes equations and a predictor-corrector solution process, Although modelling the porous flow at the pore scale can reveal the detailed information of the flow motion, it is extremely computationally expensive and not yet practical for engineering computations.

The first ISPH model for wave interactions with porous media in larger scale was proposed by Shao (2010) who applied the model for simulating solitary wave interacting with a submerged porous breakwater. Then Akbari and Namin (2013) improved the model of Shao (2010) by introducing a finer background mesh with porosity information in the whole computational domain to treat the interface more accurately. But different particle sizes were used in pure fluid zone and porous zone without considering the different influence zone of kernel function at the interface region on the predictions. Recently, Ren et al. (2014) also studied wave interaction with porous structures using an improved weakly compressible smoothed particle hydrodynamic method (WCSPH) model. In the model of Ren et al. (2014), the tangential velocities were averaged near the porous interface to obtain a continuous pressure field, but the tangential velocity is not continuous in their model.

This chapter begins with the description of the governing equations of both flows outside and outside the porous media. After that, a boundary treatment was proposed to deal with the interface between pure fluid region and porous media region. The accuracy of the numerical model for porous structures study was verified by comparing the numerical results of wave damping over a porous bed with the theoretical solution of Packwood and Peregrine (1980) . Finally, the SPH model was applied to investigate the features of flow field around and inside of a submerged porous breakwater, such as velocity and pressure and comparisons were made with experimental results of Wu and Hsiao (2013).

6.2 Governing equations

del Jesus et al. (2012) analysed two main sets of governing equations for porous flow and revealed that there is no unique governing equation for computing porous flow due to either the differences in the friction term in momentum equations or the different closure models used. Naturally, the governing equations of flow inside the porous media and outside the porous media are different from each other. Since Navier-stokes equations were widely used for the flow modelling outside the porous media, herein, the unsteady two-dimensional Navier–Stokes equations with Lagrangian form are used for solving flows outside of porous media. Navier–Stokes type equations with Lagrangian form, which was proposed by Huang (2003) for porous flows in the Euler form, are used for solving flows inside of porous media.

6.2.1 Flow outside the porous media

Following Huang et al. (2003) and Shao (2010), the flow outside of the porous media is considered as laminar and can be solved by two-dimensional unsteady Navier-Stokes equations. The Lagrangian form of the Navier-Stokes equations is expressed as equation (6.1) and equation (6.2) in the SPH framework.

$$\frac{1}{\rho}\frac{d\rho}{dt} + \nabla \cdot \mathbf{u}_w = 0 \tag{6.1}$$

$$\frac{d\mathbf{u}_w}{dt} = -\frac{1}{\rho}\nabla P + \mathbf{g} + \nu\nabla^2\mathbf{u}_w \tag{6.2}$$

where $\rho =$ density; $t =$ time; $\mathbf{u}_w =$ flow velocity outside of porous structure; $P =$ pressure; $g =$ gravitational acceleration and $\nu =$ laminar viscosity.

As for laminar flow, the turbulence is not considered in equation (6.2) similar to the approach taken by Huang et al. (2003) in order to simplify the interface boundary conditions with the porous flow region. However, Huang et al. (2003) indicated that this simplification could cause some errors in describing wave breaking. Therefore, the case studies in this thesis are limited to non-breaking situations.

6.2.2 Flow inside of the porous media

Following Huang et al. (2003) and Shao (2010), the governing equation for flow inside of the porous media is solved by the Navier-Stokes equation with added linear and nonlinear drag force terms in the in momentum equation, are

$$\frac{1}{\rho}\frac{d\rho}{dt} + \nabla\cdot\mathbf{u}_p = 0 \tag{6.3}$$

$$\frac{d\mathbf{u}_p}{dt} = -\frac{1}{\rho}\nabla P + \mathbf{g} + \nu\nabla^2\mathbf{u}_p - \frac{\nu n_w}{K_P}\mathbf{u}_p - \frac{C_f n_w^2}{\sqrt{K_P}}\mathbf{u}_p\left|\mathbf{u}_p\right| \tag{6.4}$$

where $n_w =$ porosity of the porous media; $K_P =$ intrinsic permeability and $C_f =$ nonlinear resistance coefficient. Here $\mathbf{u}_p$ is the discharge velocity which equals to the seepage velocity multiplied by the porosity for the porous media. Discharge velocity is also referred to as apparent velocity in porous flow literatures. Because of the particle velocity is the apparent velocity in the governing equations, no further velocity treatment is required to satisfy the Beavers and Joseph boundary condition (Ren et al., 2014). This is a big advantage of the particle approach in simulating wave interaction with porous structures.

The left hand side of equation (6.4) is in the form of a full derivative. Comparing equation (6.4) with the governing equation of Huang et al. (2003), it can be found that if the inertia coefficient equals to unity the left hand side of the momentum equation can then be written as the full derivative of particle velocity. The inertial coefficient denotes the added mass effect for accelerating fluid in porous media (Liu et al., 1999). The value of the inertial coefficient is generally known for an isolated simple body, while it's unknown for the random, densely packed materials. For the present study, the value is chosen according to Shao (2010), Akbari and Namin (2013) and Ren et al. (2014), which all used the same value of one.

The last two terms at the right hand side of the momentum equation represent the effect of the fixed porous solid skeleton, with the linear term dominating in the low Reynolds number flow and the square law term in the high Reynolds number flow, respectively.

According to Liu et al. (1999) the turbulence inside the porous structure is usually very weak and negligible in the condition of small permeability of the porous medium. Furthermore, only laminar flow is consider outside of the porous media, so the turbulence effect is ignored for the porous flow and turbulence term is not included in the above equation.

6.2.3 Drag force

Different resistance force equations were applied in Huang et al. (2003) and Huang et al. (2008) for solitary wave propagating over a submerged porous breakwater and a porous bed, separately. According to McDougal (1993) if the porosity n_w and the stone size d of the porous structure are known, the intrinsic permeability K_P can be determined by the following empirical formula

$$K_P = 1.643\times10^{-7}\left[\frac{d_{50}}{d_0}\right]^{1.57}\frac{n_w^{\,3}}{\left(1-n_w\right)^2}, \qquad d_0 = 0.01\text{m} \tag{6.5}$$

And the nonlinear resistance coefficient can be evaluated using the formula given by Arbhabhirama and Dinoy (1973).

$$C_f = 100\left[d_{50}\left(\mathrm{m}\right)\left(\frac{n_w}{K_p} \right)^{1/2} \right]^{-1.5} \tag{6.6}$$

These two equations are used in the following study of solitary wave propagating over a porous bed and interaction with submerged breakwater.

6.3 Computation procedure

As detailed computation procedure was described in section 3.3, only the different parts from that procedure text are given here.

First, it's the two sets of governing equation for flow inside of the porous structure and for pure fluid flow. Ren et al. (2014) pointed out that no additional matching condition is needed to carry out the Beavers and Joseph porous interface boundary condition. Further, Beavers and Joseph (1967) presented that velocity flied is continuous along the interface of the pure fluid and porous materials and. Moreover, the particle velocity in the governing equations of porous flow is the apparent velocity, equal to the particle velocity of the pure fluid flow. Therefore, the presented momentum equations equation (6.2) and equation (6.4) can be solved simultaneously for the entire domain including porous and pure fluids by only setting the friction terms being zero in pure fluid zone. Similar approach was also used by Akbari and Namin (2013), in which a uniform momentum equation with the porosity was proposed for the whole computation domain. When computing the flow in the pure fluid, the porosity equal to unit, while the real porosity of porous structure was used in the computing the flow inside of the porous (Akbari and Namin, 2013).

In addition, the equation of intermediate velocity increment is different. the predict-correct two step was explained in detail for how to solve the governing

equations section 3.3. Similarly, the two resistance force terms in the momentum equation for flow inside of the porous are added in the predict step as equation (6.7) to predict the intermediate particle velocity and particle position, apart from the gravitational force term and viscosity force term. As most parts of the numerical procedure are the same as for the outside flow only the different part of the solution procedure is presented here and the subscript p in $\mathbf{u}_p$ is dropped for simplicity.

$$\Delta \mathbf{u}_* = \left(\mathbf{g} + \frac{1}{\rho} \nabla \cdot \overset{\Rightarrow}{\boldsymbol{\tau}} - \frac{\nu n_w}{K_P} \mathbf{u} - \frac{C_f n_w^2}{\sqrt{K_P}} \mathbf{u} |\mathbf{u}| \right)_t \Delta t \tag{6.7}$$

6.4 Interface boundary

As it can be expected, the most difficult phenomenon in porous flow to treat is the flow exchange across the interface between pure fluid flow region and porous flow region. Since ISPH is a Lagrangian numerical method, the flow exchange means that the fluid particles near the interface need to be allowed to move across the porous interface from both sides and change their positions to relocate in different flow media region at each computational time step.

The physical boundary conditions at the interface are the continuity of the velocities and the continuity of normal and tangential stresses (Beavers and Joseph, 1967; Deresiewicz and Skalak, 1963; Liu, 1973). They can expressed as

$$\mathbf{u}_w = n_w \mathbf{u}_p \tag{6.8}$$

$$\left(n_i \sigma_{ij} n_j \right)_w = \left(n_i \sigma_{ij} n_j \right)_p \tag{6.9}$$

$$\left(\tau_i \sigma_{ij} n_j \right)_w = \left(\tau_i \sigma_{ij} n_j \right)_p \tag{6.10}$$

In which the subscript "*w*" denotes the physical variable in the water region, while the subscript "*p*" denotes the physical variable in the porous flow region. σ_{ij} are the

stress tensors, and τ_i and n_j denote the tangential and normal unit vectors to the interface.

These interface boundary conditions was simplified into a two-dimensional form by Huang et al. (2003) in simulating a solitary wave propagating over a submerged porous breakwater. In order to implement the two-dimensional boundary condition, an imaginary grid line was placed at the interfaces between the porous medium and outside flow region (Shao, 2010) at each time step. The computation of each flow region at both side of the interface was carried out separately. When computing the pure flow zone, the interface boundary information on the boundary grid was given by flow inside of the porous media. Then the interface boundary information of the porous media was given by flow outside of the porous to computing the porous flow motion. This process is repeated at each computational time step until the end of the computation. Unfortunately this method is complicated to use and also not entirely consistent with the Lagrangian nature of the SPH method as pointed out by Akbari and Namin (2013), because particles in SPH carry a specified mass to move continuously between porous region and pure fluid region and consequently the calculated density of each particle changes during the computation (Akbari and Namin, 2013).

Considering that the porous interface is actually a not a sharp line but a transitional zone, Akbari and Namin (2013) proposed a new boundary treatment method by introducing a finer background mesh with porosity information not only in the porous region but also in the pure fluid region. Though more detail porosity information can be obtained for computation near the interface, Akbari and Namin (2013) failed to consider the effect of the differences in the particle spacing and the influence zone of kernel function at the interface region on the predictions.

All above mentioned interface treatment methods did not solve the interface problem completely and are also rather too difficult to implement or too complex to understand. Herein a simple and effective interface treatment method will be proposed for the ISPH application for wave interaction with porous structures. Instead of an imaginary grid line, an interface zone is placed between the porous region and the pure flow region with the interface line being the central line as

shown in Figure 6.1. Therefore, two equal parts distribute at both sides of the interface (the fluid part and the porous part with each width = $2D_0$, total width = $4D_0$) where D_0 is the distance between particles.

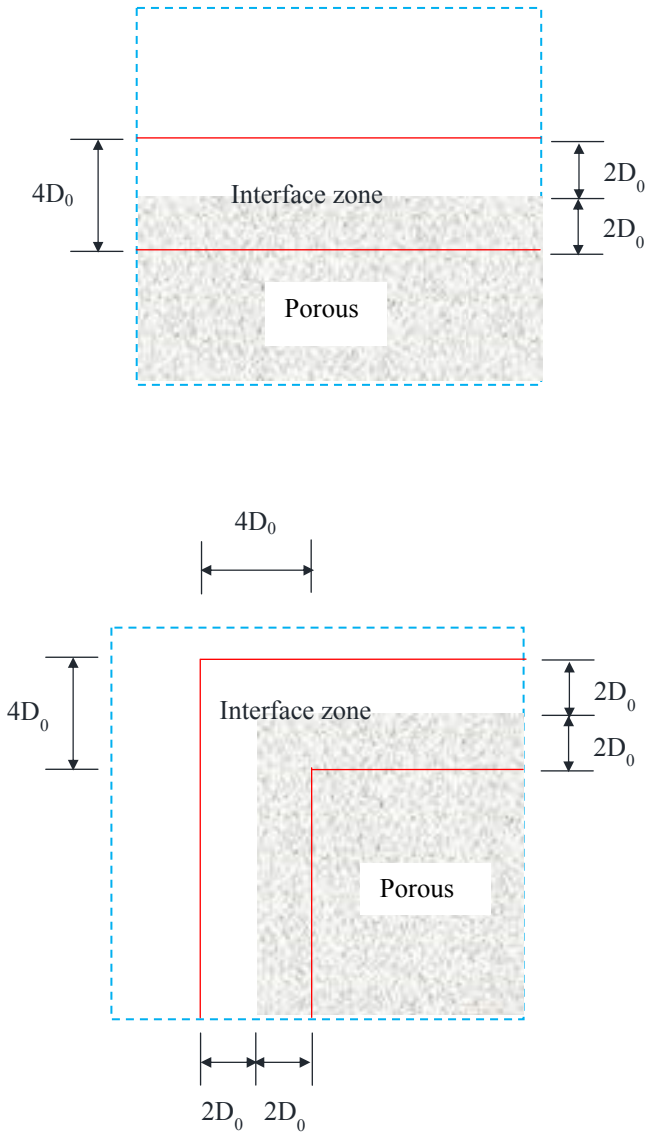

Figure 6.1. Schematic diagram of interface zone along the interface between porous flow region and pure flow region, space between the red lines are the interface zone

At each computational time, the pressures of particles on the interface zone are averaged by the cubic-spline kernel function after solving the Poisson pressure equation. In this calculation only the neighbouring particles in the interface zone are included in the summation. Meanwhile, the interfacial boundary condition can meet the continuity of normal and tangential stresses automatically due to the particle velocity being the apparent velocity in the governing equations (Ren et al., 2014). Subsequently, the velocity and position are updated using the revised velocity obtained by considering flow exchange at the interface. With this treatment, a continuous and smooth normal velocity field and pressure field can be achieved in the vicinity of the interface between the outside flow and the porous flow.

A similar way for interface treatment was used by Ren et al. (2014) to simulate the wave interaction with porous structures in SPH, within which an imaginary transition zone was set along the interface and the width of the transition zone was related to the smoothing length of the SPH kernel approximation. Since the tangential velocity is not continuous at the porous interface it is physically unrealistic to average out the particle velocity difference as proposed by Ren (2014).

6.5 Case I: Wave attenuation over porous bed

The accuracy of the new SPH model for porous structures was firstly verified by comparing the numerical results of wave damping over porous bed with the theoretical solution of Packwood and Peregrine (1980). After the model is verified the model was used to investigate the features of flow field around and inside of a submerged porous breakwater.

6.5.1 Description of numerical modelling

In this section, the proposed SPH porous model is examined for accuracy in predicting the amplitude attenuation of a solitary wave propagating over a rigid porous bed. The theoretical results of Packwood and Peregrine (1980) is used for comparison.

A schematic diagram of modelling set up is showed in in Figure 6.2. The computation zone includes both the water region and porous region. Solitary wave was generated at the left side of the numerical wave flume with the initial wave height H_i. The still water depth is h_0, and the depth of the porous bed is h_p with a porosity n_w and intrinsic permeability K_p. The flow was simulated by solving equation (6.1) and equation (6.2), equation (6.3) and (6.4) together. As showed in Figure 6.2, the intersection of the left boundary and the wave flume bottom was defined as (x, y) = (0, 0). The wave tank was 46.0m long and 0.52m high. The left side of the porous bed is 3.0m away from coordinate origin of the computation domain. The bottom is solid boundary.

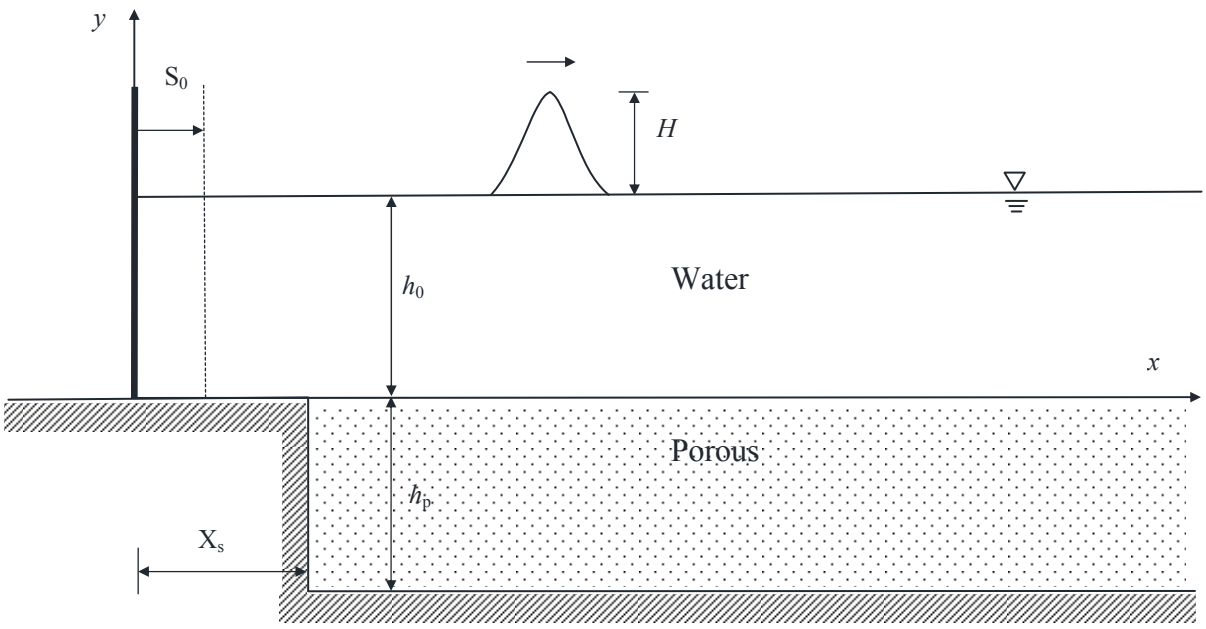

Figure 6.2. Schematic diagram of a solitary wave propagating over a rigid porous bed

6.5.2 Comparisons of wave height attenuation

Figure 6.3 compares the computed and theoretical wave heights and it provides two types of results, wave height ratio of SPH without and with the interface treatment is implemented. Packwood and Peregrine (1980) gave the theoretical wave height damping function of solitary wave propagating over a permeable bed with finite fixed depth as

$$H = \frac{H_i}{1 + C_s \left(H_i / h_0 \right) \left(x / h_0 \right)} \tag{6.11}$$

where x is the distance travelled by the solitary wave;

$$C_s = 0.4 \left(K_h / C_0 \right) \left(h_p / h_0 \right) \tag{6.12}$$

$$C_0 = \sqrt{g h_0} \left(1 + H_i / 2 h_0 \right) \tag{6.13}$$

And K_h represents the hydraulic conductivity of the porous media and can be expressed as

$$K_h = K_p g / \upsilon \tag{6.14}$$

Here υ is the kinematic viscosity of the fluid.

Specific parameters used are water depth $h_0 = 0.4\text{m}$, the ratio between depth of porous bed and depth of still water $h_p / h_0 = 1.0$, the porosity of the porous bed $n_w = 0.39$ and the solitary wave height $H_i = 0.11\text{m}$. The diameter of porous materials is $d_{50} = 0.55\text{cm}$ so the intrinsic permeability coefficient is $K_p = 0.102 \times 10^{-7}\,\text{m}^2$ according to equation (6.5), and the nonlinear resistance force coefficient is $C_f = 0.51$ as calculated by equation (6.6). The particle spacing is 0.04m in the simulation and about 24 thousands of particles in total are simulated.

As shown in Figure 6.3 the green line with circle represents the theoretical wave attenuation ratio with the increase of the distance. Besides, the red line with square denotes the SPH results with pressure average treatment near interface and

the blue line with triangular denotes the SPH numerical results without the treatment. First, Figure 6.3 indicates the attenuation of the wave height ratio H/H_i decreases to 0.672 at the distance of 36m under this small degree of permeability. Porous bed can cause large wave energy dissipation by the percolation of flow and friction of porous solid structure. Second, Figure 6.3 reveals that both the SPH wave height attenuations fit well with the theoretical values but the results with pressure average fits seem to fit the theoretical predictions better than that without pressure average.

As to the discrepancies between the numerical and theoretical results, this may be caused by the numerical errors in the free surface detection due to some particle splashing out the free surface. And the post-process code maybe not good enough to calculate the wave height at fixed point. This can be the reason for fluctuation of numerical results. The reason for the numerical results being generally lower than the theoretic results could also be due to energy dissipation caused by the friction in the boundary layers in both pure fluid bed and porous bed (Huang et al., 2008).

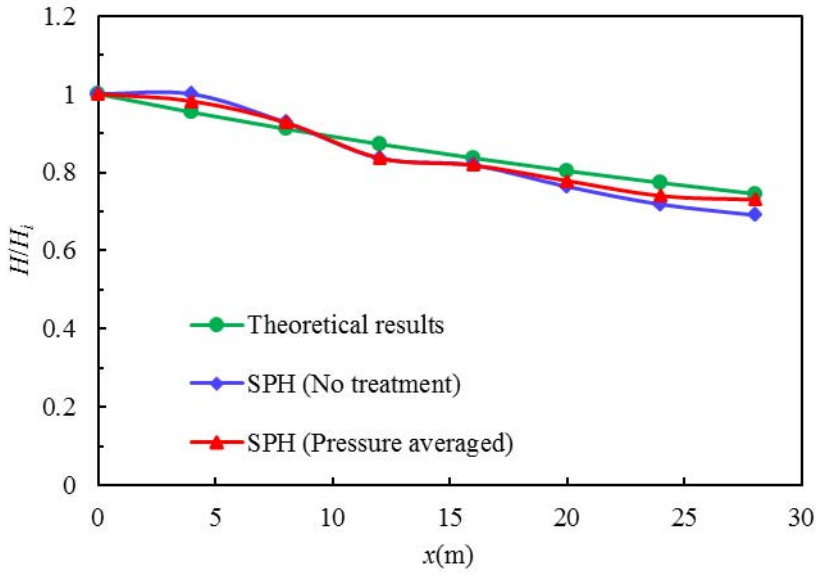

Figure 6.3. Comparison of the SPH numerical and theoretical wave heights for a solitary wave propagating over a porous bed

6.5.3 Pressures at the two sides of the interface

In order to further test the interface treatment, a best and straightforward way is to check the pressures continuity at the interface by comparing the pressure at the same points of the interface but calculated from each side of the flow zone.

Table 6-1 presents the coordinates of the six pressure measurement points that are three pairs of pressure measurement points P1 and P2, P3 and p4, P5 and P6. Each pair of points has the same x coordinate and a very tiny difference in y coordinates so as can be safely considered to be located at the same position. y= 0.001m means that the location is in the pure water area, while y= - 0.001m means that the location is in the porous area. So P1, P3 and P5 are in the water region and P2, P4 and P6 are in the porous media region, respectively.

Table 6-1. The coordinates of the pressure measurement points

Measurement points	P1	P2	P3	P4	P5	P6
x(m)	10		15		20	
y(m)	0.001	-0.001	0.001	-0.001	0.001	-0.001

Figure 6.4 shows time history of dynamic pressure at different measurement points. As we can see, the pressure curve of each pair of pressure points matches each other (P1 and P2, P3 and P4, P5 and P6) perfectly from the beginning of the time till end, including all the peak value and even pressure fluctuation. The pressure comparison demonstrates that the SPH model can predict the pressure of porous flow by averaging pressure using kernel function at interface zone.

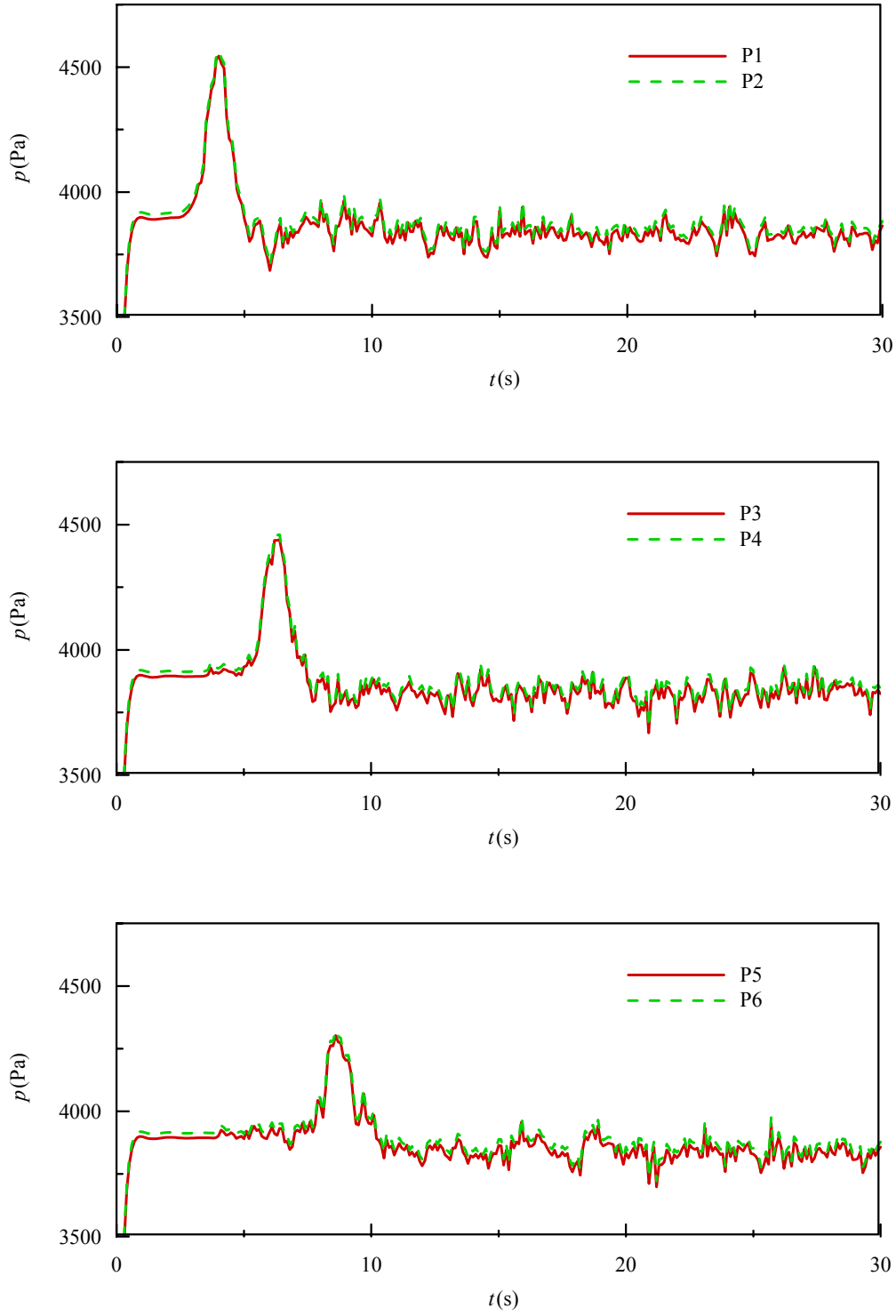

Figure 6.4. Time series of dynamic pressure at different measurement points

6.6 Case II: Wave interaction with porous breakwater

6.6.1 Description of numerical modelling

A numerical simulation was carried out to reproduce the experiment of Wu and Hsiao (2013) by using the proposed SPH model. The physical experiment was conducted in a 2D narrow wave flume that was 25 m long, 0.5 m wide, and 0.6 m high. As shown in Figure 6.5, the left side of the flume was equipped with a piston-type wave-maker to generate the solitary wave and a gravel beach was installed on the right side of the flume to dissipate wave energy and reduce wave reflection (Wu and Hsiao, 2013). The bottom is solid boundary and the right side of the computational domain is absorbing boundary. A permeable cuboid structure was mounted on the bottom in the middle of the wave flume. The structure which was composed of uniform-sized spheres with a constant diameter d_{50} of 1.5 cm was 13 cm long, 6.5 cm height and 50 cm wide with a porosity value of 0.52. As shown in Figure 6.5, two capacitance-type wave gauges were located in front of (x = −1.8 m, WG1) and behind (x = +1.8 m, WG2) the porous breakwater to record the free surface elevation time histories. The velocity field was measured by a particle image velocimetry (PIV) in the vicinity of the permeable breakwater with 30 times of repetition for providing ensemble-averaged mean values. The constant water depth is 0.106m, with the wave-height-to water- depth ratio of 0.45. More detail about the experiment can be found in Wu and Hsiao (2013).

The numerical computation zone was arranged according to the physical experiment. Because the porous breakwater fully occupied the wave flume in the lateral direction in experiment, this physical experiment can be regarded as 2D in macroscopic scale. Wu et al. (2014) also stated that the submerged porous medium can be seen as a 2D spatially averaged porous structure on the macroscopic scale and reproduce the experiment by using 2D VARANS modelling. As shown in Figure 6.5, the intersection of the weather side of the porous breakwater and flume bottom was defined as (x, z) = (0, 0). The wave tank was 8.0m long and 0.2m high, with a porous

region in the middle of the wave tank. The weather side of the breakwater is 4.0m away from the left side of the computation domain.

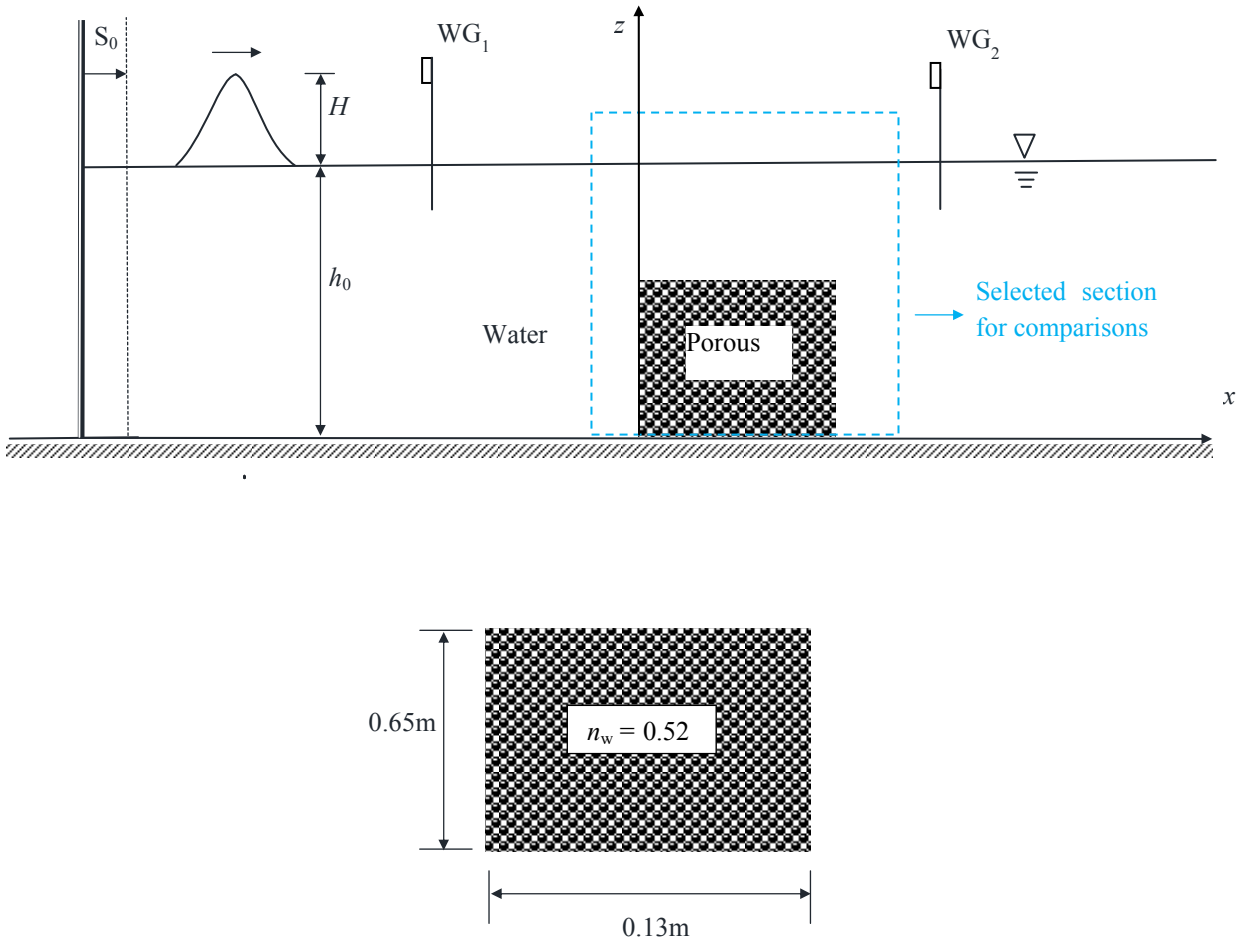

Figure 6.5. Schematic diagram of a solitary wave propagating over submerged porous breakwater

The solitary wave was generated by the method described in section 3.6. Since the length of the computation domain is shorter than that in the physical experiment wave flume (25m), instead of given the required wave height 0.477m, the incident wave height was determined by matching the measured wave height at reference wave gauge WG_1 to the experimentally measured wave height through

trying different wave height repeatedly at the start point of the numerical flume. The downstream boundary was designed according to the boundary treatment described in section 3.6 to prevent wave reflection. The bottom of the wave tank was treated as non-slip boundary.

The particle spacing is 0.005m, with about 36 thousands particles in total in the simulation. The particle spacing in the porous region is the same as the particle spacing in water area. This setup can ensure computational efficiency and accuracy. Only about 3.5 hours was needed for the simulation time 8s with a computer of 3.33GHz.

6.6.2 Comparisons between model results and experiment data

Figure 6.6 shows the comparison of free surface elevation time series between present the SPH model results and experiment results of Wu and Hsiao (2013). The wave curve at reference point x = -1.8m fits fairly well with the experiment measurement, especially the incident wave as shown in Figure 6.6 (a). This means the incident wave generated numerically is a close representation of that in the laboratory. The incident wave was reflected partially by the submerged porous breakwater after 4s. The reflected wave propagated at the opposite direction toward the wave gauge point x = -1.8m, resulting in a waveform similar to sine wave as shown in Figure 6.6 (a). The wave crest and wave trough can be seen clearly from the SPH modelling result with slight fluctuation duo to the particle disturbance error accumulation after being enforced to move by the solitary wave.

Likewise, Figure 6.6 (b) shows the numerical prediction of wave time series at x = 1.8m, which also fits well with the experimental measurements. It is noted that there is a slight overestimation of the wave surface at the wave trough in the numerical results. The reason for this discrepancy may be that the friction caused by the porous structure on the flow is slightly underestimated by the model.

Overall, the free surface elevation results from the SPH model agree well with the experiment. Furthermore, Wu et al. (2014) have verified that the free surface elevation time history didn't have a significant variation in different lateral sections in the 3D model, which further confirm that the 2D SPH model is capable of

predicting the free surface elevation time history for wave interaction with porous structure.

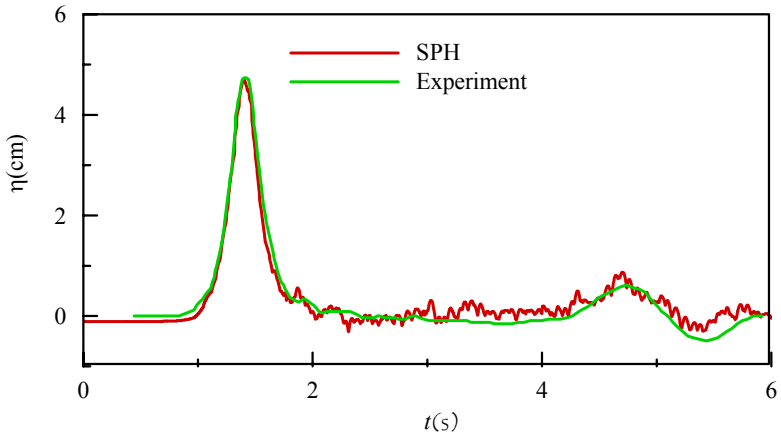

(a) x = -1.8m

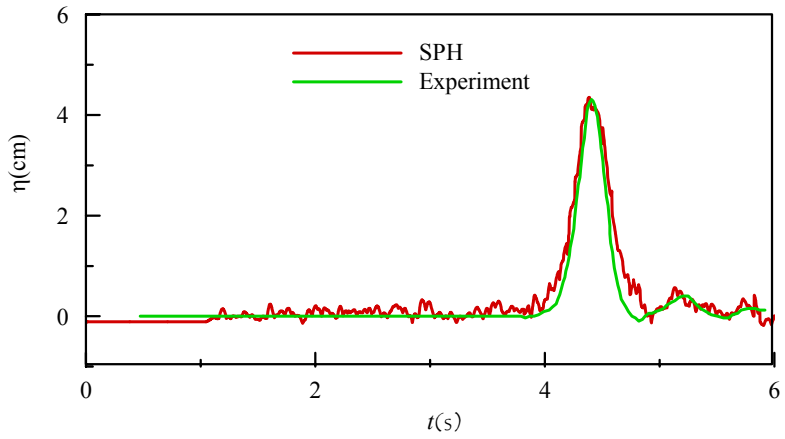

(b) x = 1.8m

Figure 6.6. Comparison of free surface elevation time series between present SPH model results and experiment Wu and Hsiao (2013) at (a) x = -1.8m and (b) x = 1.8m

Figure 6.7 to Figure 6.11 show the comparison of the velocity field between model results (lower) and experiment (upper) at five different instantaneous time t=1.45s, 1.65s, 1.85s, 2.05s and 2.25s. These five representative times were chosen

to show the flow features around the submerged permeable breakwater at five solitary wave evolutionary phases of interest from wave passing by the porous breakwater until leaving it.

As it can be seen from Figure 6.7, the temporal free surface elevations, as well as the flow pattern, are accurately predicted by the model. When the leading wave front approaches the weather side of the permeable breakwater about t=1.45s, inevitably, particles velocity directions were changed due to the impediment of permeable breakwater, resulting in the flow parting at the top of the obstacle and the

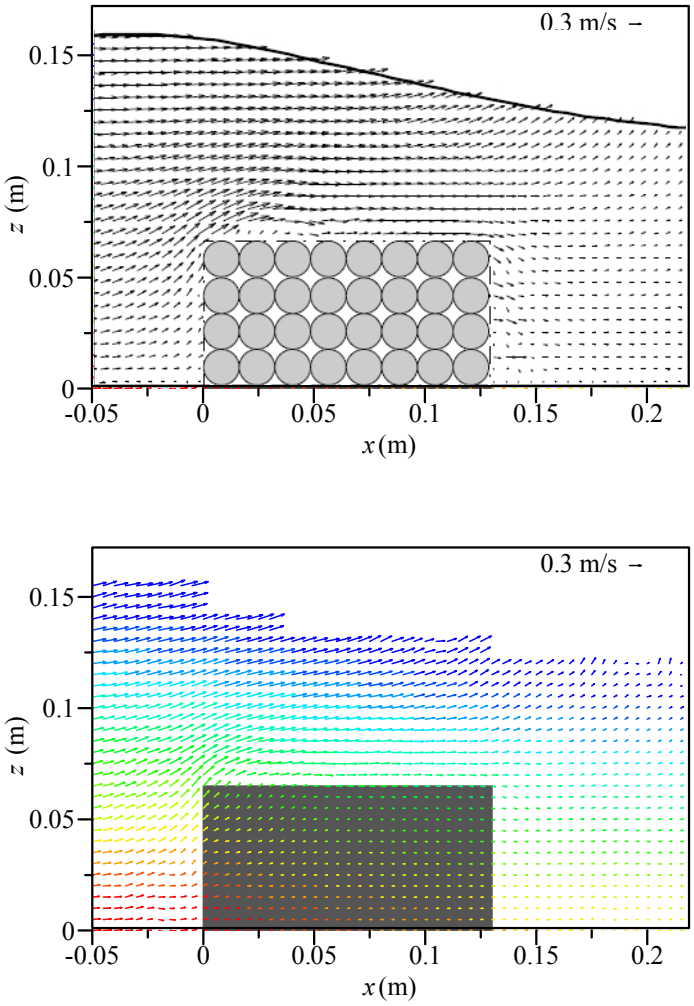

Figure 6.7. Comparison of velocity field between model results (lower) and experiment (upper) at t=1.45s

formation of a small vortex at the upper left face of the structure. Although the velocity is small, the flow is seen to penetrate the permeable breakwater from the lee side to the pure fluid zone.

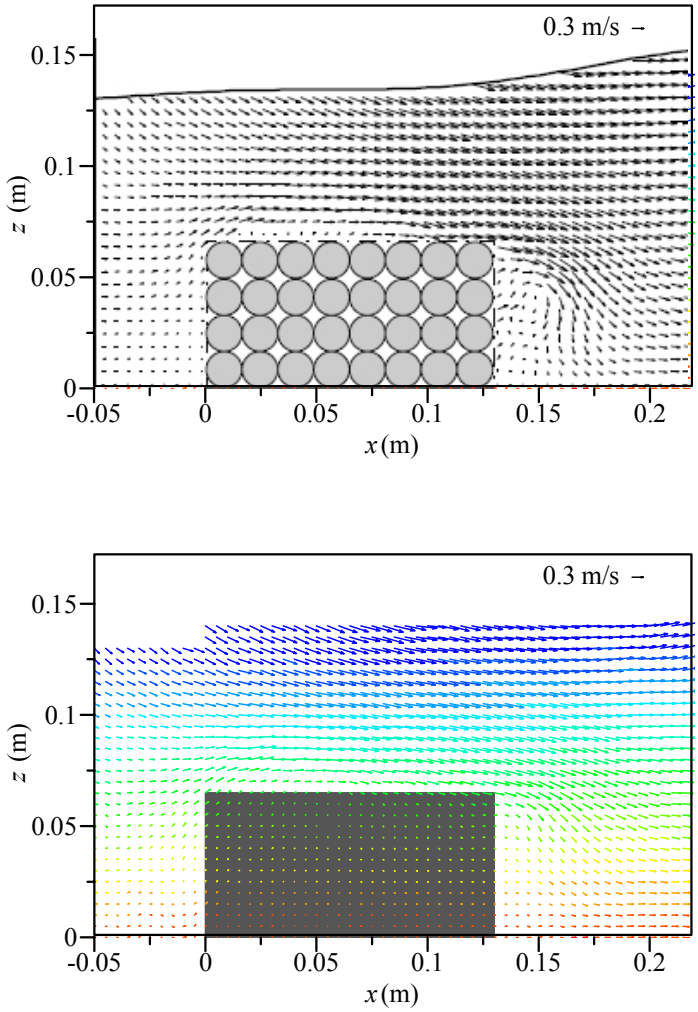

Figure 6.8. Comparison of velocity field between model results (lower) and experiment (upper) at t=1.65s

Additionally, slightly disturbed velocities can be observed on the lee side of the obstacle for experiment measurement from the upper image of Figure 6.7. This is because the breakwater is composed of regularly located spheres with uniform size in experiment and physically the flow can only penetrate through the space between

the spheres, but no flow injection at the spheres face. However, SPH model the porous region was treated as space averaged and macroscopically homogeneous and thus flow particles penetrate the lee face of the permeable breakwater at every point evenly in space and time.

As shown in Figure 6.8 (t=1.65s), the primary clockwise vortex above the upper face of the permeable breakwater is transferring from the weather side to the lee side as the crest of the solitary wave passes over the porous obstacle.

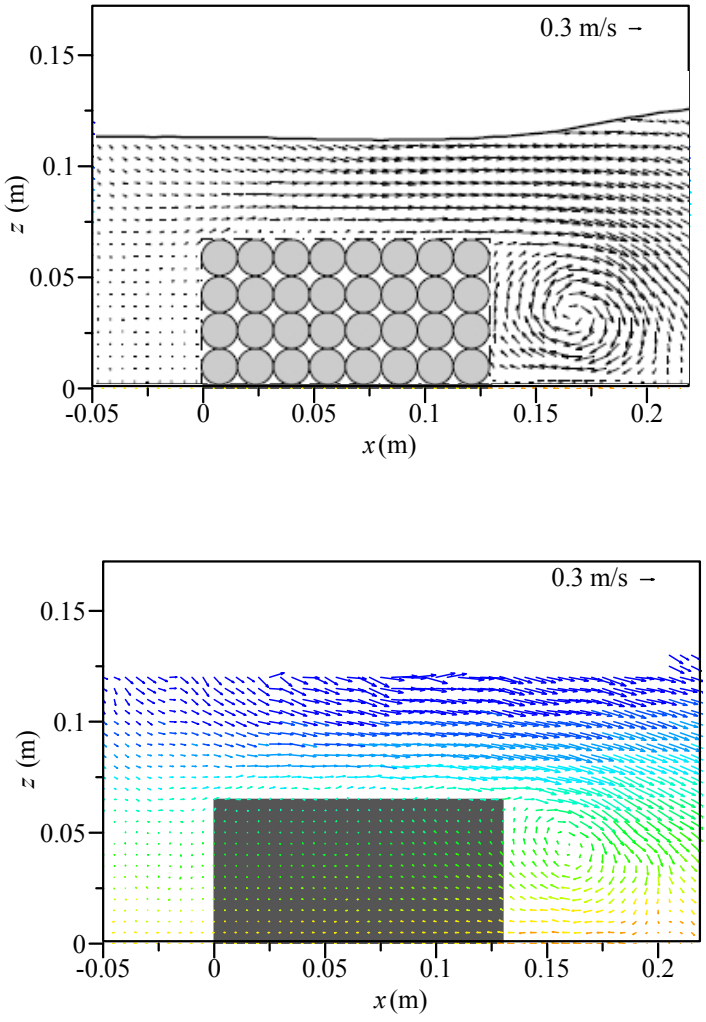

Figure 6.9. Comparison of velocity field between model results (lower) and experiment (upper) at t=1.85s

With the increase in time, this main vortex grows larger and is strengthened by the shear layers due to the flow convection that can be seen from Figure 6.8 (t=1.85s). In addition, it moves further in the wave direction and goes into deeper water.

After that, the main vortex starts to move upward to the free surface as shown in Figure 6.10 (t=2.05s), causing it to bulge slightly near the free surface in experiment, while particles of numerical results splash slightly at the same location. The SPH model simulates the locations of the centroid of the vortex fairly well.

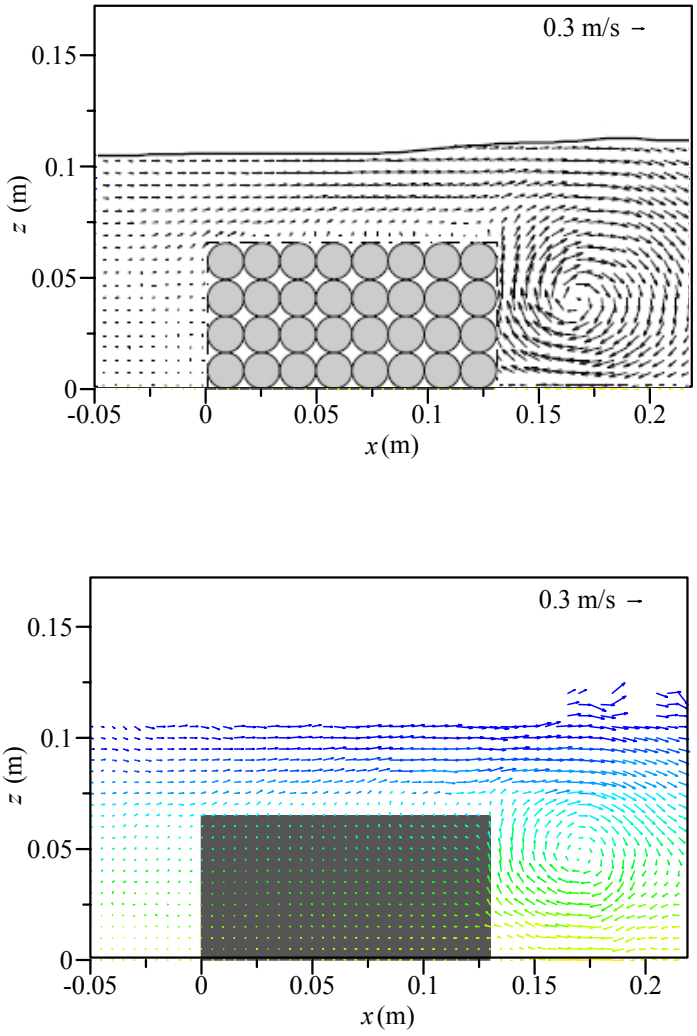

Figure 6.10. Comparison of velocity field between model results (lower) and experiment (upper) at t=2.05s

When the wave has completely passed by the breakwater, the main vortex nearly reaches the free surface as shown in Figure 6.10 (t=2.25s), velocity disturbance occurs at the free surface just head of the vortex.

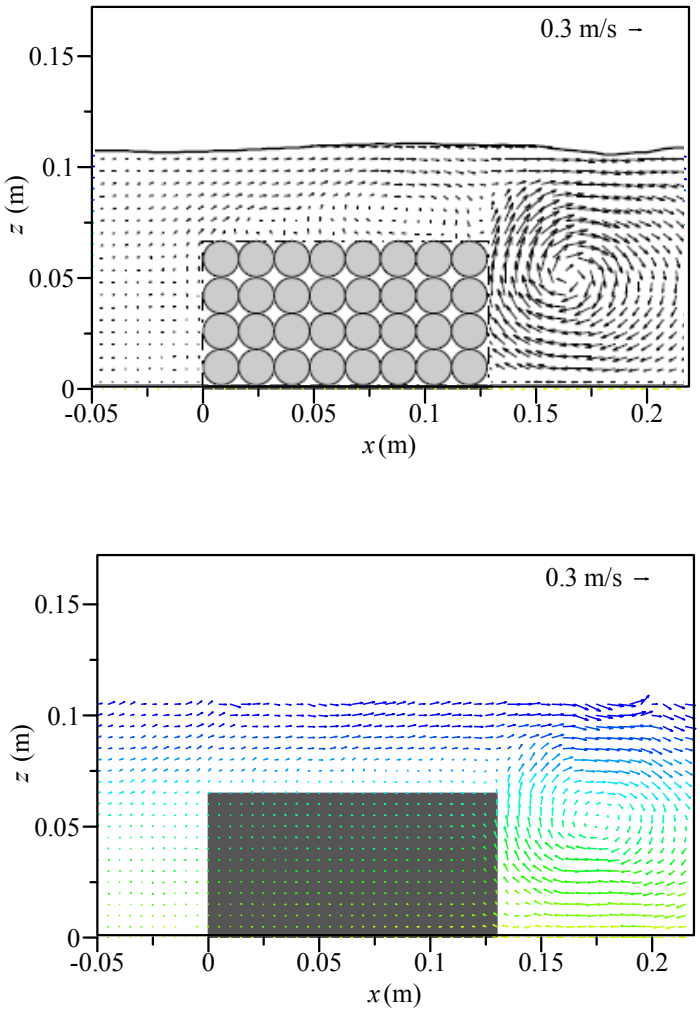

Figure 6.11. Comparison of velocity field between model results (lower) and experiment (upper) at t=2.25s

Figure 6.12 to Figure 6.21 show the velocity profiles at seven different sections in x direction. Table 6-2 presents the coordinates of the seven velocity measurement points. It should be noted that the coordinates of points V6 and V7 are deferent between t=1.45s and other time. The circle denotes the experiment velocity;

the red solid line denotes horizontal velocity distribution along the y direction for the SPH results, while green solid line denotes vertical velocity distribution along the *z* direction for the SPH results.

Table 6-2. The coordinates of the velocity measurement points

Measurement points		V1	V2	V3	V4	V5	V6	V7
x(m)	*t*=1.45s	-0.004	0.00	0.04	0.08	0.12	0.14	0.16
	t=other	-0.004	0.00	0.04	0.08	0.12	0.16	0.20

The measured and modelled results are generally in good agreement, as shown in Figure 6.12 to Figure 6.21, especially the vertical velocity distribution. The slight differences exist for the calculated horizontal velocity distribution near the interface of between the pure fluid area and porous flow area. As the leading wave front of the solitary wave approaches the weather side of the breakwater, the experiment results show a small horizontal velocity perturbation on the lee side of the obstacle at x = 0.14m whereas the SPH results show uniform velocities as shown in Figure 6.12 and Figure 6.13. This feature is consistent with the velocity field shown in Figure 6.6, and the reason has been given in above text. So the flow was clearly affected by the local geometry of breakwater and thus the results may be dependent on the x coordinate of the measurement sections.

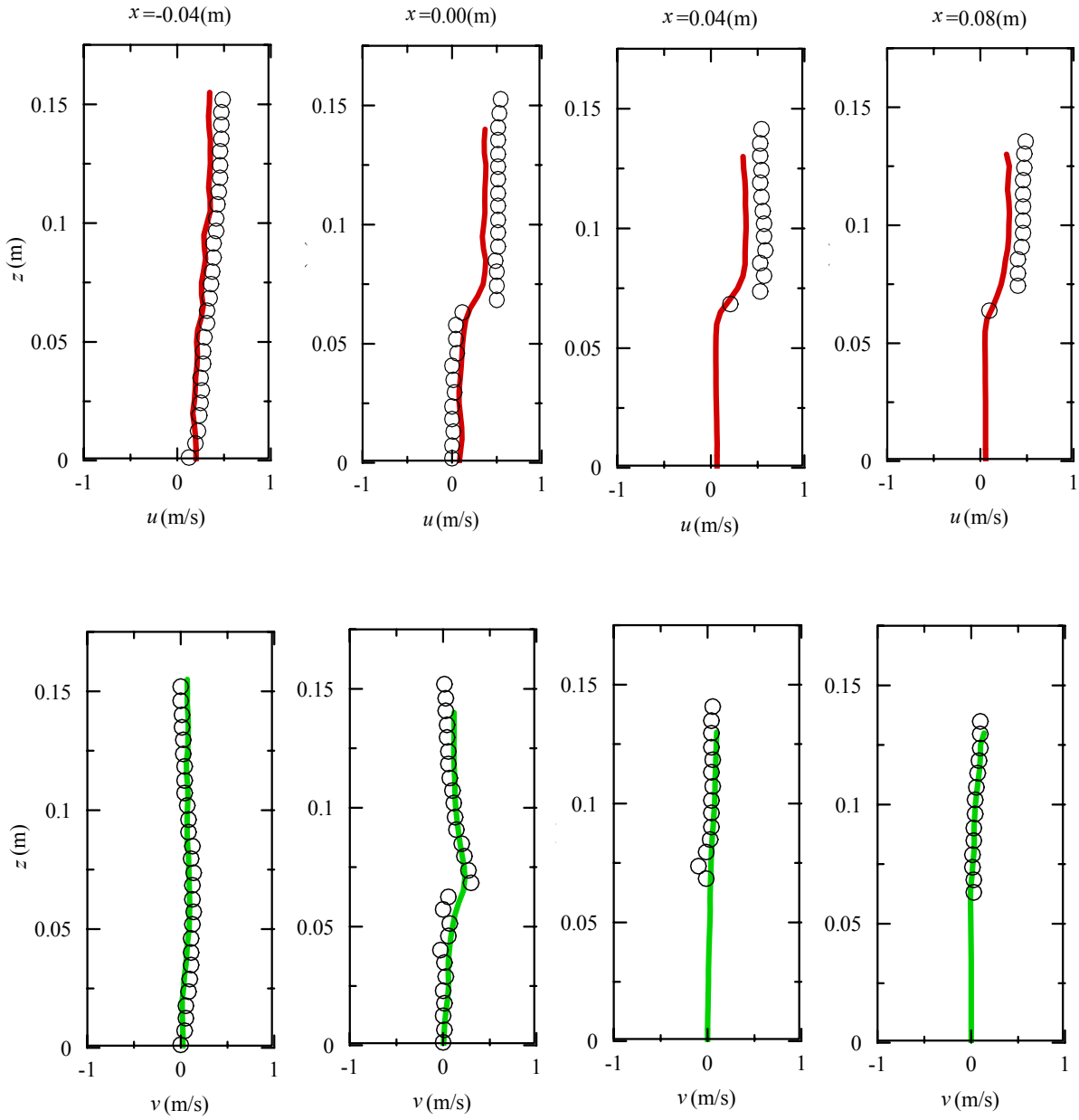

Figure 6.12. Horizontal and vertical velocity profiles comparison between model results and experiment at t=1.45s, Circle: experiment; solid line: SPH results (red: horizontal velocity, green: vertical velocity)

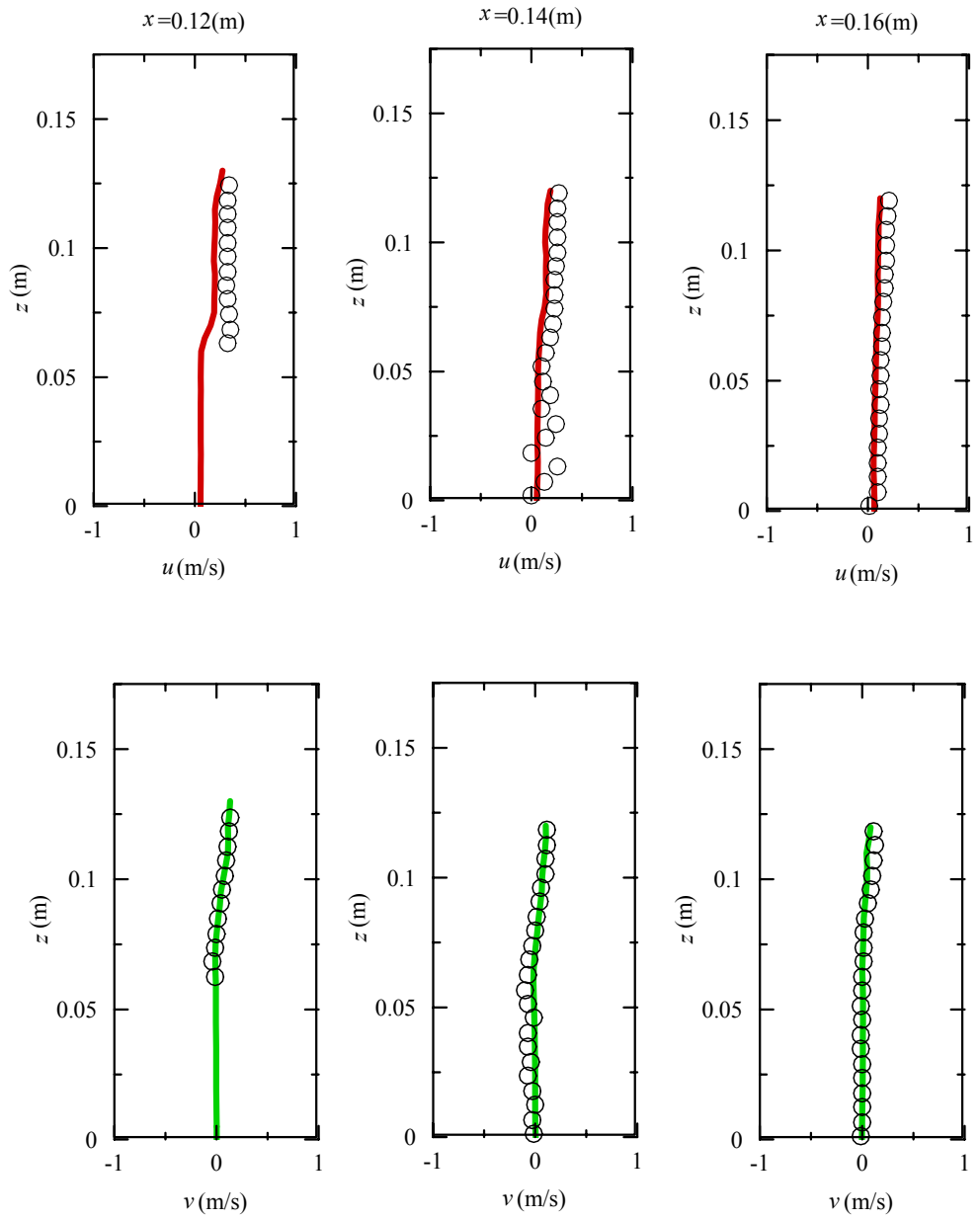

Figure 6.13. Horizontal and vertical velocity profiles comparison between model results and experiment at t=1.45s, Circle: experiment; solid line: SPH results (red: horizontal velocity, green: vertical velocity)

The slight velocity differences shown in Figure 6.13 at x = 0.14m are in the initial stage of the formation of the primary vortex. As the solitary wave propagates towards the lee edge of the obstacle, the velocity difference between the measured and calculated results changes its position to cross-section of velocity x = 0.16m in

Figure 6.14 and Figure 6.15. Moreover, the differences appear both in horizontal and vertical velocity profiles x = 0.16m.

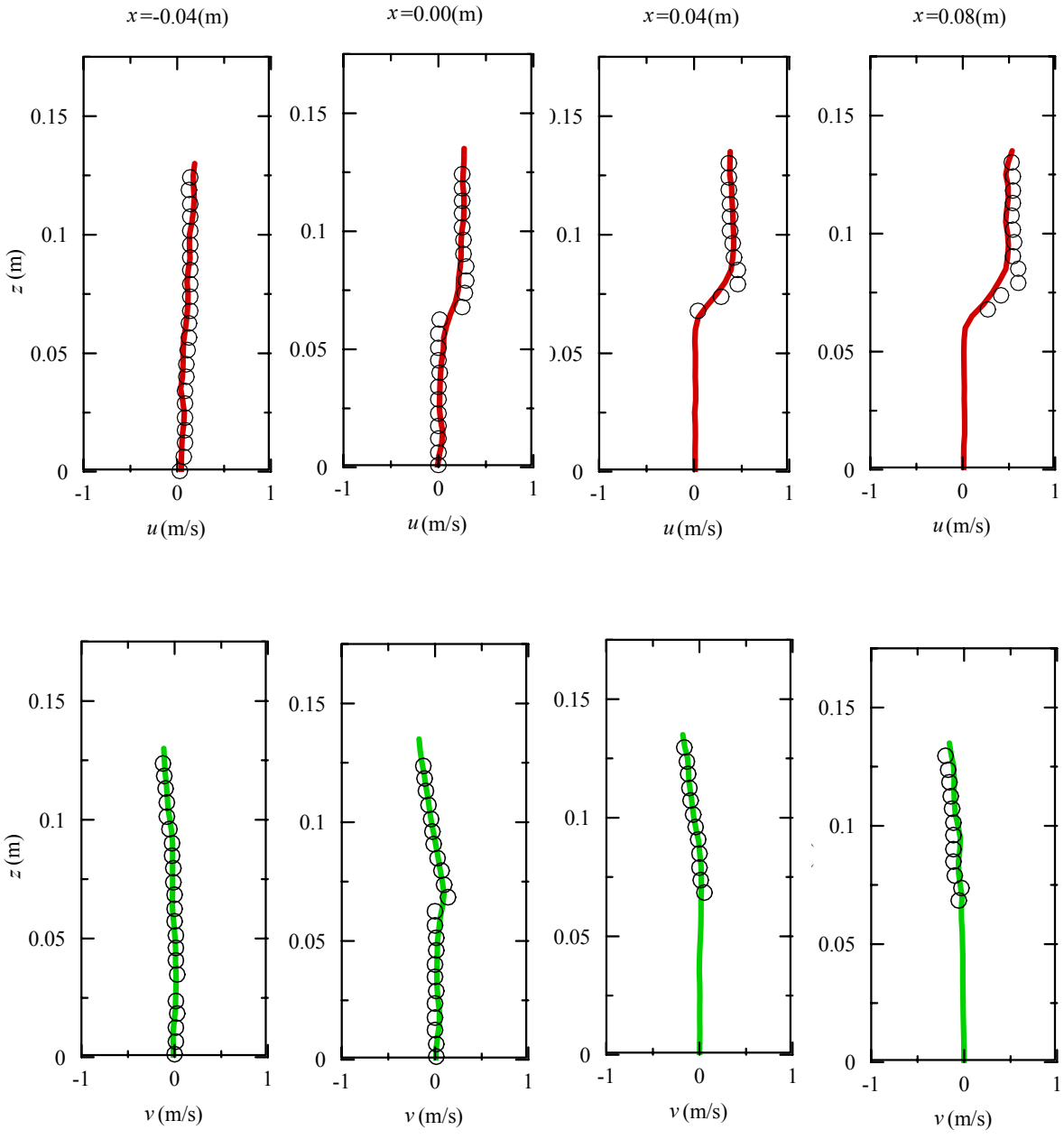

Figure 6.14. Horizontal and vertical velocity profiles comparison between model results and experiment at t=1.65s, Circle: experiment; solid line: SPH results (red: horizontal velocity, green: vertical velocity)

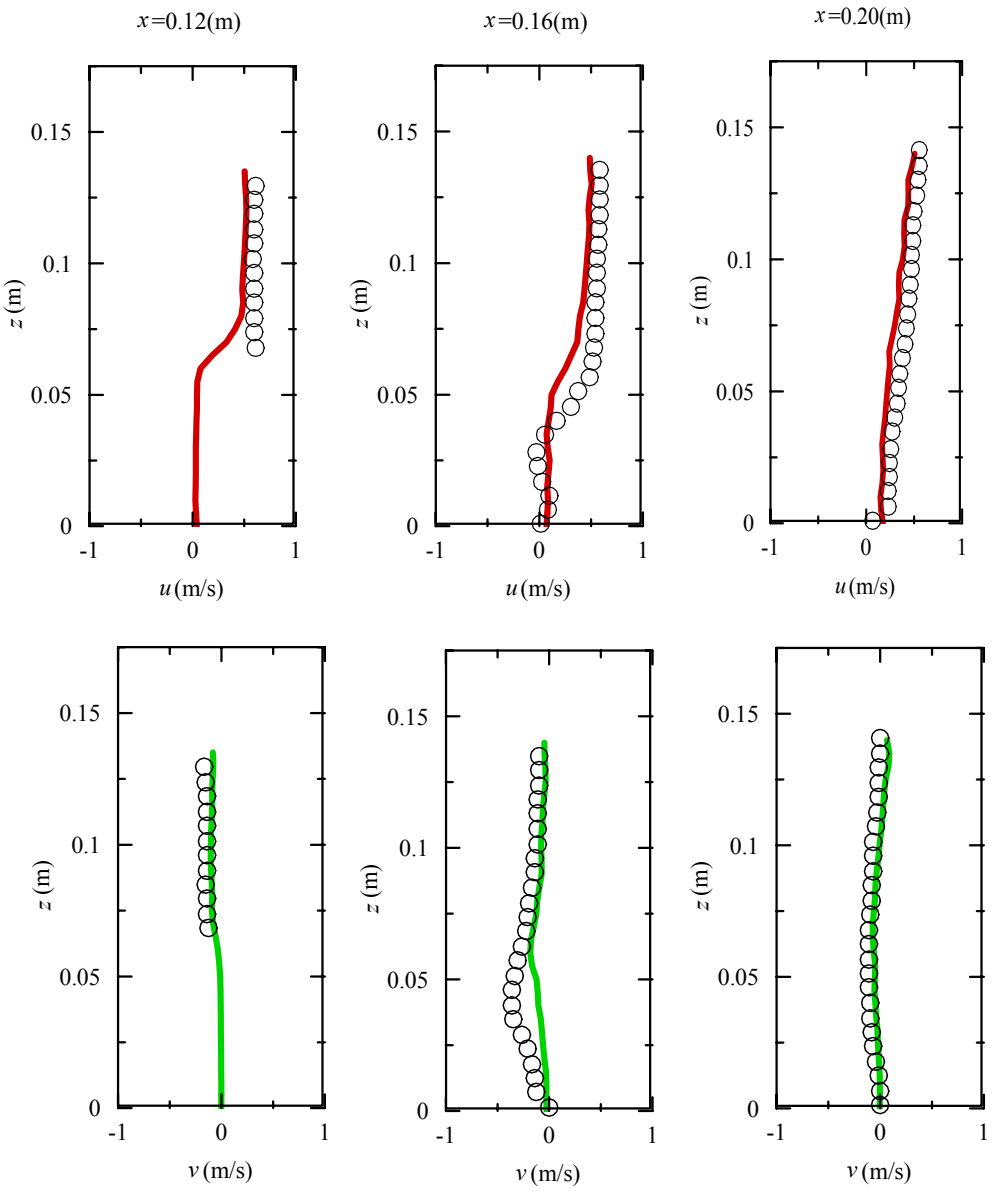

Figure 6.15. Horizontal and vertical velocity profiles comparison between model results and experiment at t=1.65s, Circle: experiment; solid line: SPH results (red: horizontal velocity, green: vertical velocity)

With the increase of time, the horizontal velocity difference is slightly enlarged between the simulation and the experiment. As shown in Figure 6.16 to

Figure 6.21 the horizontal velocity difference continues to exist from t = 1.85 s to 2.25 s, whereas the vertical velocity difference moves onward and a slight difference exists at both x = 0.16m and x = 0.20m from Figure 6.16 and Figure 6.17.

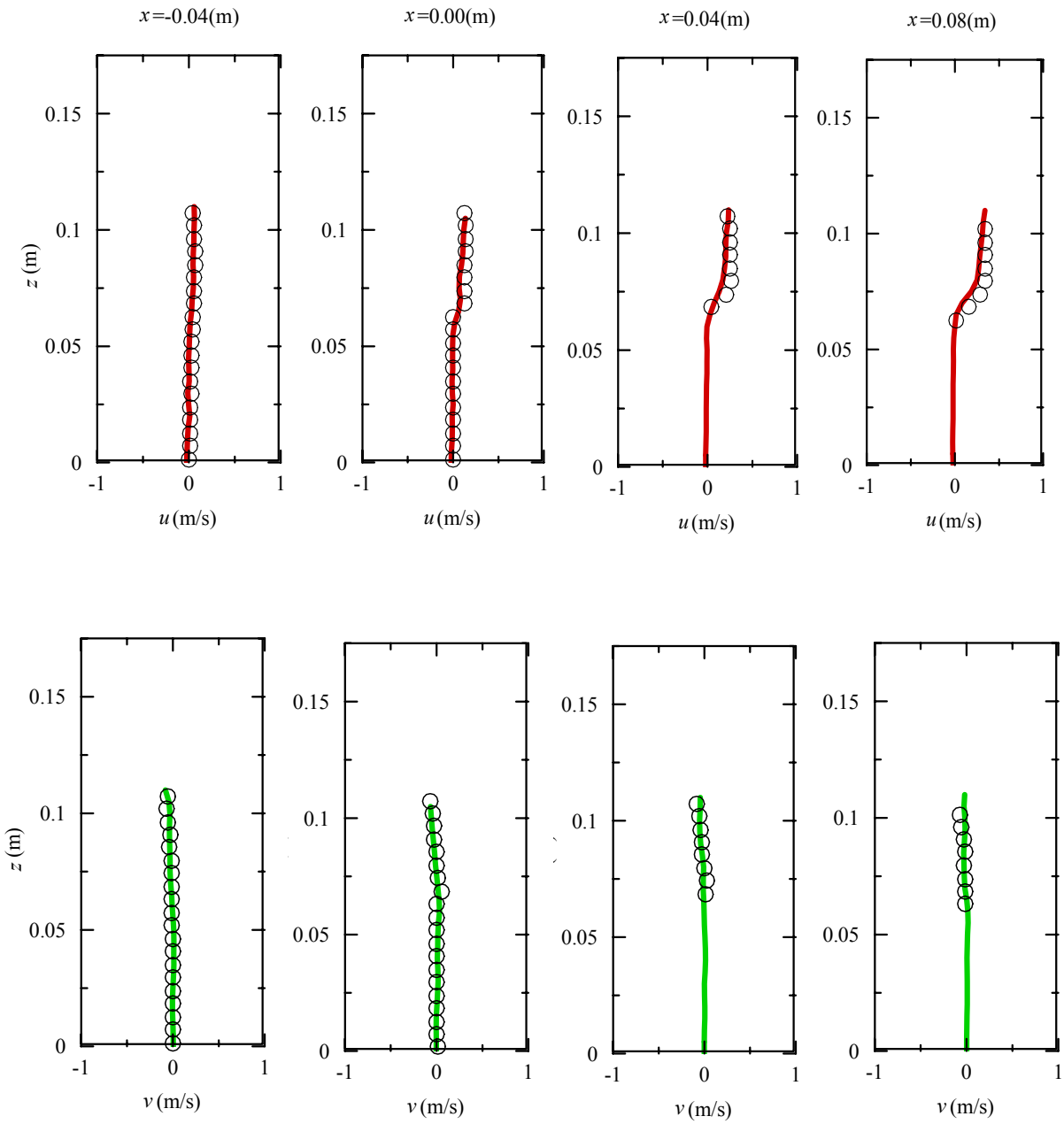

Figure 6.16. Horizontal and vertical velocity profiles comparison between model results and experiment at t=1.85s, Circle: experiment; solid line: SPH results (red: horizontal velocity, green: vertical velocity)

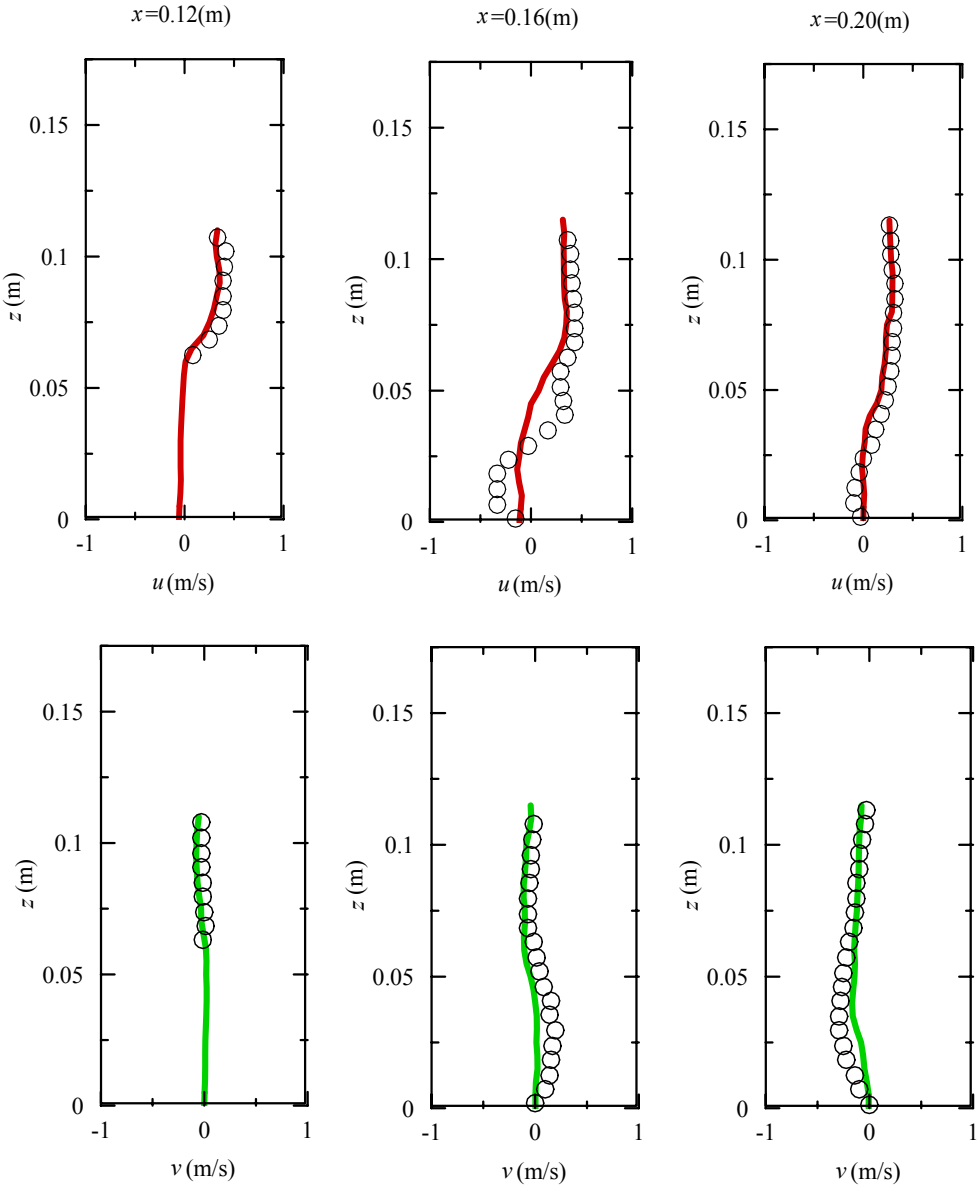

Figure 6.17. Horizontal and vertical velocity profiles comparison between model results and experiment at t=1.85s, Circle: experiment; solid line: SPH results (red: horizontal velocity, green: vertical velocity)

The fact that the vertical velocity has a good agreement between the simulation and the experiment at x = 0.16m as shown in Figure 6.19 and Figure 6.21. This indicated that the model can well predict the vertical profiles of at most of the sections. As the interface located at z = 0.65m in the computation domain, all the velocity profiles from Figure 6.12 to Figure 6.21 clearly demonstrate that the SPH

model can reproduce the large horizontal velocity changes at the important areas of the interface in both magnitude and direction.

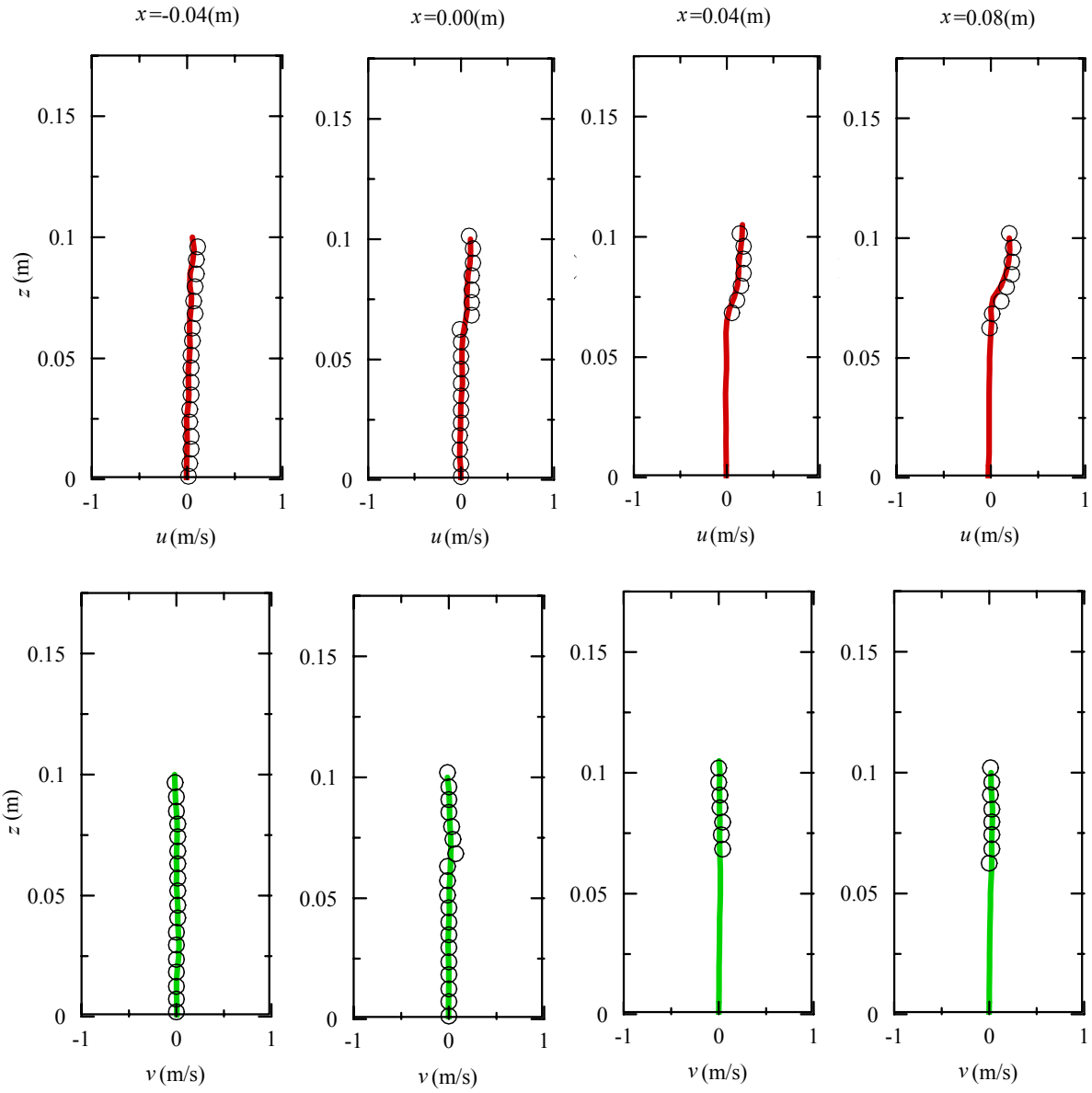

Figure 6.18. Horizontal and vertical velocity profiles comparison between model results and experiment at t=2.05s, Circle: experiment; solid line: SPH results (red: horizontal velocity, green: vertical velocity)

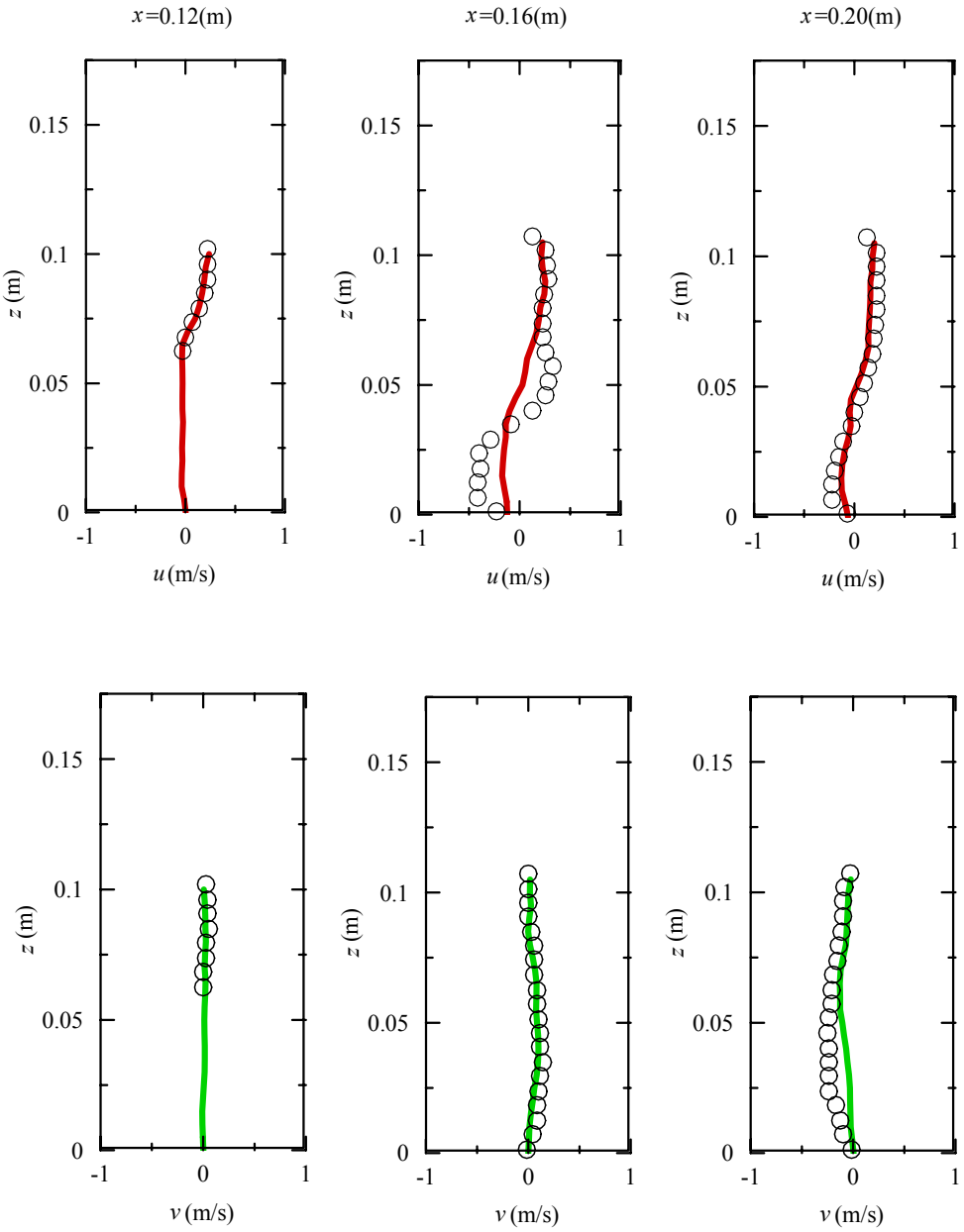

Figure 6.19. Horizontal and vertical velocity profiles comparison between model results and experiment at t=2.05s, Circle: experiment; solid line: SPH results (red: horizontal velocity, green: vertical velocity)

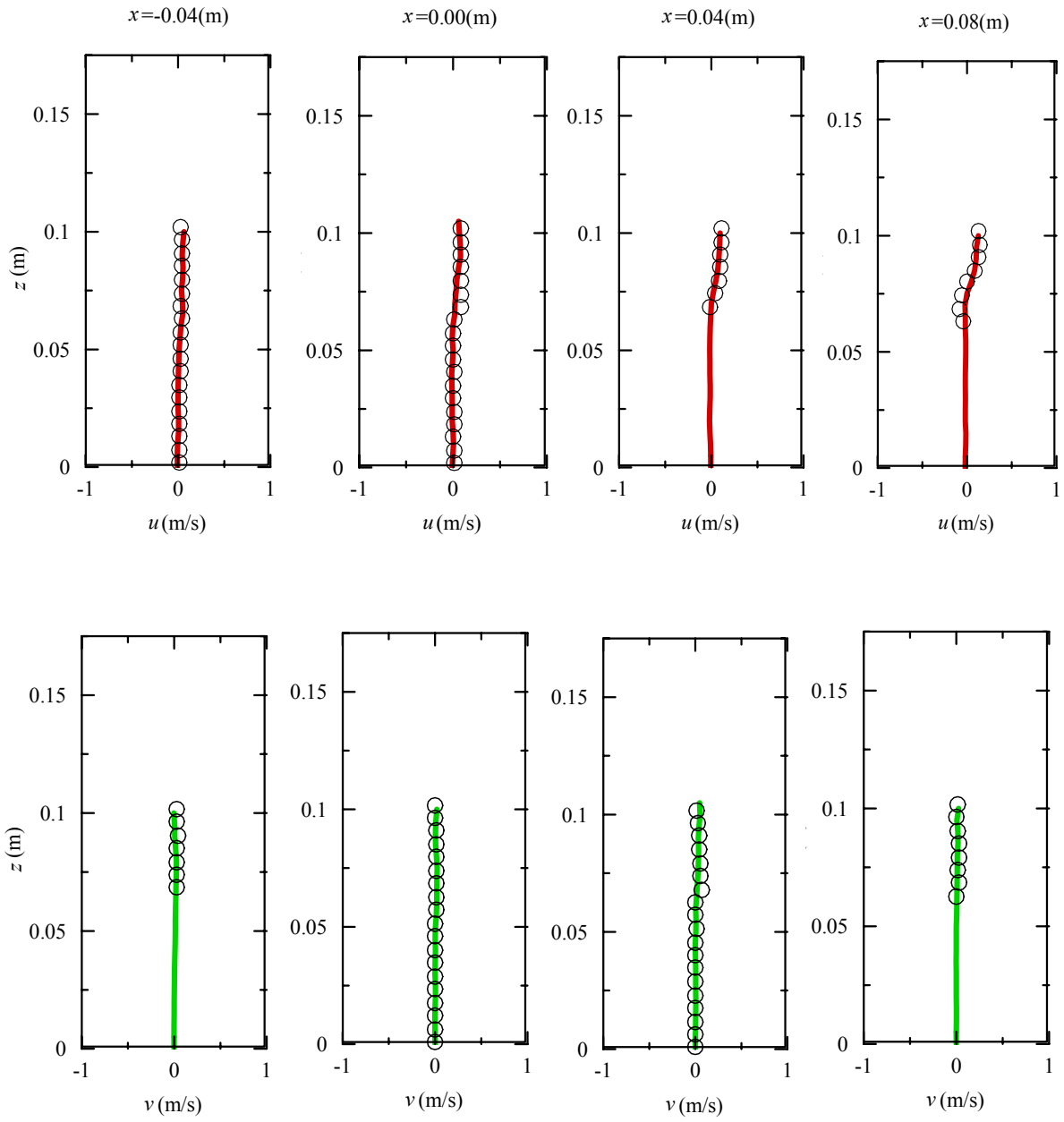

Figure 6.20. Horizontal and vertical velocity profiles comparison between model results and experiment at t=2.25s, Circle: experiment; solid line: SPH results (red: horizontal velocity, green: vertical velocity)

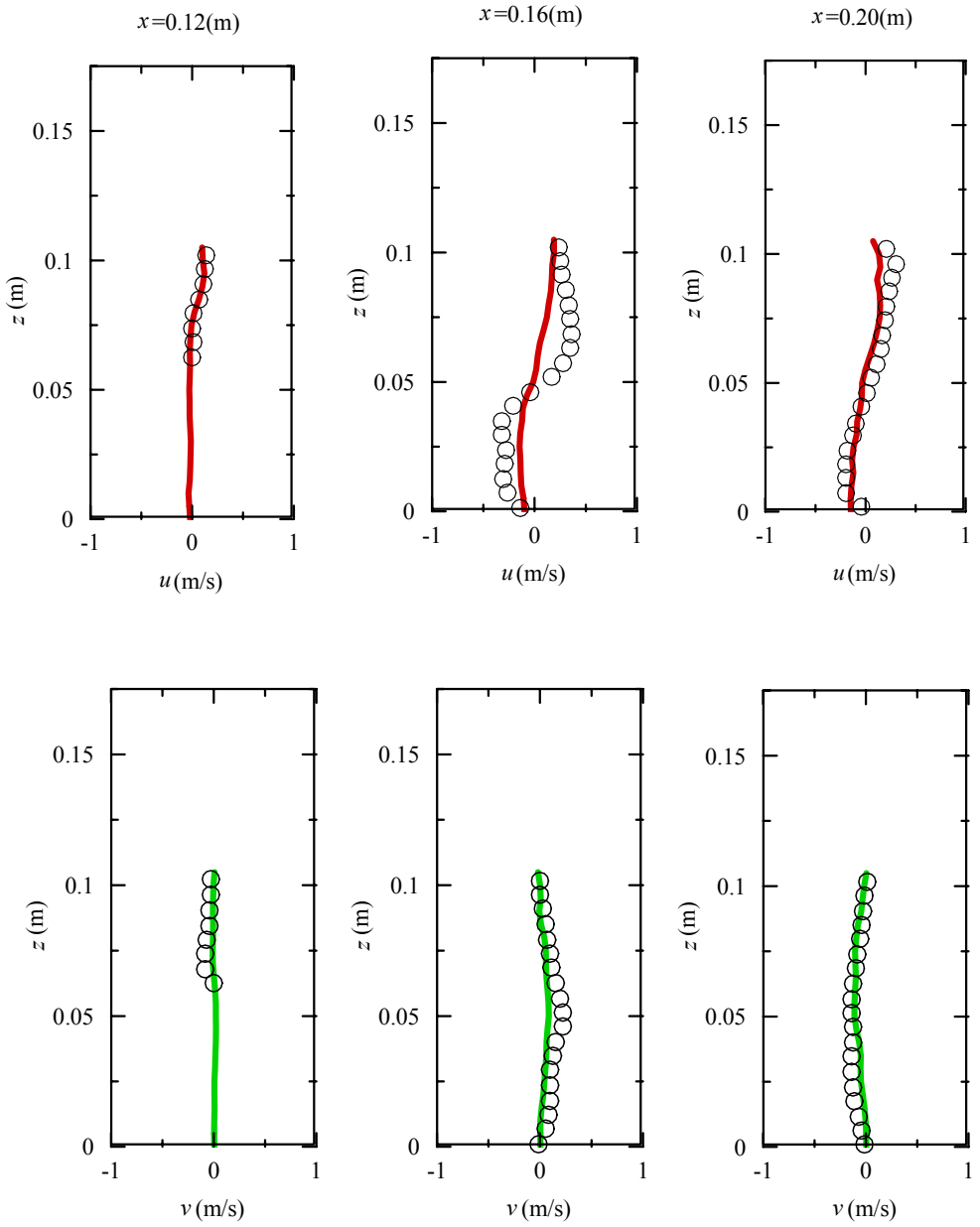

Figure 6.21. Horizontal and vertical velocity profiles comparison between model results and experiment at t=2.25s, Circle: experiment; solid line: SPH results (red: horizontal velocity, green: vertical velocity)

6.7 Summary

The SPH model was extended for investigating the wave interaction with porous structure to explore the flow motion inside and in the vicinity of the porous structure. After a comprehensive analysis of the Navier-Stokes equations for flow outside porous and the Navier-Stokes type equation for flow inside of porous, these two sets of governing equation were combined into a unified equation for both flows inside and outside of the porous structure. Instead of implementing the coupling of two computational domains, the model can solve the two sets of governing equations simultaneously by just changing the value of the resistance force. A simple and effective boundary treatment method was proposed to implement the porous interface boundary condition.

The SPH model was validated by comparing the numerically calculated wave damping ratio against the theoretical prediction for the case of wave propagation over a porous bed. The results show that the accuracy improvement can be achieved by the pressure average using kernel function at the interface zone. As a way of checking the consistency of the predictions, the time history of dynamic pressure was generated at three pairs of measurement points among which each point located at one side of the interface and is close to each other. The pressure curve of each pair of pressure points matches each other perfectly from the beginning of the time till end, including all the peak value and even pressure fluctuation. As an application and further evaluation of the model, an investigation was conducted to explore the flow motion inside of a submerged the porous structure. The free surface time history and detailed velocity filed were compared with the experiment data. A good agreement is obtained for both wave parameters. The pressure comparison proves that the interface boundary treatment is effective and all of these demonstrate that the ISPH model developed in this work is capable of modelling the wave interactions with porous structure.

Chapter 7

Conclusion and future work

7.1 Thesis contribution

The contributions of this thesis are threefold.

Firstly, a new pressure Poisson equation source term with the weighted combinations of the density invariant and velocity divergence terms is proposed to improve the stability and accuracy of the ISPH method for wave impact simulations. The model is evaluated by applying it to two typical wave impact cases: one is the dam breaking wave impact on a vertical wall and the other one is the solitary wave running up and impact on a coastal house. The computational results have indicated that the combined source term treatment can well predict the wave impact pressure and force. Sensitivity studies have shown that the weighting coefficient in the mixed source term is quite independent of the particle spacing in a converged solution and thus can be practically treated as a constant.

Through model validations against the documented data, we could find that the proposed ISPH model with improved PPE source term could well predict the dam break wave impact with much less pressure noises and also satisfactorily reproduce the solitary wave impact forces computed by the established RANS model. Although the total CPU cost of the mixed model is comparable to the model in which either the pure density invariant or velocity divergence free PPE source term is used, the computational accuracy has considerably improved based on the minimum modifications of the numerical algorithm. The tests also demonstrated that the model should be applicable to different wave impact situations with consistent behaviour of the weighting coefficient in the PPE source term for each application, thus it would be expected to provide a potential promising tool to predict real wave impact

problems with sufficient accuracy. This would be of particularly interest to the breakwater design, in which accurate integrations of the wave force and moment are required. However, depending on different flow applications, the weighting coefficient could vary considerably. For the more violent wave impact case, the divergence part is found to play a more prominent role in ensuring accurate force simulations, while in the less violent wave impact problems, the density part seems to be more important. For the two investigated wave impact cases, the weighting coefficient ranges from α = 5% in the dam break impact to 50% in the solitary wave impact.

Also, by performing additional three numerical tests and carrying out relevant analysis, it was found that there existed a close correlation between the ratio of flow height to length scales H/L and the weighting coefficient α in the mixed pressure source term. The relationship curve changes more notably in the middle range of H/L but varies very little near its lower and upper bounds. This result could be used to pre-determine the PPE source term coefficient and thus predict wave impacts in a practical engineering application where no measurements are available.

Secondly, to improve the ISPH modelling capacity a mixed source term model has been proposed by combining the standard density-invariant and the velocity divergence-free formulations in a weighted average form. The new model was applied to two benchmark dam break flows and one solitary wave impact problem for two different wave heights. By comparing with the documented experimental and numerical data, it was found that the mixed source term ISPH model predicted more accurate impact pressures and forces as compared with the results obtained using either the density-invariant or the velocity divergence-free ISPH model.

To further quantify the numerical errors generated from different ISPH source term treatments, the time histories of the particle density and velocity divergence errors were investigated by using two dam break flows and one solitary wave impact flow. Not only we have found that the numerical errors were closely linked with the violent fluid deformations and impacts, but also it has been disclosed

that a strict density-invariant model could generated relatively larger divergence errors while a strict divergence-free model generated relatively larger density errors. The mixed source term model can effectively reduce both the density and divergence errors simultaneously and thus gave the best performance in predicting the macro flow behaviours. Also, these errors have been found to be closely related to large free surface deformation and flow impact.

Thirdly, the SPH model was extended for studying the wave interaction with porous structure to explore the flow motion inside and in the vicinity of the porous structure. After a comprehensive analysis of the Navier-Stokes equations for flow outside porous and the Navier-Stokes type equation for flow inside of porous, these two sets of governing equation were combined into a unified equation for both flows inside and outside of the porous structure. Instead of implementing the coupling of two computational domains, the model can solve the two sets of governing equations simultaneously by just changing the value of the resistance force. A simple and effective boundary treatment method was proposed to implement the porous interface boundary condition.

The SPH model was validated by comparing the numerically calculated wave damping ratio against the theoretical prediction for the case of wave propagation over a porous bed. The results show that the accuracy improvement can be achieved by the pressure average using kernel function at the interface zone. As a way of checking the consistency of the predictions, the time history of dynamic pressure was generated at three pairs of measurement points among which each point located at one side of the interface and is close to each other. The pressure curve of each pair of pressure points matches each other perfectly from the beginning of the time till end, including all the peak value and even pressure fluctuation. As an application and further evaluation of the model, an investigation was conducted to explore the flow motion inside of a submerged the porous structure. The free surface time history and detailed velocity filed were compared with the experiment data. A good agreement is obtained for both wave parameters. The pressure comparison proves that the interface boundary treatment is effective and all of these demonstrate that the

ISPH model developed in this work is capable of modelling the wave interactions with porous structure

In conclusion, this thesis is among the first to provide a deeply analysis of the ISPH source term and proposed a new ISPH model with improved Poisson pressure equation. And the ISPH model was extended to explore the inside flow motion of the porous structure.

7.2 Future work

In this thesis, a new PPE source term with weighted combinations of the density invariant and velocity divergence terms is proposed to improve the stability and accuracy of the ISPH method for wave impact simulations. A simple fitting formulation was conducted to show correlation between the ratio of the flow height to the length scales (H/L) and the weighting coefficient α in the mixed pressure source term. This fitting is based on the dam break flow and solitary wave running over slope dike. The shape of the computation zone is simple and only solitary wave was included in the analysis. So, more complex geometries of computation zone and other type of waves may be considered to predetermine how to choose the value of the PPE source term coefficient.

As only laminar flow is studies here for wave interaction with porous structure, the turbulence effect is ignored in the study of simulating the flow field. However, Huang (2003) point out that this assumption could cause significant errors in some cases, such wave breaking or lager porosity. And even the turbulence inside the porous structure is usually very weak and negligible in the condition of small permeability of the porous medium according to Liu et al. (1999). It's necessary to add some established SPH turbulence models to study both the flow outside and inside of the porous in order to strengthen the robust nature of the ISPH numerical scheme. Besides, only the wave height and velocity of in porous flow simulation has been compared with the experiment data. Another work will be done to analyses the

pressure field inside of the porous structure, leading to the stability assessment of individual armour of rubble mound breakwater.

Through many problems has being addressed, one key problem concerning multi-size particle calculation in SPH schemes still limit the spread of SPH model application. The smoothing length depend on the particle size, however, the smoothing length determines the influence range of each particles. Usually, many technique focus on ensure uniform particle distribution and same influence range of each particles during the simulation to preserve the momentum conservative. This means that larger particles and smaller ones should not exist together in one simulation. Therefore, in order to extent the SPH application to more practical engineering problem, an effective multi-size particle technique is needed.

Bibliography

Adami, S., Hu, X.Y. and Adams, N.A., 2012. A generalized wall boundary condition for smoothed particle hydrodynamics. Journal of Computational Physics, 231(21): 7057-7075.

Akbari, H. and Namin, M.M., 2013. Moving particle method for modeling wave interaction with porous structures. Coast Eng, 74(0): 59-73.

Arbhabhirama, A. and Dinoy, A.A., 1973. Friction factor and Reynolds number in porous media flow. Journal of the Hydraulics Division, 99(6): 901-911.

Asai, M., Aly, A.M., Sonoda, Y. and Sakai, Y., 2012. A Stabilized Incompressible SPH Method by Relaxing the Density Invariance Condition. Journal of Applied Mathematics, 2012.

Beavers, G.S. and Joseph, D.D., 1967. Boundary conditions at a naturally permeable wall. J. Fluid Mech., 30(01): 197-207.

Buchner, B., 2002. Green Water on Ship-type Offshore Structures, Delft University of Technology.

Chang, T. and Chang, K., 2013. SPH Modeling of One-Dimensional Nonrectangular and Nonprismatic Channel Flows with Open Boundaries. Journal of Hydraulic Engineering, 139(11): 1142-1149.

Chen, Z., Zong, Z., Liu, M.B. and Li, H.T., 2013. A comparative study of truly incompressible and weakly compressible SPH methods for free surface incompressible flows. Int. J. Numer. Meth. Fluids, 73(9): 813-829.

Chorin, A.J., 1968. Numerical solution of the Navier-Stokes equations. Math. Comp, 22(104): 745–762.

Colagrossi, A. and Landrini, M., 2003. Numerical simulation of interfacial flows by smoothed particle hydrodynamics. Journal of Computational Physics, 191(2): 448-475.

Colin, F., Egli, R. and Lin, F.Y., 2006. Computing a null divergence velocity field using smoothed particle hydrodynamics. Journal of Computational Physics, 217(2): 680-692.

Crespo, A.J.C., Gómez-Gesteira, M. and Dalrymple, R.A., 2007. 3D SPH simulation of large waves mitigation with a dike. J. Hydraul. Res., 45(5): 631-642.

Cummins, S.J. and Rudman, M., 1999. An SPH projection method. Journal of Computational Physics, 152(2): 584-607.

Cummins, S.J., Silvester, T.B. and Cleary, P.W., 2012. Three-dimensional wave impact on a rigid structure using smoothed particle hydrodynamics. Int. J. Numer. Meth. Fluids, 68(12): 1471-1496.

Dalrymple, R.A. and Rogers, B.D., 2006. Numerical modeling of water waves with the SPH method. Coast Eng, 53(2-3): 141-147.

de Lemos, M.J., 2006. Turbulence in Porous Media: Modeling and Applications. Elsevier.

del Jesus, M., Lara, J.L. and Losada, I.J., 2012. Three-dimensional interaction of waves and porous coastal structures: Part I: Numerical model formulation. Coast Eng, 64(0): 57-72.

Demirbilek, Z. and Nwogu, O.G., 2007. Boussinesq Modeling of Wave Propagation and Runup over Fringing Coral Reefs, Model Evaluation Report. ERDC/CHL TR-07-12, Vicksburg, MS.

Deresiewicz, H. and Skalak, R., 1963. On uniqueness in dynamic poroelasticity. Bulletin of the Seismological Society of America, 53(4): 783-788.

Garcia, N., Lara, J.L. and Losada, I.J., 2004. 2-D numerical analysis of near-field flow at low-crested permeable breakwaters. Coast Eng, 51(10): 991-1020.

Ghadimi, P., Abtahi, S. and Dashtimanesh, A., 2012. Numerical Simulation of Solitary Waves by SPH Method and Parametric Studies on the Effect of Wave Height to Water Depth Ratio. International Journal of Engineering & Technology, 1(4): 453-465.

Gingold, R.A. and Monaghan, J.J., 1977. Smoothed particle hydrodynamics-Theory and application to non-spherical stars. Mon Not R Astron Soc, 181: 375-389.

Gómez-Gesteira, M., Cerqueiro, D., Crespo, C. and Dalrymple, R.A., 2005. Green water overtopping analyzed with a SPH model. Ocean Eng, 32(2): 223-238.

Gomez-Gesteira, M., Rogers, B.D., Dalrymple, R.A. and Crespo, A.J.C., 2010. State-of-the-art of classical SPH for free-surface flows. J. Hydraul. Res., 48: 6-27.

Goring, D.G., 1979. Tsunamis--The Propagation of Long Waves Onto a Shelf, California Institute of Technology, California.

Gotoh, H., Shao, S.D. and Memita, T., 2004. SPH-LES model for numerical investigation of wave interaction with partially immersed breakwater. Coast Eng J, 46(1): 39-63.

Gresho, P.M. and Sani, R.L., 1987. On pressure boundary conditions for the incompressible Navier-Stokes equations. Int. J. Numer. Meth. Fluids, 7(10): 1111-1145.

Gui, Q., Shao, S. and Dong, P., 2014. Wave Impact Simulations by an Improved ISPH Model. Journal of Waterway, Port, Coastal, and Ocean Engineering, 140(3): 04014005.

Herrera, P.A., Massabó, M. and Beckie, R.D., 2009. A meshless method to simulate solute transport in heterogeneous porous media. Advances in Water Resources, 32(3): 413-429.

Hsiao, S.-C. and Lin, T.-C., 2010. Tsunami-like solitary waves impinging and overtopping an impermeable seawall: Experiment and RANS modeling. Coast Eng, 57(1): 1-18.

Hsu, T.-J., Sakakiyama, T. and Liu, P.L.F., 2002. A numerical model for wave motions and turbulence flows in front of a composite breakwater. Coast Eng, 46(1): 25-50.

Hu, C. and Kashiwagi, M., 2004. A CIP-based method for numerical simulations of violent free-surface flows. J Mar Sci Technol, 9(4): 143-157.

Hu, X.Y. and Adams, N.A., 2007. An incompressible multi-phase SPH method. Journal of Computational Physics, 227(1): 264-278.

Huang, C.-J., Chang, H.-H. and Hwung, H.-H., 2003. Structural permeability effects on the interaction of a solitary wave and a submerged breakwater. Coast Eng, 49(1–2): 1-24.

Huang, C.-J. and Dong, C.-M., 2001. On the interaction of a solitary wave and a submerged dike. Coast Eng, 43(3–4): 265-286.

Huang, C.J., Shen, M.L. and Chang, H.H., 2008. Propagation of a solitary wave over rigid porous beds. Ocean Eng, 35(11-12): 1194-1202.

Hughes, J.P. and Graham, D.I., 2010. Comparison of incompressible and weakly-compressible SPH models for free-surface water flows. J. Hydraul. Res., 48(sup1): 105-117.

Karunarathna, S.A.S.A. and Lin, P., 2006. Numerical simulation of wave damping over porous seabeds. Coast Eng, 53(10): 845-855.

Khayyer, A. and Gotoh, H., 2009a. Modified Moving Particle Semi-implicit methods for the prediction of 2D wave impact pressure. Coast Eng, 56(4): 419-440.

Khayyer, A. and Gotoh, H., 2009b. Wave Impact Pressure Calculations by Improved SPH Methods. Int J Offshore Polar, 19(4): 300-307.

Khayyer, A. and Gotoh, H., 2010. On particle-based simulation of a dam break over a wet bed. J. Hydraul. Res., 48(2): 238-249.

Khayyer, A. and Gotoh, H., 2011. Enhancement of stability and accuracy of the moving particle semi-implicit method. Journal of Computational Physics, 230(8): 3093-3118.

Khayyer, A. and Gotoh, H., 2012. A 3D higher order Laplacian model for enhancement and stabilization of pressure calculation in 3D MPS-based simulations. Appl Ocean Res, 37(0): 120-126.

Khayyer, A., Gotoh, H. and Shao, S.D., 2008. Corrected Incompressible SPH method for accurate water-surface tracking in breaking waves. Coast Eng, 55(3): 236-250.

Khayyer, A., Gotoh, H. and Shao, S.D., 2009. Enhanced predictions of wave impact pressure by improved incompressible SPH methods. Appl Ocean Res, 31(2): 111-131.

Kobayashi, N. and Wurjanto, A., 1990. Numerical model for waves on rough permeable slopes. J Coastal Res: 149-166.

Koh, C.G., Luo, M., Gao, M. and Bai, W., 2013. Modelling of liquid sloshing with constrained floating baffle. Computers & Structures, 122(0): 270-279.

Kondo, M. and Koshizuka, S., 2011. Improvement of stability in moving particle semi-implicit method. Int. J. Numer. Meth. Fluids, 65(6): 638-654.

Koshizuka, S., Nobe, A. and Oka, Y., 1998. Numerical analysis of breaking waves using the moving particle semi-implicit method. Int. J. Numer. Meth. Fluids, 26(7): 751-769.

Lara, J.L., Garcia, N. and Losada, I.J., 2006. RANS modelling applied to random wave interaction with submerged permeable structures. Coast Eng, 53(5–6): 395-417.

Lara, J.L., Losada, I.J. and Guanche, R., 2008. Wave interaction with low-mound breakwaters using a RANS model. Ocean Eng, 35(13): 1388-1400.

Larsen, J. and Dancy, H., 1983. Open boundaries in short wave simulations — A new approach. Coast Eng, 7(3): 285-297.

Lee, B.H., Park, J.C., Kim, M.H. and Hwang, S.C., 2011. Step-by-step improvement of MPS method in simulating violent free-surface motions and impact-loads. Comput Method Appl M, 200(9-12): 1113-1125.

Lee, E.S., Moulinec, C., Xu, R., Violeau, D., Laurence, D. and Stansby, P., 2008. Comparisons of weakly compressible and truly incompressible algorithms for the SPH mesh free particle method. Journal of Computational Physics, 227(18): 8417-8436.

Lee, E.S., Violeau, D., Issa, R. and Ploix, S., 2010. Application of weakly compressible and truly incompressible SPH to 3-D water collapse in waterworks. J. Hydraul. Res., 48(SUPPL. 1): 50-60.

Lee, J.-J., Skjelbreia, J.E. and Raichlen, F., 1982. Measurmment of Velocities in Solitary Waves. Journal of the Waterway Port Coastal and Ocean Division, 108(2): 200-218.

Li, J., Liu, H., Gong, K., Tan, S.K. and Shao, S., 2012. SPH modeling of solitary wave fissions over uneven bottoms. Coast Eng, 60(0): 261-275.

Liang, D.F., Thusyanthan, N.I., Gopal Madabhushi, S.P. and Tang, H.W., 2010. Modelling solitary waves and its impact on coastal houses with SPH method. China Ocean Engineering, 24(2): 353-368.

Liu, G.R. and Liu, M.B., 2003. Smoothed Particle Hydrodynamics: a meshfree particle method. World Scientific.

Liu, P.L., 1973. Damping of water waves over porous bed. Journal of the Hydraulics Division, 99(12): 2263-2271.

Liu, P.L.F., Lin, P., Chang, K.A. and Sakakiyama, T., 1999. Numerical modeling of wave interaction with porous structures. Journal of Waterway, Port, Coastal and Ocean Engineering, 125(6): 322-330.

Lo, E.Y.M. and Shao, S., 2002. Simulation of near-shore solitary wave mechanics by an incompressible SPH method. Appl Ocean Res, 24(5): 275-286.

Lucy, L.B., 1977. A numerical approach to the testing of the fission hypothesis. The astronomical journal, 82: 1013-1024.

Mansour, J.A., 2008. SPH and α-SPH: Applications and Analysis. Monash University.

Marrone, S., Antuono, M., Colagrossi, A., Colicchio, G., Le Touzé, D. and Graziani, G., 2011. δ-SPH model for simulating violent impact flows. Comput Method Appl M, 200(13–16): 1526-1542.

McDougal, W., 1993. State of the art practice in coastal engineering. Lecture Notes, National Cheng Kung University, Taiwan: 10.25-10.28.

Monaghan, J.J., 1989. On the problem of penetration in particle methods. Journal of Computational Physics, 82(1): 1-15.

Monaghan, J.J., 1992. Smoothed Particle Hydrodynamics. Annu Rev Astron Astr, 30(1): 543-574.

Monaghan, J.J., 1994. Simulating free surface flows with SPH. Journal of Computational Physics, 110: 399-406.

Monaghan, J.J., 2002. SPH compressible turbulence. Mon Not R Astron Soc, 335(3): 843-852.

Monaghan, J.J., 2004. Energy transfer in a particle α model. Journal of Turbulence: N12.

Monaghan, J.J. and Kajtar, J.B., 2009. SPH particle boundary forces for arbitrary boundaries. Computer Physics Communications, 180(10): 1811-1820.

Monaghan, J.J. and Kos, A., 1999. Solitary waves on a cretan beach. Journal of Waterway, Port, Coastal and Ocean Engineering, 125(3): 145-154.

Monaghan, J.J., Kos, A. and Issa, N., 2003. Fluid motion generated by impact. Journal of Waterway, Port, Coastal and Ocean Engineering, 129(6): 250-259.

Monaghan, J.J. and Lattanzio, J.C., 1985. A refined particle method for astrophysical problems. Astronomy and Astrophysics, 149: 135-143.

Morris, J.P., 1994. A Study of the Stability Properties of SPH, Monash University, Melbourne.

Morris, J.P., 1996. Analysis of Smoothed Particle Hydrodynamics with Applications, Monash University, 338 pp.

Oger, G., Doring, M., Alessandrini, B. and Ferrant, P., 2007. An improved SPH method: Towards higher order convergence. Journal of Computational Physics, 225(2): 1472-1492.

Orszaghova, J., 2011. Solitary waves and wave groups at the shore, Oxford University.

Packwood, A.R. and Peregrine, D.H., 1980. The propagation of solitary waves and bores over a porous bed. Coast Eng, 3: 221-242.

Peregrine, D., 2003. Water-wave impact on walls. Annu Rev Fluid Mech, 35(1): 23-43.

Randles, P.W. and Libersky, L.D., 1996a. Smoothed Particle Hydrodynamics: Some recent improvements and applications. Comput Method Appl M, 139(1-4): 375-408.

Randles, P.W. and Libersky, L.D., 1996b. Smoothed Particle Hydrodynamics: Some recent improvements and applications. Comput Method Appl M, 139(1–4): 375-408.

Ren, B., Wen, H., Dong, P. and Wang, Y., 2014. Numerical simulation of wave interaction with porous structures using an improved smoothed particle hydrodynamic method. Coast Eng, 88(0): 88-100.

Robertson, I.N., Paczkowski, K., Riggs, H.R. and Mohamed, A., 2011. TSUNAMI BORE FORCES ON WALLS. Proceedings of the ASME 2011 30th International Conference on Ocean, Offshore and Arctic Engineering, Rotterdam, The Netherlands, p.^pp. 395-403.

Robertson, I.N., Paczkowski, K., Riggs, H.R. and Mohamed, A., 2013. Experimental Investigation of Tsunami Bore Forces on Vertical Walls. Journal of Offshore Mechanics and Arctic Engineering, 135(2).

Rogallo, R.S. and Moin, P., 1984. Numerical Simulation of Turbulent Flows. Annu Rev Fluid Mech, 16(1): 99-137.

Rogers, B.D., Dalrymple, R.A. and Stansby, P.K., 2010. Simulation of caisson breakwater movement using 2-D SPH. J. Hydraul. Res., 48: 135-141.

Rojanakamthorn, S., Isobe, M. and Watanabe, A., 1989. A mathematical model of wave transformation over a submerged breakwater. Coastal Engineering in Japan, 32(2): 209-234.

Shadloo, M.S., Zainali, A., Yildiz, M. and Suleman, A., 2012. A robust weakly compressible SPH method and its comparison with an incompressible SPH. Int J Numer Meth Eng, 89(8): 939-956.

Shao, S., 2005. SPH simulation of solitary wave interaction with a curtain-type breakwater. J. Hydraul. Res., 43(4): 366-375.

Shao, S., 2010. Incompressible SPH flow model for wave interactions with porous media. Coast Eng, 57(3): 304-316.

Shao, S. and Gotoh, H., 2004. Simulating coupled motion of progressive wave and floating curtain wall by SPH-LES model. Coast Eng J, 46(2): 171-202.

Shao, S., Ji, C., Graham, D.I., Reeve, D.E., James, P.W. and Chadwick, A.J., 2006. Simulation of wave overtopping by an incompressible SPH model. Coast Eng, 53(9): 723-735.

Shao, S. and Lo, E.Y.M., 2003. Incompressible SPH method for simulating Newtonian and non-Newtonian flows with a free surface. Advances in Water Resources, 26(7): 787-800.

Shiach, J.B., Mingham, C.G., Ingram, D.M. and Bruce, T., 2004. The applicability of the shallow water equations for modelling violent wave overtopping. Coast Eng, 51(1): 1-15.

Slattery, J.C., 1999. Advanced transport phenomena. Cambridge University Press.

Sollitt, C.K. and Cross, R.H., 1972. Wave transmission through permeable breakwaters. Coastal Engineering Proceedings, 1(13).

Sulisz, W., 1985. Wave reflection and transmission at permeable breakwaters of arbitrary cross-section. Coast Eng, 9(4): 371-386.

Szewc, K., Pozorski, J. and Minier, J.P., 2012. Analysis of the incompressibility constraint in the smoothed particle hydrodynamics method. Int J Numer Meth Eng, 92(4): 343-369.

Tartakovsky, A.M. and Meakin, P., 2006. Pore scale modeling of immiscible and miscible fluid flows using smoothed particle hydrodynamics. Advances in Water Resources, 29(10): 1464-1478.

Thao, N.D., Esteban, M., Takagi, H. and Shibayama, T., 2008. IMPACT PRESSURES DUE TO BREAKING SOLITARY WAVE EXERTED ON A VERTICAL WALL. In: J.M. Smith (Editor), Coastal Engineering 2008. World Scientific Pub Co Inc, pp. 3186-3198.

Vacondio, R., Rogers, B.D., Stansby, P.K. and Mignosa, P., 2013. Shallow water SPH for flooding with dynamic particle coalescing and splitting. Advances in Water Resources, 58(0): 10-23.

van Gent, M.R.A., 1995. Wave Interaction with Permeable Coastal Structures. Dissertation Thesis.

Violeau, D. and Issa, R., 2007. Numerical modelling of complex turbulent free-surface flows with the SPH method: an overview. Int. J. Numer. Meth. Fluids, 53(2): 277-304.

Wu, Y.-T. and Hsiao, S.-C., 2013. Propagation of solitary waves over a submerged permeable breakwater. Coast Eng, 81(0): 1-18.

Wu, Y.-T., Yeh, C.-L. and Hsiao, S.-C., 2014. Three-dimensional numerical simulation on the interaction of solitary waves and porous breakwaters. Coast Eng, 85(0): 12-29.

Wurjanto, A. and Kobayashi, N., 1993. Irregular Wave Reflection and Runup on Permeable Slopes. Journal of Waterway, Port, Coastal, and Ocean Engineering, 119(5): 537-557.

Xia, X., Liang, Q., Pastor, M., Zou, W. and Zhuang, Y.-F., 2013. Balancing the source terms in a SPH model for solving the shallow water equations. Advances in Water Resources, 59(0): 25-38.

Xiao, H. and Huang, W., 2008. Numerical modeling of wave runup and forces on an idealized beachfront house. Ocean Eng, 35(1): 106-116.

Xu, R., 2010. An improved incompressible smoothed particle hydrodynamics method and its application in free-surface simulations, University of Manchester, Manchester.

Xu, R., Stansby, P. and Laurence, D., 2009. Accuracy and stability in incompressible SPH (ISPH) based on the projection method and a new approach. Journal of Computational Physics, 228(18): 6703-6725.

Yu, X. and Chwang, A., 1994. Wave Motion through Porous Structures. Journal of Engineering Mechanics, 120(5): 989-1008.

Zhang, S., Morita, K., Fukuda, K. and Shirakawa, N., 2006. An improved MPS method for numerical simulations of convective heat transfer problems. Int. J. Numer. Meth. Fluids, 51(1): 31-47.

Zhu, Y., Fox, P.J. and Morris, J.P., 1999. A pore-scale numerical model for flow through porous media. International Journal for Numerical and Analytical Methods in Geomechanics, 23(9): 881-904.